Università degli Studi di Ferrara

DOTTORATO DI RICERCA IN
"SCIENZE BIOMEDICHE E BIOTECNOLOGICHE"

CICLO XXX

COORDINATORE Prof. Paolo Pinton

Linking mitochondria to different human disorders: implication of mitophagy in LHON disease and characterization of the mitochondrial Ca^{2+} regulator MCUb in cancer progression

Settore Scientifico Disciplinare: MED/04

PhD student

Dott. Alberto Danese

Supervisor

Prof. Paolo Pinton

Anni 2015/2017

ABBREVIATIONS

AEQ	aequorin;
AKT	protein kinase B;
ANT	adenine nucleotide translocase;
ATG	autophagy related genes;
Bcl-2	B-cell lymphoma 2;
Ca^{2+}	calcium ions;
$[Ca^{2+}]$	Ca^{2+} concentration;
$[Ca^{2+}]_c$	cytosolic Ca^{2+} concentration;
$[Ca^{2+}]_{er}$	endoplasmic reticulum Ca^{2+} concentration;
$[Ca^{2+}]_m$	mitochondrial Ca^{2+} concentration;
CaMKII	Ca^{2+}/calmodulin-dependent protein kinase II;
CMA	chaperone mediated autophagy;
CNX	calnexin;
cytC	cytochrome C;
DAG	diacylglycerol;
DRP1	dynamin-related protein;
$\Delta\Psi_m$	mitochondrial membrane potential;
ER	endoplasmic reticulum;
ERMES	ER-mitochondria encounter structure;
GFP	green fluorescent protein;
grp75	glucose-regulated protein 75;
HIF1α	hypoxia-inducible factor 1-alpha;
IMM	inner mitochondrial membrane;
IMS	intermembrane space;
IP3	inositol 1,4,5-trisphosphate;
IP3R	inositol 1,4,5-trisphosphate receptor;
IP3-BD	IP3-binding domain;
LC3	microtubule-associated protein-light chain 3;
LHON	Leber's hereditary optic neuropathy;
Letm1	leucine zipper-EF-hand containing transmembrane protein 1;
MAMs	mitochondria-associated membranes;
MEFs	mouse embryonic fibroblasts;

MCU	mitochondrial Ca^{2+} uniporter;
MICU1/2	mitochondrial calcium uptake 1/2;
MCUR1	mitochondrial calcium uniporter regulator 1;
MMP	mitochondrial membrane permeabilization;
mTOR	mammalian target of rapamycin;
mtDNA	mitochondrial DNA;
Mfn-1 -2	mitofusin-1 -2;
NCX	Na^{2+}/Ca^{2+} exchanger;
Oct-3/4	octamer-binding transcription factor 3/4;
OMM	outer mitochondrial membrane;
OXPHOS	oxidative phosphorylation;
PACS-2	phosphofurin acidic cluster sorting protein 2;
PAMs	plasma membrane associated membranes;
PE	phosphatidylethanolamine;
PI3K	phosphatidylinositol 3-kinase;
PIP2	phosphatidylinositol 4,5-bisphosphate;
PLC-β	phospholipase C-β;
PM	plasma membrane;
PMCA	plasma membrane Ca^{2+} ATPase;
PML	promyelocytic leukemia protein;
mPTP	permeability transition pore;
ROCs	receptor operated Ca^{2+} channels:
ROS	reactive oxygen species;
RyR	ryanodine receptor;
SERCA	sarco-endoplasmic reticulum Ca^{2+} ATPase;
Sig-1R	Sigma-1 receptor;
SOCE	store-operated Ca^{2+} entry;
SOD	superoxide dismutase;
Sox2	sex determining region Y-box 2;
SR	sarcoplasmic reticulum;
TCA	tricarboxylic acid circle;
VDAC	voltage-dependent anion channel;
VOCs	voltage operated Ca^{2+} channels.

Abstract

Ca^{2+} homeostasis and Ca^{2+} signal perform a central role in modulating several cellular responses, such as motility, muscle contraction, fertilization, exocytosis, proliferation, and apoptosis. It is not surprising that, being involved in all these crucial processes, intracellular Ca^{2+} manipulation by numerous proteins can lead to dysfunctions. An essential organelle which has a protagonist role in calcium homeostasis regulation and in most of the previous mentioned cellular processes is undoubtedly the mitochondria. Mitochondrial dysfunctions have been found to be associated with several disorders such as neurodegenerative diseases, aging, and cancer. In this thesis work, we investigated mitochondrial dynamics in the context of an important optic neuropathy and in cell cycle progression. In particular, we explored the role of autophagic and compartment-specific mitophagic activity in Leber's hereditary optic neuropathy (LHON) finding that this degradative process represents a primary target for blocking the progressive optic nerve degeneration and the consequent reduction of vision typical of this neuropathy. Concerning cell cycle, with this work, we place the mitochondria at the center of a $[Ca^{2+}]_c$ buffering action that allows the correct progression through the cell cycle, and we assign for the first time a potential oncogenic connotation to the MCU complex dominant-negative subunit MCUb. Taken together, these data remark the importance of this fascinating organelle, clarifies some relationships between mitochondria, calcium signaling, and cell physiology and provide a new starting point for future investigations aimed at identifying new therapies for and against mitochondrial-mediated cell death.

1. INTRODUCTION

1.1 MITOCHONDRIA AND SURROUNDINGS

Mitochondria have a crucial role in life and death of eukaryotic cells since they are the main players in many cellular processes such as energy production, apoptosis, autophagy, reactive species of oxygen (ROS) production, thermogenesis and calcium homeostasis.

In the last 20 years, several human disorders including neurodegenerative diseases, cancer, and diabetes, have been shown to be due to mitochondrial dysfunctions. Furthermore, the mitochondrial dysfunction may also be involved in the natural process of aging.

1.1.1 Mitochondrial structure

Mitochondria are characterized by a double system of membranes, delimitating four "mitochondrial spaces" where different metabolic pathways take place: the outer membrane (OMM), the intermembrane space (IMS), the inner membrane (IMM) and the matrix.

The OMM is permeable to ions and small proteins (MW<10 kDa) because of the abundance of a large conductance channel, known as mitochondrial porin or voltage-dependent anion channel (VDAC) (*1*). IMS contains about 6% of total mitochondrial protein; the most abundant member is represented by cytochrome c, a component of the oxidative phosphorylation (oxphos) system. IMS also contains pro-apoptotic proteins as well as enzymes, which are involved in the energetic metabolism (adenylate kinase and creatine kinase), in reactive oxygen species removal and in the membrane organization.

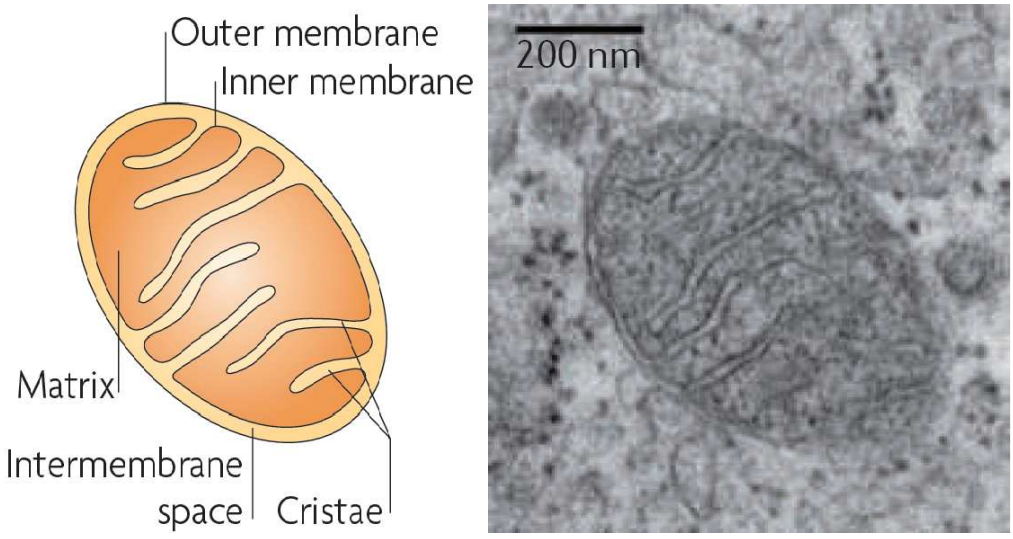

Figure 1 - Mitochondrial ultrastructure. On the left, a schematic image representing the structure of mitochondria. A transmission electron microscopy image of mitochondria in ultrathin sections of human fibroblast cells on the right. (Figure from Westermann, Nat Rev Moll Cell Bio 2010)

The IMM is impermeable to most small molecules and ions, being responsible for the maintenance of the electrochemical gradient between the matrix and the IMS. The IMM is organized in different compartments: the peripheral inner membrane and lamellar double-membrane interdigitations called cristae (*2*). Cristae are not merely random folds, but rather internal compartments formed by deep invaginations originating from very tiny "point-like structures" in the inner membrane. These narrow tubular structures, called cristae junctions, can limit the diffusion of molecules from the intra-cristae space towards the IMS, thus creating a microenvironment where mitochondrial electron transport chain (ETC) complexes (as well as other proteins) are hosted and protected from random diffusion. The inner boundary membrane is enriched with structural proteins and components of the import machinery of mitochondria.

In addition to enzymes and cofactors of catabolic metabolism, the matrix also contains all the components of mitochondrial protein synthesis machinery and several copies of mitochondrial DNA molecules as well as catalase, glutathione peroxidase, peroxiredoxin and antioxidant enzymes like manganese superoxide dismutase.

Since the IMM is the site of OXPHOS, the morphology of cristae and cristae junctions can have profound implications for the rate of ATP production (*3*). Moreover, the number and shape of these structures can also limit the diffusion of cytochrome c by compartmentalization and consequently regulate the propensity to cell death.

According to the evolution theory, mitochondria derives from a symbiotic relationship between a primordial eukaryotic cell and an aerobic bacterium (*4*). After this symbiotic event, part of the proto-mitochondrion genome has been transferred to the nucleus. In Mammalian mtDNA molecule retains only 37 genes: the 12S and 16S rRNA and the 22 tRNAs representing the mitochondrial translational machinery along with 13 structural genes. These mtDNA-encoded proteins are structural subunits of oxidative phosphorylation system. They include: seven (ND1-ND4, ND4L, ND5, ND6) of the 46 peptides of Complex I, one of the eleven peptides of Complex III (cytochrome b), three of the 13 peptides of Complex IV (COI, COII, COIII) and two of the 16 peptides of Complex V (ATP6, ATP8).

1.1.2 Mitochondria associated membrane (MAM)

Specific organization of the intracellular organelles enables direct communication between various compartments within the cell. Among the different direct interactions or "close contacts" between cellular organelles, MAMs have recently attracted the attention of many researchers, as represented by the growing number of publications describing the critical roles of MAMs in physiology and pathology. MAMs consist of regions of the ER involved

in direct interactions with the mitochondria. However, proteins from other cellular compartments have also been found in MAMs, suggesting that MAMs also form close contacts with other intracellular structures in addition to the ER. For instance, plasma membrane (PM) proteins are observed in MAMs, indicating the presence of close contacts between the mitochondria and the PM (*5*). According to numerous studies, mitochondria-ER contact sites are dynamic structures. However, because we can isolate these structures, the interactions between these membranes are strong, and they are not destroyed during isolation procedures. Plasma membrane-associated membranes (PAMs) (*6*) and ER-mitochondria encounter structures (ERMES) (*7*) are other examples of the physical and functional contacts that are isolated during cellular subfractionation.

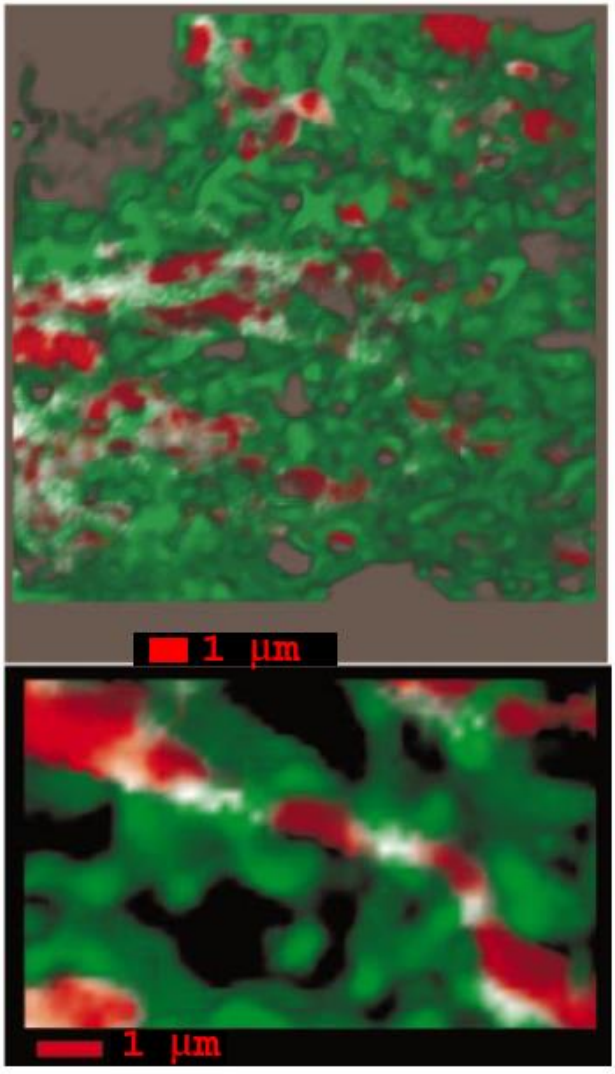

Figure 2 - High-resolution 3D imaging of ER-mitochondria contact sites. Combined 3D imaging of mitochondria and ER in a HeLa cell transiently expressing mtGFP(Y66H, Y145F) and erGFP(S65T). The mitochondrial and ER images are represented in red and green, respectively; the overlaps of the two images are white. On the bottom, a detail of the main image (80-nm pixel) (figure from Rizzuto, R., et al., Science, 1998).

Most researchers believe that the first evidence showing that the mitochondria and ER are closely positioned at some regions comes from the early 1970s in the studies by Franke and Kartenbeck (*8*) and Morre et al. (*9*). However, the first reports on the direct association

between the mitochondria and ER date back to as early as the late 1950s (*10*). Almost simultaneously with the observations mentioned above from the 1970s, Lewis and Tata (*11*) observed that a fraction of the ER was found in low-speed centrifugation pellets containing the mitochondrial portion during subfractionation of rat liver homogenates. Based on this observation, we acknowledge this paper as the first report to describe a MAM isolation procedure. Almost twenty years later, in the early 1990s, the Vance group made significant progress in the MAM field by presenting a detailed protocol describing the isolation of pure MAM fractions in a series of articles published in J. Biol. Chem. (*12*), which was improved upon by Meier et al. (*13*) ten years later. Over the years, the MAM isolation method was developed and optimized to enable the isolation of MAMs from different animal tissues and cell cultures (*14*). The existence of the MAM fraction is not an exclusive characteristic of mammalian cells; close interactions between mitochondria and the ER have also been described in yeast. Interestingly, similar contacts between mitochondria and the ER have been described for chloroplasts and the ER in plants.

In addition to the development of more refined protocols for isolating pure MAM fractions, the list of proteins present at mitochondria-ER contact sites increases every year. Although many proteins localized at the MAM have been identified, we have not determined which proteins can be used as universal MAM markers because some MAM proteins are only present in specific organs, tissues or cell types. Another problem is the observation that no protein is exclusively localized to the MAM fraction. Instead, the localization of a specific protein at the MAM is only appropriately termed as enriched because these proteins are also present in other cellular compartments. Regarding the molecular composition of the MAM fraction, an article by Poston et al. presents a detailed proteomic analysis of the MAM (*5*). These authors detected and classified approximately 1200 proteins from the MAM fraction isolated from a mouse brain and confirmed that the MAM fraction contains proteins characteristic of the PM and the Golgi apparatus (24% and 6%, respectively, of the total proteins detected in MAMs). Based on the long list of proteins found in the MAM fraction or that translocate to the MAMs under certain conditions, MAMs seem to play essential roles in various processes. Initially, the MAM fraction was considered necessary for lipid synthesis and trafficking (long-chain fatty acid coenzyme A ligase-1 (FACL-1) and -4, phosphatidylserine synthase-1 (PSS-1) and -2, serine active site containing 1 (SERAC1), fatty acid transport protein 4 (FATP4), acyl-CoA desaturase, phosphatidylethanolamine N-methyltransferase 2 (PEMT2) and many other proteins present in MAM involved in this process are reviewed in (*15*)) and Ca^{2+} handling (e.g., IP3R, ryanodine receptor, sigma-1 receptor (SIG1R), and promyelocytic leukemia protein (PML)). MAMs were later linked to

the modulation of mitochondrial morphology (mitochondria-shaping proteins and chaperone proteins (MFN-1 and -2)), apoptosis (Bcl-2, hematopoietic cell-specific Lyn substrate1 (HCLS1)-binding protein 3 (HS1BP3)), mitochondrial contact site formation (VDAC and adenine nucleotide translocase (ANT)), protein folding (calnexin (CNX)) and sorting (phosphofurin acidic cluster sorting protein 2 (PACS-2)), ER stress (glucose-regulated protein 75-kDa (GRP75) and endoplasmic reticulum resident protein 44 (ERp44)), inflammation (inflammasome components: NALP3, adaptor ASC and thioredoxin interacting protein (TXNIP)), autophagy (pre-autophagosome/autophagosome markers (ATG14 and ATG5), and p66Shc) and the cellular response to oxidative stress (p66Shc protein and Ero1α). The presence of these critical proteins involved in crucial cellular processes explains why alterations in MAM composition are related to the pathogenesis of different disorders (*16*), including type-2 diabetes (mTOR complex 2 (mTORC2) and MAM-associated Akt), and several neuronal-based diseases, such as Parkinson's disease and Huntington's disease, and neurodegenerative diseases, such as schizophrenia, dementia, and seizures. Moreover, MAMs have been proposed to be involved in familial Alzheimer's disease (FAD) and GM1-gangliosidosis.

1.2 MITOCHONDRIA AND ENERGY PRODUCTION

1.2.1 Citric Acid Cycle

The citric acid cycle (TCA) was elucidated by Sir Hans Krebs in 1940 and later, in 1949, Kennedy and Lehningher demonstrated that the entire cycle occurs inside mitochondria (*17*). The triose deriving from glycolysis is wholly oxidized into three molecules of CO_2 during a sequence of reactions that allow the reduction of cofactors NAD and flavin adenine nucleotide (FAD), providing energy for the respiratory chain in the form of electrons. The first reaction of the citric acid cycle is the condensation of one Acetyl-CoA and a molecule of citrate to generate oxaloacetate and is catalyzed by citrate synthase. Citrate is then transformed into isocitrate by aconitase through the formation of cis-aconitate. This step is reversible and could lead to the accumulation of both citrate and isocitrate. Only the fast consumption of isocitrate by its dehydrogenase can force the reaction to the proper direction. Isocitrate dehydrogenase catalyzes the first irreversible oxidation leading to the decarboxylation of isocitrate, generating CO_2 and α-ketoglutarate. The second carbon leaves the cycle in the following step when the newly generated α- ketoglutarate is immediately decarboxylated by the α-ketoglutarate dehydrogenase complex in a reaction similar to the pyruvate decarboxylation. In fact, both these complexes share high similarities in enzyme

amino acid composition and the organization of the different subunits. The energy released from both oxidations is used to generate NADH from NAD that directly feeds into the respiratory chain.

The following step is catalyzed by succinyl-CoA synthetase and utilizes the energy derived from the CoA removal to phosphorylate GDP (or ADP) to GTP (or ATP). Selectivity for the nucleotide is determined by the isozyme involved. It has been well established that at least two isozymes of succinyl-CoA synthetase are expressed in animal tissues (*18*), and the proportion of them seems to be tissue specific.

The succinate generated in the previous step is a 4 carbons compound that is then converted, by three sequential reactions, to oxaloacetate to conclude the cycle. The first of these steps is the oxidation of succinate to fumarate by succinate dehydrogenase. This enzyme, tightly bound to the IMM, catalyzes FAD reduction to FADH2 that provides electrons for the respiratory chain. Fumarate is then hydrated by fumarate hydratase to L-malate. It is particularly interesting that both succinate dehydrogenase and fumarate hydratase are oncosuppressor genes. It has been demonstrated that inactivation of these oncosuppressors leads to the accumulation of succinate and fumarate that spread in the cytosol and promote hypoxia-inducible factor 1α (HIF1α) accumulation by inactivating prolyl hydroxylase enzymes (promoter of HIF1α degradation); HIF1α, in turn, improves a pseudo-hypoxic condition that favors tumor development (*19*). The last event that completes the citric acid cycle is the oxidation of L-malate to oxaloacetate. This reaction is performed by L-malate dehydrogenase, which induces the reduction of another molecule of NAD to NADH. The resulting molecule of oxaloacetate is suitable for starting another cycle through condensation with an acetyl group.

During all these processes, only one molecule of ATP (or GTP) is produced, but three molecules of NADH and one of FADH2 (plus one molecule of NADH from pyruvate dehydrogenase), which provide electrons for the respiratory chain, are also generated and subsequently result in the production of large amounts of ATP.

1.2.2 The oxidative phosphorylation

Mitochondria, performing the last steps of cellular catabolism, are commonly referred as "the energy factory" of the cell; they produce most of the energy required in the form of ATP. In fact, they are the site of the OXPHOS system and the electron transport chain, and through this, they oxidize hydrogen derived from our dietary carbohydrates (TCA cycle) and fats (β-oxidation) with oxygen to generate heat and ATP. Pyruvate, aminoacids and fatty acids deriving from cytosolic catabolic pathways are further oxidized in mitochondria matrix

through Krebs cycle or β-oxidation to produce NADH (nicotinamide adenine dinucleotide, reduced form) and FADH2 (flavine adenine dinucleotide, reduced form), as substrates of the respiratory chain. Since the inner membrane is freely permeable only to O_2, CO_2, and H_2O_2 and it lacks NADH transporters, electrons deriving from cytosolic NADH are transferred into mitochondrial matrix through shuttle systems.

The OXPHOS system is composed of five multimeric enzymatic complexes (I-V) and consists of approximately 90 subunits, 13 encoded by the mitochondrial DNA (mtDNA). All the complexes are integrated into the lipid bilayer of the mitochondrial IM and together with two mobile electron carriers, ubiquinone (CoQ) and cytochrome c (cyt c), they make up the electron transport chain.

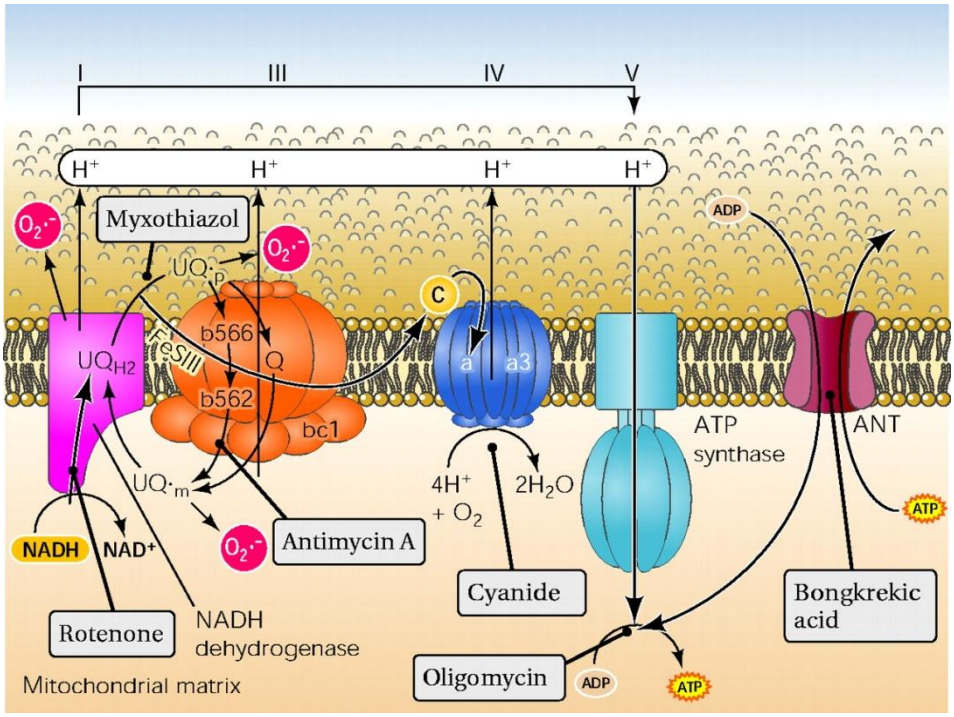

Figure 2 - Schematic representation of mitochondrial electron transport chain (adapted from Physiology 20:303-315, 2005)

Complex I (NADH dehydrogenase) is the largest of the respiratory complexes and is composed approximately of 45 subunits, seven encoded by mtDNA. Complex I or Complex II (succinate dehydrogenase) sequentially transfer two electrons deriving from NADH or FADH2 to CoQ giving ubisemiquinone (CoQ•) and then ubiquinol (CoQH2). Complex II is the only respiratory enzyme entirely encoded by nuclear DNA (nDNA), and it is composed of 4 subunits. Moreover, complex II is also the only enzyme of the respiratory chain that does not show proton-pumping activity, but it represents an alternative entry point for

electrons and a checkpoint for the coordination between Krebs cycle and oxidative phosphorylation.

Complex III (ubiquinol cytochrome c oxidoreductase) has only one mtDNA-encoded subunit, cytochrome b, and ten nDNA-encoded subunits. Complex III exists as symmetric dimer where each monomer consists of eleven subunits; its function comprises coupling electron transfer to the translocation of two protons across the IMM.

From cyt c, electrons flow to Complex IV (Cytochrome c oxidase) that is composed of 13 subunits, three of them encoded by mtDNA. Complex IV reduces molecular oxygen to water; the energy released by the esorgonic electron transfer to the oxygen is then converted into protonmotive force. Contextually to the redox reactions Complex I, III and IV pump protons from the matrix into the intermembrane space so that through the inner membrane is established an electrochemical gradient consisting of two components: ΔpH (chemical) and ΔΨ (electric).

This electrochemical gradient, due to the flow of the electrons through the respiratory chain, is finally used by Complex V (ATP synthase) to generate ATP.

ATP synthase could be divided into two main components: F0 that allows the channeling of protons, and F1 that catalyzes ATP phosphorylation. The F0 is embedded in the IMM, while the F1 resides in the mitochondrial matrix and is bound to the F0 through a γ subunit (which drives conformational changes) and a b2δ dimer (that holds F0 and F1 together). The protons flow from the intermembrane space to the matrix through the F0 inducing its rotation; the movement is transmitted from the γ subunit to the F1 causing conformational rearrangements. The F1 has a trimeric structure consisting of αβ dimers. The subsequent changes are linked to the binding of substrates, phosphorylation, and release of ATP. The three possible dimers are never in the same conformational state and, what is more, the conformational changes in one dimer drive rearrangements in the other. It has been calculated that for the synthesis of one ATP molecule, 4 protons are required (3 for the ATP synthase rearrangements and 1 for ATP, ADP and Pi transport). Once synthetized, ATP can locate inside mitochondrial matrix or be transported into the IMS by the nucleotide exchanger adenine nucleotide translocase (ANT) that passively exchanges ATP with ADP. Once in the IMS, ATP can freely pass the OMM through VDAC.

1.2.3 Reactive Oxygen Species (ROS) production and accumulation

Mitochondria are the primary source of ROS under normal physiological conditions, with superoxide

radicals being the primary ROS produced by these organelles. ROS are a variety of molecules and free radicals - chemical species with one unpaired electron - deriving from the partial reduction of molecular oxygen. Complex I and complex III are the major superoxide (O_2•-) producing sites in mitochondria. The O_2- is the product of a one-electron reduction of oxygen and is rapidly converted into hydrogen peroxide (H_2O_2) by manganese superoxide dismutase (MnSOD); this anion is then metabolized by glutathione peroxidize (GPX) to H_2O.

O_2•- can dismutate, spontaneously or through a reaction catalyzed by superoxide dismutases, to hydrogen peroxide. This species is not highly oxidant per se but can react with nitric oxide (NO•) in a reaction controlled by the rate of diffusion of both radicals to give peroxynitrite, (ONOO) a more powerful oxidant. ROS play an important role in regulating several cellular processes, including immune response and apoptosis, and act as second messengers in cellular signaling. ROS affect these standard cellular functions by altering the activities of various tyrosine and serine/threonine kinases, mitogen-activated protein kinases, and transcription factors. Excessive ROS production may cause local damage to the Fe-S clusters of respiratory enzymes (complexes I, II and III), as well as to tricarboxylic acid cycle enzymes (aconitase). Moreover, peroxynitrite can nitrate tyrosine residues or thiolic groups of nearby proteins and both complex I and MnSOD have been reported to be damaged by this process. Oxidized proteins are recognized by proteases and degraded.

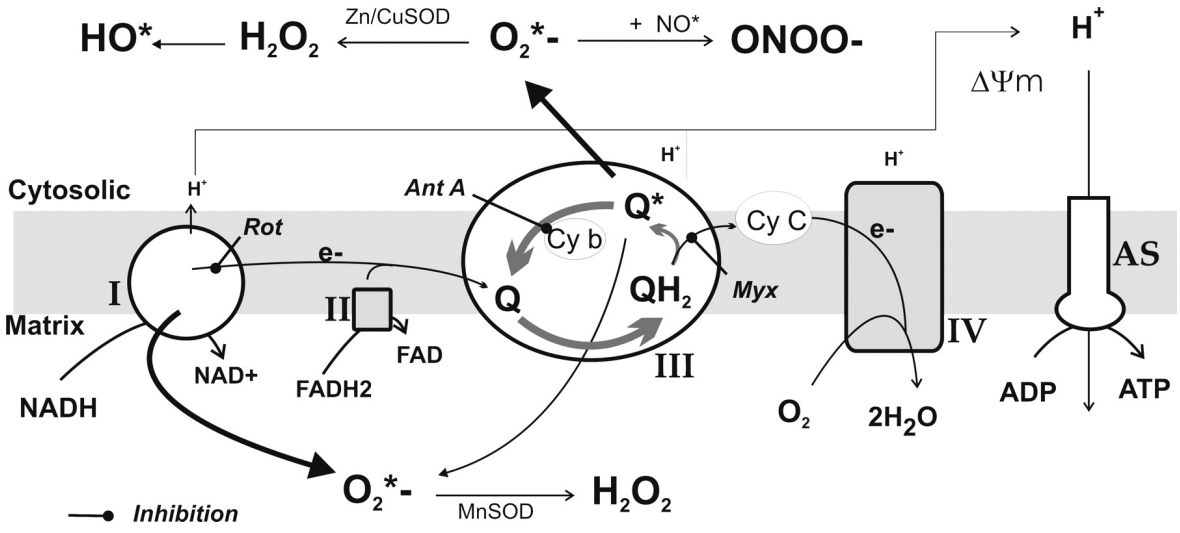

Figure 3 - Main mechanisms for mitochondrial reactive oxygen species (ROS) generation. The main routes for O_2−· transformation are represented. SOD, superoxide dismutase; H_2O_2, hydrogen peroxide; ONOO−, peroxynitrite; NO*, nitric oxide; $\Delta\Psi_m$: mitochondrial potential; AS, ATP synthase. Only the inner mitochondrial membrane is represented. (Figure from Camello-Almaraz et al., Cell Physiology, 2006)

Oxidative damage causes potentially mutagenic modifications to DNA, contributing to cancer, neurodegenerative diseases, and premature aging. In particular, due to the peculiar

structure, mtDNA is very susceptible to ROS attack and the oxidative damage is much higher than that in the nuclear DNA. Therefore, ROS induced injury is the principal cause of mitochondrial genomic instability leading to respiratory dysfunctions.

Lastly, another critical damaging process is lipid peroxidation; this affects vital mitochondrial functions, such as respiration and oxidative phosphorylation, inner membrane barrier properties, maintenance of mitochondrial membrane potential ($\Delta\Psi_m$), and mitochondrial Ca^{2+} buffering capacity.

1.3 MITOCHONDRIA AND CALCIUM

1.3.1 Ca^{2+} as a cellular signal

Intracellular Ca^{2+} signaling is fundamental for the regulation of multiple cellular processes, including development, proliferation, secretion, gene activation and cell death. The universality of Ca^{2+} as an intracellular messenger depends on its enormous versatility regarding speed, amplitude, and spatiotemporal patterning. The Ca^{2+}-signalling network can be divided into four functional units:

• signaling is triggered by a stimulus that generates various Ca^{2+}-mobilizing signals;

• the latter activates the ON mechanisms that feed Ca^{2+} into the cytoplasm;

• Ca^{2+} functions as a messenger to stimulate numerous Ca^{2+}-sensitive processes;

• the OFF mechanisms, composed of pumps and exchangers, remove Ca^{2+} from the cytoplasm to restore the resting state (*20*).

In resting cells, the $[Ca^{2+}]_c$ is carefully maintained at deficient levels (100 nM), while the concentration of the ion in the extracellular space is about 1 mM. There are also intracellular organelles, such as the ER and secretory granules, which contain one to ten thousand-fold greater concentrations of Ca^{2+} than the cytoplasm. There is an electric gradient between the two sides of the plasma membrane, which stands for values between -10 and -70 mV. The cell then spends a significant proportion of this energy against electrochemical gradient to maintain the concentration of this ion on such low values. However, in response to different stimuli, the amount of the cation may increase significantly, up to 1-3 μM. The rapid increase in $[Ca^{2+}]$ in the cytoplasm is, therefore, one of the leading features of the complex Ca^{2+} signal at the cellular level. The effect of this increase was correlated with an increasing number of physiopathological events. Muscle contraction, hormone secretion, synaptic transmission, as well as the proliferation and apoptosis are just a few examples of Ca^{2+}-mediated processes.

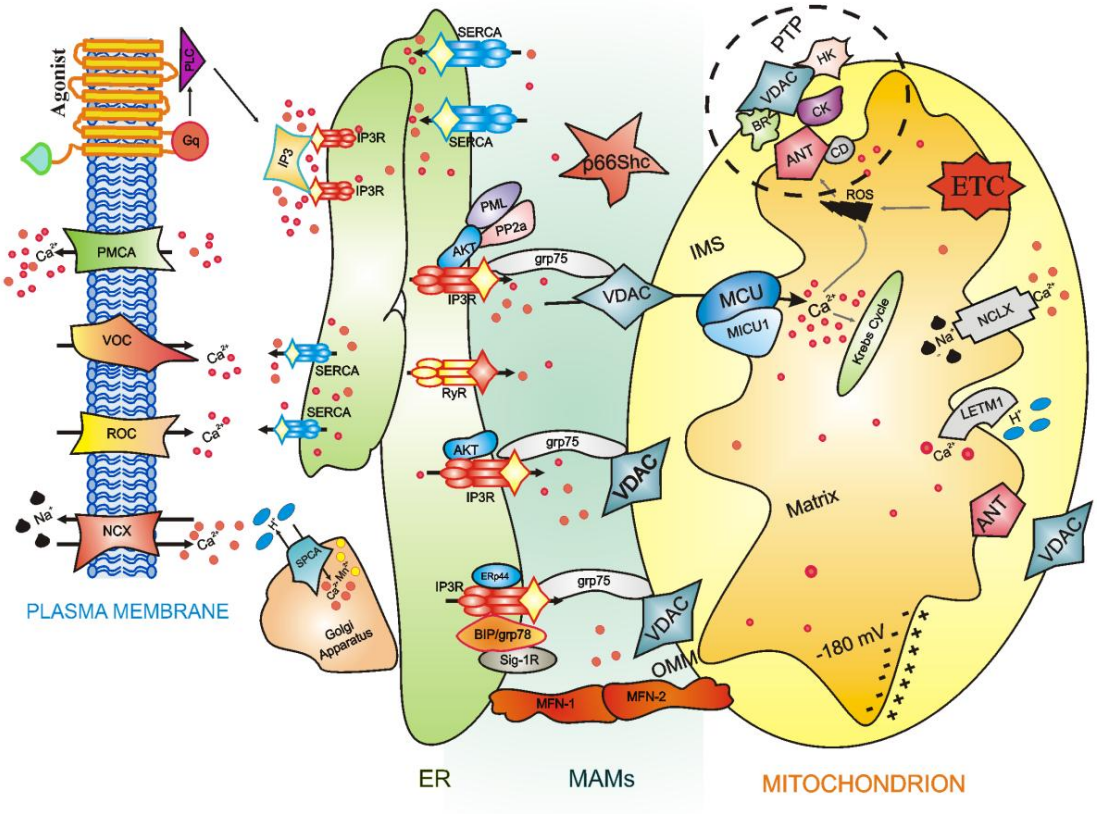

Figure 4 - Representation of intracellular Ca^{2+} dynamics and MAMs proteins involved in ER-mitochondria Ca^{2+} cross-talk. Cells generate a Ca^{2+} signal through two mechanisms that use internal and external sources of Ca^{2+}. Calcium enters the cell through channels and pumps situated on the plasma membrane; these are gated by voltage (VOCs) or external messengers (ROCs). A series of stimuli that act on cell surface receptors triggers the activation of PLC that catalyzes the hydrolysis of phosphatidylinositol 4,5-biphosphate to IP3 and DAG. The binding of IP3 to its receptor IP3R stimulates ER Ca^{2+} release and consequently the transfer of Ca^{2+} (red dots) from ER to mitochondria. Mitochondrial surface directly interacts with the ER through contact sites defining hotspot Ca^{2+} signaling units. Mitochondrial Ca^{2+} import occurs through the mitochondrial Ca^{2+} uniporter (MCU) and the H^+/Ca^{2+} exchanger LETM1; conversely, NCLX, mitochondrial Na^+/Ca^{2+} exchanger, together with the PTP, export Ca^{2+} from the matrix. Ca^{2+} levels return to resting conditions through a series of channels and pumps: PMCA and NCX permit the ion extrusion into the extracellular milieu, SERCA (situated on the ER) and SPCA (on the Golgi apparatus) re-establish basal Ca^{2+} levels in intracellular stores. Abbreviations: ANT, adenosine nucleoside transporter; ETC, electron transport chain; HK, hexokinase; CD, cyclophilin D; CK, creatine kinase; BR, benzodiazepine receptor (Figure from Patergnani et al., Cell Communication and Signaling, 2011)

The fundamental question is how it is possible that different events may be regulated by a single messenger. The answer is found in the versatility of the Ca^{2+} signal. An extensive Ca^{2+}-signalling toolkit is used to assemble signaling systems with very different spatial and temporal dynamics. Rapid highly localized Ca^{2+} spikes regulate fast responses, whereas slower reactions are controlled by repetitive global Ca^{2+} transients or intracellular Ca^{2+} waves. Ca^{2+} has a direct role in managing the expression patterns of its signaling systems that are continuously being remodeled in both health and disease. During the on reaction, stimuli induce both the entry of external Ca^{2+} and the formation of second messengers that release internal Ca^{2+} that is stored within the endoplasmic reticulum or Golgi apparatus. Most of this Ca^{2+} is bound to buffers, whereas a small proportion binds to the effectors that

activate various cellular processes. During the above reactions, Ca^{2+} leaves the effectors and buffers and is removed from the cell by multiple exchangers and pumps. The Na^{+}/Ca^{2+} exchanger (NCX) and the plasma membrane Ca^{2+}-ATPase (PMCA) extrude Ca^{2+} to the outside, whereas the sarco/endoplasmic reticulum Ca^{2+}-ATPase (SERCA) pumps Ca^{2+} back into the ER.

Mitochondria also have an active function during the recovery process in that they sequester Ca^{2+} rapidly through a uniporter, and release more slowly back into the cytosol to be dealt with by the SERCA and the PMCA. Cell survival is dependent on Ca^{2+} homeostasis, whereby the Ca^{2+} fluxes during the above reactions exactly match those during the on reaction.

1.3.2 Ca^{2+} release from intracellular stores

ER is the most extensive intracellular organelle, comprising a three-dimensional network of endomembranes arranged in a complex grid of cisternae and microtubules. This organelle is made up of structurally and functionally distinct domains, about the variety of cellular functions played by the organelle, primarily concerning protein synthesis, maturation, and delivery to their destination (*21*). Moreover, the ER is a dynamic reservoir of Ca^{2+} ions, which can be activated by both electrical and chemical cell stimulation (*22*), making this organelle an indispensable component of Ca^{2+} signaling.

ER's role in signaling comprises some components constituting the Ca^{2+} signaling pathway such as IP3Rs, RyRs, SERCAs, that are release channels and pumps. Also, buffers (calnexin, calreticulin) and some ancillary proteins (FK 506-binding proteins, sorcin, triadin, phospholamban) are involved (*23*).

Everything starts with many extracellular stimuli, such as hormones, growth factors, neurotransmitters, neurotrophins, odorants and light that generating IP3 through the phospholipase C isoforms, activated in different manners: G-protein coupled receptors (acting via PLC-β), tyrosine-kinase coupled receptors (PLC-γ), an increase in Ca2+ concentration (PLC-δ) or activated by Ras (PLC-ε) (*24*). The effector is the IP3Rs, nonselective cationic channels that conduct Ca^{2+}.

Three isoforms of IP3R encoded by different genes have been identified (IP3R1, 2 and 3) with varying affinities of agonist and tissue distribution (*25*). The domains that makeup IP3R3 include the IP3-binding domain (IP3-BD), located near the N-terminus of the protein; the six transmembrane-spanning domain is at the C-terminal end of each subunit, and, between them, an internal coupling domain assures the signal of IP3 binding is transferred to the channel-forming region, hence triggering its opening.

The release of Ca^{2+} from the ER is a nonlinear, cooperative process wherein IP3 binds to four receptor sites on the IP3R, one on each subunit of the tetramer (*26*). Small perturbations in conditions can cause uncoordinated bursts of local release across a cell. The brief opening of IP3R channels gives rise to localized Ca^{2+} pulses, called "sparks".

Ca^{2+} oscillations depend upon both the spatial organization of IP3Rs and their regulation by Ca^{2+}, while the links between IP3R activities and Ca^{2+} oscillations are not fully understood. Ca^{2+} regulates channel activity in a biphasic manner. Early studies demonstrated inhibition of IP3-mediated Ca^{2+} mobilization by micromolar concentrations of Ca^{2+} (*27*). Also the ER Ca^{2+} content preserve the capability to regulate the channel opening: in permeabilized hepatocytes, an increase in $[Ca^{2+}]_{er}$ enhances the sensitivity of IP3R for its ligand, also promoting spontaneous Ca^{2+} release, but the nature of this direct regulation and the protein involved are still a matter of debate (*28*). In this context, the tight spatial relationship between ER and mitochondria, and the capacity of the latter to rapidly clear the high $[Ca^{2+}]$ microdomain generated at the mouth of the IP3R, makes mitochondria an active player in the control of the IP3R function.

Whereas IP3 and Ca^{2+} are essential for IP3R channel activation, other physiological ligands, such as ATP, are not necessary but can finely modulate the Ca^{2+}-sensitivity of the channel (*29*). As for Ca^{2+}, the modulation of IP3R by ATP is biphasic: at micromolar concentrations, ATP exerts a stimulatory effect, while inhibiting channel opening in the millimolar range (*30*).

1.3.3 Mitochondrial Calcium Uniporter (MCU) complex

As described above, Ca^{2+} homeostasis is responsible for controlling a vast number of cellular functions. Mitochondrial Ca^{2+} uptake plays an essential role in the maintenance of homeostasis and participates in cellular metabolism, cytosolic Ca^{2+} buffering, secretory functions, cell survival, proliferation, migration and cell death (*31*). For many years, mitochondrial Ca^{2+} uptake was ascribed to a single transport mechanism mediated by an individual protein that functions as a uniporter; however, the uniporter was recently shown to be a macromolecular complex consisting of pore-forming and regulatory subunits, rather than a single protein (*32*).

The pore is physically formed by oligomers of MCU. MCU has two putative transmembrane domains, with C- and N-terminal domains spanning the mitochondrial matrix (*33*). The nuclear MCU gene, located on chromosome 10, encodes for a protein of 40 kDa but it loses its target sequence when it is imported into the mitochondria. The result is a mature 35-kDa

protein expressed in all tissues, capable of oligomerization, giving rise to a complex of higher molecular weight (*33*).

From the topological point of view, the MCU is located in the IMM, with the N-terminal and the C-terminus facing the matrix; there is a linker of 9 aa (the DIME domain) facing in the IMS between the two transmembrane domains. The DIME domain is essential for the Ca^{2+} transport because mutations inside it render the protein non-functional (*33*).

The overexpression of MCU increases mitochondrial Ca^{2+} uptake and sensitizes cells to apoptotic stimuli, and the employment of short interfering RNA (siRNA) silencing of MCU strongly reduced mitochondrial Ca^{2+} uptake. This reduction is specific for mitochondria, does not induce impairment of the electrochemical gradient or change in mitochondrial morphology and the induction of specific mutations at the level of the putative pore-forming region to reduce the mitochondrial calcium uptake and blocks the channel activity of the protein.

Mitochondrial calcium uptake protein 1 (MICU1) is an essential regulatory subunit of the complex; its discovery preceded the identification of MCU (*34*). MICU1 performs a gatekeeping function, stabilizing the closed state of the MCU complex and cooperating to allow Ca^{2+} to accumulate inside the mitochondria.

MICU2 shares 25% sequence identity with MICU1 and interacts with both MICU1 and MCU. The structure and function of this protein are still subjects of debate.

A 10-kDa single-pass membrane protein named efflux-multidrug resistance protein (EMRE) interacts with MICU1 and MCU oligomers. Thus, EMRE acts as a bridge between MICU1 activity and the channel proprieties of MCU; its loss drives the reduction of mitochondrial Ca^{2+} uptake to the same extent as MCU depletion (*35*).

MCUb is an MCU paralogue/isogene that acts as an endogenous dominant-negative isoform (*36*). The mRNA levels of MCUb are deficient when compared to MCU levels; this mRNA is highly expressed in the heart and lungs and little expressed in skeletal muscle. Variations of tissue-dependent accumulation of mitochondrial Ca^{2+} have been reported, and the Ca^{2+} influx in skeletal muscle is 28-fold higher than in cardiac mitoplasts (*37*).

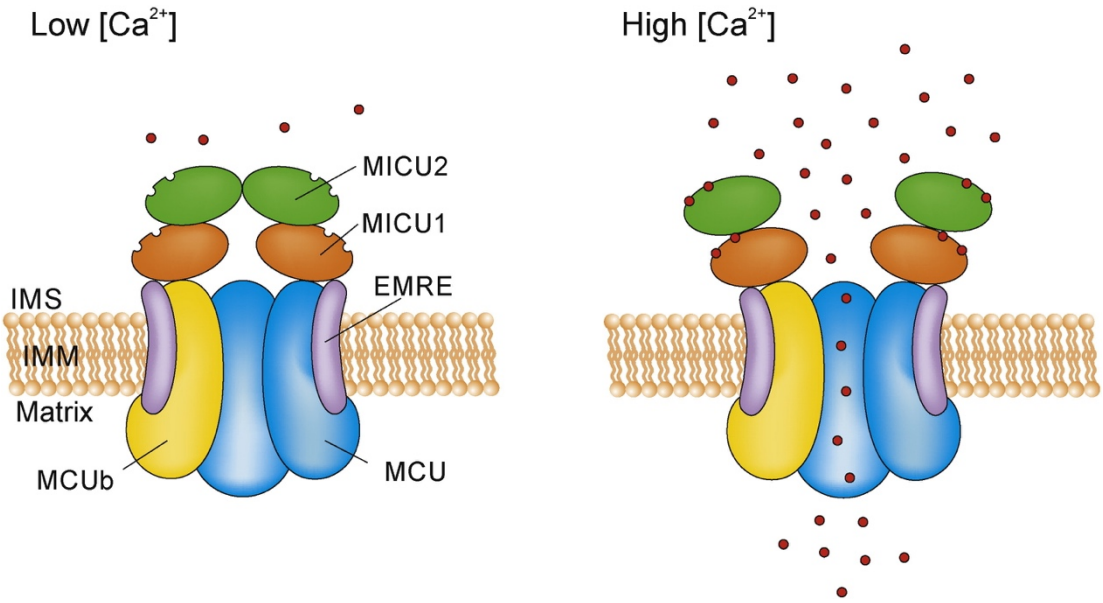

Figure 5 - Schematic representation of the different components of the mitochondrial uniporter complex. MCU comprises pore-forming and regulatory proteins. (Figure from Mammucari et al., BBA, 2016)

In 2012, it was also identified a regulator of MCU, CCDC90A or MCUR1 (mitochondrial calcium uniporter regulator 1), an integral membrane protein required for MCU-dependent mitochondrial Ca^{2+} uptake (*38*). MICUR1 interacts with MCU but not with MICU1, and these three proteins do not exist in the same complex. Therefore, the uniporter complex seems to be composed of MCU holomers, MCUb, MICU1, MICU2, and EMRE.

The latest work by Patron et al. also shows that MICU1 and MICU2 finely tune the MCU by exerting opposite effects on MCU activity; at low [Ca^{2+}] MICU2 largely shuts down MCU activity, at higher [Ca^{2+}] MICU1 allows the response of mitochondria to Ca^{2+} signals generated in the cytoplasm (*39*). Thus, MCU complex is essential for mitochondrial Ca^{2+} uptake, and the equilibrium of all the components maintains the normal cellular bioenergetics.

1.4 CALCIUM AND MITOCHONDRIA ARE ESSENTIAL REGULATORS OF CELL FATE

1.4.1 Mitochondria and Apoptosis

Cell death is a crucial and essential aspect of life. Although this statement may be contradictory, cell death itself is directly connected to cell proliferation and cell survival (*40*).

Programmed cell death has been established as an anti-cancer defense mechanism; therefore, any modification to the related pathways leads to uncontrolled cell proliferation and oncogenesis.

Early classifications of cell death were based on morphological assays, and apoptosis was one of the first processes to be described. The initial morphological observations were defined as the rounding-up of the cell, a reduction in cellular volume, chromatin condensation, cytoplasmic shrinkage, the retraction of pseudopods, nuclear fragmentation, and a particular boiling-like process termed blebbing (*41*).

Apoptosis is the most important and well-studied mechanism of cell death; approximately 10 million cells undergo the apoptotic process in an adult human under physiological conditions each day (*42*). At the same time, mitochondria are also essential checkpoints of the apoptotic process, as they may release caspase cofactors (*43*). Indeed, the apoptotic pathway is activated by the release of numerous mitochondrial proteins into the cytosol. Cytochrome c is undoubtedly the central player in the finely tuned apoptotic activation process. Typically, almost all cytochrome c is tightly bound to the mitochondrial inner membrane, thanks to its electrostatic interactions with acidic phospholipids, but a small fraction could exist loosely attached to IMM, available for mobilization.

Cytochrome c is considered an irreplaceable component of the mitochondrial electron transport chain, shuttling electrons from complexes III to IV, and is thus essential to life: the disruption of its only gene is embryonic lethal (*44*). Once released into the cytoplasm, this protein drives the assembly of caspases activating complex together with Apaf-1 (apoptosis–protease activating factor 1) and caspase 9, the so-called ‘apoptosome'. Cytochrome c, once in the cytosol, induces the rearrangement and heptaoligomerization of Apaf-1: each of these complexes can recruit up to seven caspase molecules, leading to their proteolytic self-processing and consequent activation (*45*).

A considerable number of other proapoptotic, intermembrane space-resident proteins, such as Smac/ DIABLO, AIF, HtrA2/Omi, and EndoG are contained into mitochondria HtrA2 (high temperature requirement protein A2) and DIABLO (direct inhibitor of apoptosis-binding protein with a low isoelectric point) both have an N-terminal domain that can interact and inhibit IAPs (inhibitor of apoptosis proteins). IAPs, such as XIAP, cIAP-1, and cIAP-2, are cytosolic soluble peptides that generally associate and stabilize procaspases, thus preventing their activation. Conversely, apoptosis-inducing factor and EndoG (endonuclease G) translocate from intermembrane space to the nucleus upon treatment with several apoptotic stimuli where they seem to mediate chromatin condensation and DNA fragmentation (*46*).

After ceramide treatment, the ER releases Ca^{2+} which is internalized into the mitochondria. As a consequence, organelle swelling and fragmentation were detected that were paralleled by the release of cytochrome c. These changes were prevented by Bcl-2 expression as well as experimental conditions that lowered $[Ca^{2+}]_{er}$ (*47*).

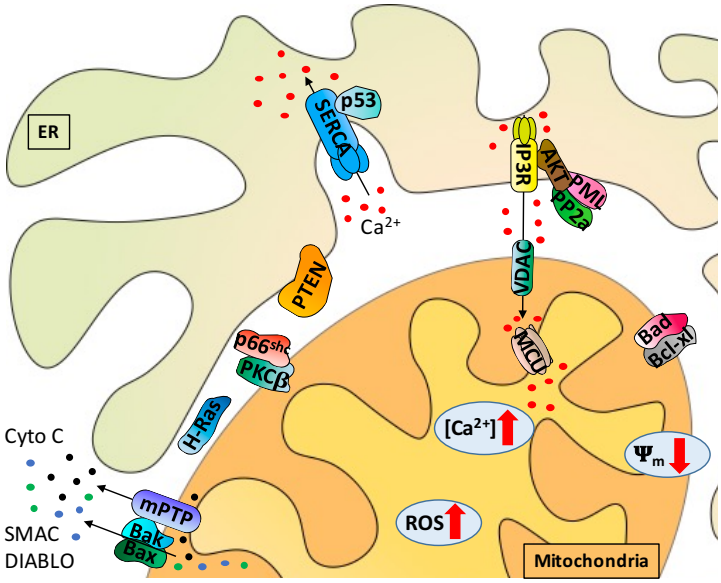

Figure 6 - Summary of the mitochondrial, ER and MAM proteins involved in apoptosis. The Bcl-2-protein family includes numerous anti-apoptotic (i.e., Bcl-XL) and pro-apoptotic (i.e., Bak, Bax, Bad) members. H-RAS reduces Ca2+ transfer from the ER to mitochondria and blocks the apoptotic program. The oncosuppressor PML regulates Ca2+-dependent apoptosis. PTEN interacts with IP3R in opposition to Akt phosphorylation of the receptors. p53 modulates apoptosis by controlling Ca2+ flux into the mitochondria. np66Shc and the putative oncogene PKC-β cooperate to conserve the physiological levels of apoptosis and autophagy. (Figure from Danese et al., BBA Bioenergetics, 2017)

The Bcl-2 protein family controls the intrinsic pathway of apoptosis. Proapoptotic Bax and Bak proteins exist as inactive monomers in viable cells with Bax localizing in the cytosol, loosely attached to membranes, and Bak residing in the mitochondrial fraction. Upon apoptosis induction, Bax translocates to mitochondria where it homo-oligomerizes and inserts in the outer membrane; similarly, also Bak undergoes a conformational change, which induces its oligomerization at the outer mitochondrial membrane. Together, these events trigger mitochondrial outer membrane permeabilization, the crucial process mediating the release of intermembrane space-resident caspase cofactors into the cytoplasm (*48*).

Mitochondria also undergo a morphological remodeling of their shape during the programmed cell death; after apoptosis induction, mitochondria become mostly fragmented, resulting in small, rounded and numerous organelles. This process occurs quite early in apoptotic cell death, soon after Bax/Bak oligomerization, but before caspase activation. Interestingly, the perturbation of the equilibrium between fusion and fission rates seems to

correlate with cell death sensitivity. In particular, conditions in which mitochondrial fission is inhibited, such as DRP1 (dynamin-like protein 1) downregulation or mitofusins overexpression, actively delay caspase activation and cell death induced by numerous stimuli. Similarly, stimulation of organelle fission (by DRP1 overexpression or Mfn1/2 and OPA1 inhibition) promotes apoptosis by facilitating cytochrome c release and apoptosome assembly (*49*). However, the relationship between mitochondrial fusion/fission and apoptosis is complex and mitochondrial fragmentation is not necessarily related to apoptosis. Indeed, mitochondrial fission per se does not increase cell death, and DRP1 overexpression has been reported to protect cells from some apoptotic challenges, such those dependent on mitochondrial Ca^{2+} overload.

A crucial event of the apoptotic process is the loss of mitochondrial membrane potential secondary to the opening of the mitochondrial permeability transition pore (mPTP), triggered by different pathological conditions. The availability of chemical mPTP inhibitors such as cyclosporine A and related compounds lacking the cytosolic inhibitory effect on calcineurin, as well as the development of cyclophilin D knockout mouse will help to clarify the role of mPTP in physiological and pathological condition and identify areas of pharmacological intervention in common disorders such as ischemia-reperfusion injury, liver diseases, neurodegenerative and muscle disorders. The OMM permeability and mPTP opening induced cell death, as well as happening consequently to elevated mitochondrial [Ca^{2+}], is also caused by reactive oxygen species (ROS) production and accumulation (*50*).

1.4.2 The autophagic process and its link with the mitochondrial compartment

In eukaryotic cells, there are two major systems that degrade cellular components: the ubiquitin-proteasome system (UPS) and the lysosomes. Unlike the UPS system that only degrades proteins which must be tagged by ubiquitin, the lysosomal system is responsible for degrading macromolecules, including proteins, and for the turnover of organelles by autophagy (*51*). The pivotal discovery of ATG genes has provided a significant breakthrough in the understanding of macroautophagy and of its functions in physiology and disease (*52*). There are mostly three types of autophagy; besides chaperone-mediated autophagy (CMA) the most important ones are micro and macroautophagy. The principal differences lie in the mode of transport: macroautophagy starts with the formation of a vacuole, known as the autophagosome, which sequesters cytoplasmic components, microautophagy consists of the direct uptake of portions of the cytoplasm by the lysosomal membrane. Autophagosome nucleation, which is the first step of autophagosome formation, requires BECLIN1. The interaction of BECLIN1 with VPS34 is known to promote the

catalytic activity of VPS34 and increase levels of PI(3)P, but is dispensable for the normal function of VPS34 in protein trafficking or recruitment of endocytic events.

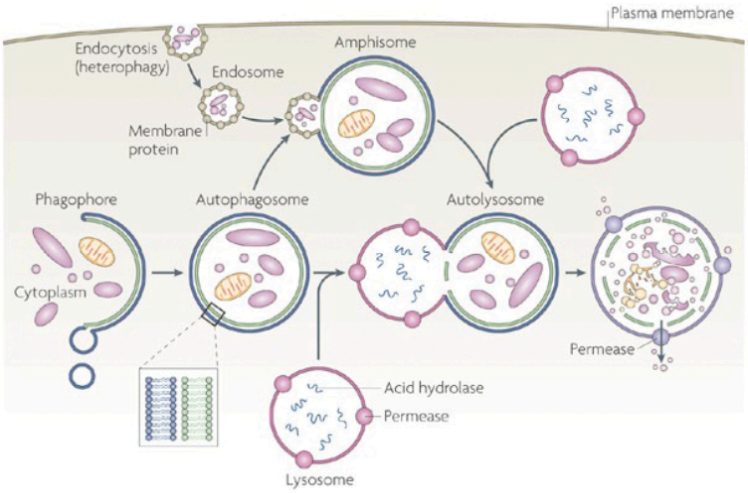

Figure 7 - Different stages of the autophagic process. From the left, phagophore starts to engulf cytoplasmatic materials such as proteins and organelles, then, phagophore is sealed to form autophagosome. This new organelle is fused with lysosome forming a transient structure called autophagolysosome, in which low pH and proteases digest all the material to recycle aminoacids and other molecules.

Depending on the proteins recruited by BECLIN1, class III PI3K complexes differentially regulate the process of autophagosome formation. BECLIN1 complex binding partner acting as positive autophagy regulator are: ATG14L, UVRAG, AMBRA1, BIF1, PINK1, VMP1, HMGB1.81 In contrast to these positive regulators, there are negative regulators among Beclin1-interacting partners such as RUBICON, BCL-2, and BCL-XL (*53*).

The simultaneous elongation and nucleation of the phagophore are to be considered the expansion of the isolation membrane. Two ubiquitin-like protein conjugation systems are involved in the development of autophagosome membranes, the ATG12-ATG5, and the ATG8- phosphatidylethanolamine (PE). The ATG12-ATG5 conjugate further interacts with ATG16 to form a ~350 kDa multimeric ATG12-ATG5-ATG16 protein complex through the homo-oligomerization of Atg16. The second ubiquitin-like protein conjugation system is the modification of ATG8 by PE, a crucial process for the formation of autophagosome. ATG8 is cleaved by cysteine protease ATG4 and then conjugated with PE by ATG7 and ATG3, a second E2-like enzyme. This lipidated ATG8-PE then associates with newly forming autophagosome membranes.

The conversion of ATG8 to ATG8-PE is thus well-known as a marker of autophagy induction. ATG8 is represented by at least eight members that can be divided into two subgroups based on their amino acid sequence homology: the microtubule-associated protein

1 light chain 3 (LC3) family (LC3A, LC3B, LC3B2 and LC3C) and the GABA(A) receptor-associated protein (GABARAP) family.

Finally, autophagosome fuses with lysosomes or vacuoles, and the sequestration of cytoplasm into a double-membrane cytosolic vesicle is followed by the fusion of the vesicle with a late endosome or lysosome to form an autophagolysosome (or autolysosome). Autophagy is one of the major responses to stress in eukaryotic cells and is implicated in several pathological conditions such as infections, neurodegenerative diseases, and cancer (*54*). Autophagy and mitochondria are closely linked by the selective elimination of excess or damaged organelles, a process called mitophagy. Mitochondria are degraded under a variety of different conditions, including mitochondrial dysfunction, basal mitochondrial quality control and during developmental operations (i.e., during the maturation of immature red blood cells) (*55*). To date, considerable progress has been made in identifying mitophagic adaptors on the degradation of parental mitochondria after fertilization and understanding the overall importance of mitophagy for aging and neurodegenerative diseases.

Mitochondrial depolarization can occur naturally during mitochondrial fission or can be induced through cellular stress pathways, including apoptosis. After extensive damage, mitochondrial membranes can be permeabilized through distinct routes, and mitochondrial membrane permeabilization (MMP) constitutes one of the hallmarks of apoptotic or necrotic cell death (*43*).

However, if the mitochondrial insult is not too severe and only a fraction of the mitochondrial pool is damaged, the cell can be saved from death through the mitophagic degradation.

The voltage-sensitive kinase PINK1 is the marker that allows recognizing damaged mitochondria. Usually, PINK1 is continuously degraded on mitochondria, but with the drop of membrane potential, PINK1 is stabilized on the outer mitochondrial membrane (*56*). After PINK1 rapid accumulation on the mitochondrial surface, recruitment of Parkin (an E3 ligase to mitochondria) occurs, where it ubiquitinates multiple mitochondrial proteins, including Mfn1/2 and the VDAC1 protein. The accumulation of ubiquitin-modifications is thought to facilitate the recruitment of the autophagy adaptor p62, eventually leading to the autophagosomal degradation of the damaged mitochondrion (*57*). Mutations in the genes coding for both PINK1 and Parkin were identified in the early-onset forms of Parkinson disease. In cell culture models, disease-associated mutants of PINK1 and Parkin dramatically reduced the recruitment of Parkin to damaged mitochondria and their subsequent degradation (*58*).

In addition to mitophagy-mediators, the loss of general autophagy regulators, like ATG5 or ATG7, also leads to significant accumulation of damaged mitochondria, further supporting the idea that autophagy plays a crucial role in mitochondrial quality control, to ensure the health of the mitochondrial network (*59*).

Mitochondrial depolarization/fragmentation are two common prerequisites for mitophagy, and mitochondrial fusion can block mitophagy. This intimate link between mitochondrial shape and degradation suggests that both processes could also be coupled on the molecular level. Indeed, two different systems were identified that affect both mitophagy and mitochondrial form. Even though it is now well-known that mitochondrial dynamics and mitophagy are tightly linked by several means, it will be essential to understanding all the pathways that directly affect the mitochondrial shape, in relation to this particular degradation process.

1.4.3 MCU complex and the role of its components in tumorigenesis

Mitochondrial Ca^{2+} overload has been associated with apoptosis and necrosis in many pathological conditions, and as a mitochondrial Ca^{2+} uniporter, MCU has many pathophysiological implications. When a pro-apoptotic stimulus occurs, MCU-expressing cells display an enhanced sensitivity to apoptosis. Moreover, inhibition of the pathway that activates the MCU complex by phosphorylating the uniporter through Ca^{2+}/calmodulin-dependent protein kinase II (CaMKII) and protein tyrosine kinase 2 beta (Pyk2) prevents Ca^{2+} overload in mitochondria, reactive oxygen species (ROS) production, and cell death (*60*).

Then, MCU complex is essential for mitochondrial Ca^{2+} uptake, and the equilibrium of all the components maintains the normal cellular bioenergetics. Therefore, modulation of the expression of MCU complex subunits could improve our understanding of the possible pathogenic role of the uniporter.

As shown in our previous study, microRNA-25 (miR-25) is up-regulated in human prostate and colon cancers and targets the MCU gene. miR-25 decreases MCU expression and, consequently, reduces mitochondrial Ca^{2+} uptake and resistance to Ca^{2+}-dependent apoptotic death (*61*).

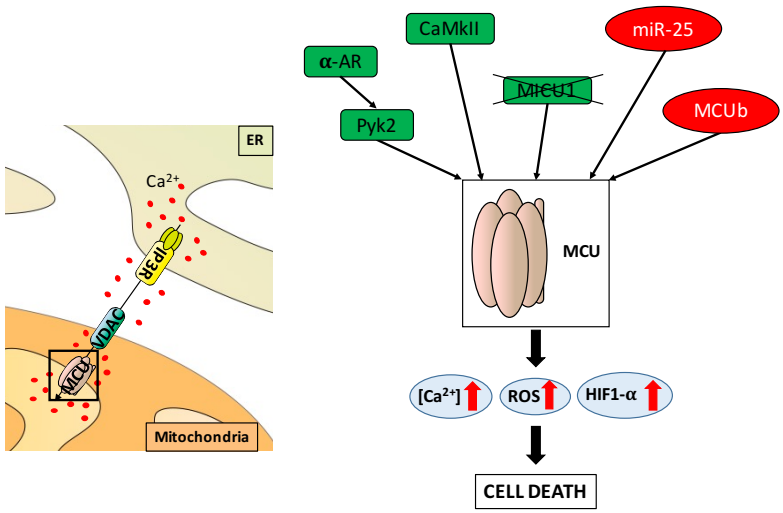

Figure 8 - Proteins that modulate MCU complex activity and cell death. Ca2+ uptake is performed by the MCU located in the IMM. Modulation of MCU complex subunits and function could make cells highly subject to apoptotic cell death in stress conditions because of increased basal ROS levels during mitochondrial Ca2+ uptake. In green are proteins that promote the entry of Ca2+ into the mitochondria; in red are proteins that decrease mitochondrial Ca2+ absorption and ROS generation. Inhibition of the pathway that activates the MCU complex by phosphorylating the uniporter through CaMKII and Pyk2 prevents Ca2+ overload in mitochondria, ROS production, and consequent cell death, which could be important in tumor progression. MICU1 knockout cells have increased basal ROS levels during mitochondrial Ca2+ uptake, leading to apoptotic cell death in stress conditions. In contrast, miR-25 (which decreases MCU expression) and MCUb (which acts as an endogenous dominant-negative isoform of MCU) reduce mitochondrial Ca2+ uptake and, consequently, drive resistance to Ca2+-dependent apoptotic death. (Figure from Danese et al., BBA Bioenergetics, 2017)

Elevated mitochondrial [Ca^{2+}] and ROS accumulation via MCU activity may induce cell death by increasing OMM permeability and the opening of the mPTP (*50*). MCU overexpression rises mitochondrial ROS generation and accumulation and, conversely, silences MCU or inhibits its activity through the introduction of the dominant-negative subunit MCUb, decreasing mitochondrial ROS generation induced by various stimuli (*62*). MICU1 knockout cells lose their MCU complex gatekeeping function and are highly susceptible to apoptotic cell death under stress conditions because of the increased basal ROS levels during mitochondrial Ca^{2+} uptake (*63*).

A recent study from the University of Padua highlights a possible role of MCU in the regulation of breast cancer progression via hypoxia-inducible factor-1α (HIF-1α). MCU and HIF-1α expression are suggested to be directly related; moreover, HIF-1α-regulated genes are expressed in human breast cancer samples, which is sufficient to consider MCU as a novel marker of cancer progression (*64*).

2. PATHOLOGICAL MITOPHAGY DISRUPTS MITOCHONDRIAL HOMEOSTASIS IN LEBER'S HEREDITARY OPTIC NEUROPATHY

2.1 ABSTRACT

Leber's hereditary optic neuropathy (LHON) has been the first human disease associated with a maternally inherited missense mutation in mitochondrial DNA (mtDNA), and is the most frequent mitochondrial disease. This disorder is characterized by the selective degeneration of retinal ganglion cells (RGC), the terminal retinal neurons projecting their optic nerve-forming axons to the brain, which ultimately results in blindness. It was previously demonstrated that compensatory activation of mitochondrial biogenesis successfully drives incomplete penetrance, and that increased oxidative stress and propensity to apoptosis characterize mutant cells.

In this study, as counterpart to mitochondrial biogenesis, we explored the role of autophagic and compartment-specific mitophagic activity in LHON using fibroblasts, fibroblast-derived cytoplasmatic hybrids (cybrids) and induced Pluripotent Stem Cells (iPSCs)-derived neurons. We found that these LHON cellular models of increasing complexity, displayed a sustained activation of the autophagic process, a pathologically increased mitophagic activity, and an alteration of several mitochondrial readouts including reactive oxygen species (mROS) production, mitochondrial network and bioenergetics. To counteract these pathological features, we used compounds such as autophagy-regulators (3-methyladenine, clozapine and chloroquine) and modulators of mitochondrial activity (idebenone), observing the rescue of all the pathological phenotypes observed under naïve conditions.

Overall, our findings suggest that auto/mitophagy plays a key role in the pathogenic mechanisms leading to LHON, most importantly, representing a primary target for blocking the progressive optic nerve degeneration and the consequent reduction of vision.

2.2 INTRODUCTION

Leber's hereditary optic neuropathy is amongst the most frequent mitochondrial disorders (*65, 66*) and has been the first to be associated with maternally inherited missense mutations of mitochondrial DNA (mtDNA) (*67*). This blinding disease is peculiar in affecting very selectively only the retinal ganglion cells (RGCs), the neurons that originate the optic-nerve forming axons, which undergo a catastrophic wave of neurodegeneration leading subacutely to optic nerve atrophy and severe reduction of central vision (*68, 69*). Usually, one of three common LHON mtDNA mutations, invariably affecting ND subunits of complex I, is found in homoplasmic state (100% mutant mtDNAs) in all individuals along the maternal lineages. However, only a few individuals become affected (incomplete penetrance), most frequently young males (gender prevalence) (*68, 69*). Complex I dysfunction induced by LHON mutations reduces the bioenergetic efficiency of oxidative phosphorylation (OXPHOS) (*70, 71*) and increases reactive oxygen species (ROS) production (*72-74*). Under *in vitro* conditions forcing cells to rely on OXPHOS for energy production, such as switching cell culture medium from glucose to galactose as carbon source, LHON-mutant cells lose viability and undergo apoptotic death (*75, 76*). Recent *ex-vivo* (blood cells, muscle biopsies and post-mortem retinal and optic nerve specimens) and *in vitro* (fibroblasts) evidences indicate that increased mitochondrial biogenesis is a compensatory strategy operated by cells to contrast the defective phenotype induced by LHON mtDNA mutations (*77*).

Tissue specificity in LHON has been proposed as due to the unique characteristic of RGC axons, which are unmyelinated for the long, initial stretch of their intra-retinal tract, turning myelinated as soon as they cross the lamina cribrosa at the optic nerve head (*68, 69*). This imposes an asymmetric energy dependence that is reflected in different mitochondrial densities and dynamics needed for their correct distribution along the RGC axons. Thus, the compensatory response based on increased mitochondrial biogenesis needs to be considered within the anatomical context of this neuronal cell type. In fact, small RGCs with smaller axons are the most sensitive to the defective mitochondrial metabolism in LHON (*78, 79*), and larger or smaller anatomical conformation of the optic disc has been found to be, respectively, a protective or a risk factor to become affected or suffer a more severe disease (*80*). However, the discriminating point affecting the two major unexplained features, male prevalence and incomplete penetrance, remains currently centred on the efficient compensatory increase in mitochondrial biogenesis (*77*). In fact, estrogens activate mitochondrial biogenesis, providing a hint for the clear protection displayed by females (*81*). More broadly, the higher efficiency that some LHON mutation carriers, besides the

gender, display in activating compensatory mitochondrial biogenesis, predicts the risk of developing the disease, leaving them lifelong unaffected (*77*). This efficiency is most probably determined by specific, still unknown, genetic variants (*82*), but is also highly modulated by the interaction with environmental factors such as tobacco and alcohol exposure, as recently highlighted (*83, 84*). Overall, the scenario of LHON penetrance remains extremely complex and only partially understood.

Mounting evidence indicates that mitochondrial biogenesis is deeply interlinked to a larger master program regulating mitochondrial homeostasis and life cycle (*85*). The counterpart of mitochondrial biogenesis is mitochondrial clearance, which is largely coincidental with elimination of damaged mitochondrial by autophagy, i.e. mitophagy (*86*). The execution of mitophagy and its role in the pathogenesis of LHON, as well as how mitophagy participates to the compensatory mechanisms, are mostly unknown. This prompted us to undertake the current study, aimed at completing the elucidation of the full program regulating mitochondrial homeostasis in LHON and how this is disturbed by the LHON-related complex I dysfunction. Understanding the full picture paves the road to the modulation of this program for therapeutic purposes.

2.3 RESULTS

2.3.1 Autophagy and mitophagy are pathologically increased in fibroblasts from LHON affected patients, but not in unaffected mutation carriers

The starting point of our study was to investigate how autophagy and mitophagy may be affected by LHON mutations in patient-derived fibroblast cell lines, and how the quality control mechanisms are coordinated and balanced with mitochondrial biogenesis.

We assessed the levels of autophagic activity in fibroblasts from LHON affected patients and unaffected carriers of the LHON mutation (from herein defined as carriers). We thoroughly analyzed the two most frequent LHON mutations, the m.11778G>A/MT-ND4 and m.3460G>A/MT-ND1, but similar findings in most cases also applied to the m.14484T>C/MT-ND6 mutation.

Light chain 3 (MAP1LC3, hereafter referred to as LC3), a mammalian homolog of yeast Atg8, is used as a specific marker to monitor autophagy. During autophagy, the cytoplasmic form (LC3-I) is processed to a cleaved and lipidated membrane-bound form (LC3-II), which is localized to the autophagosome (*87*). We have assessed this conversion by immunoblotting with antibodies against LC3, which usually reveals two bands: LC3-I (16 kDa) and LC3-II (14 kDa). The amount of LC3-II correlates well with the number of autophagosomes. The LC3 conversion is also monitored through live microscopy analysis by transfecting cells with the green fluorescent protein (GFP)-LC3 reporter. After autophagy induction, labeled autophagosomes can be visualized as ring-shaped or punctate structures (*88*). As an additional autophagy marker, we used the protein SQSTM1/p62, which is inversely correlated with autophagic activity because it is selectively incorporated into autophagosomes via an interaction with LC3; thus, it is efficiently degraded by autophagy (*89*). We found that in basal conditions fibroblasts from LHON affected patients displayed a sustained activation of the autophagic process when compared to control cells, as demonstrated by an increased amount of lipidated membrane-bound form of the marker LC3 and by a significant reduction in p62 levels (Figures 9A, 9B, and 9C). To confirm these data, we used a condition of serum starvation (EBSS 30 min), known to promote the activation of the autophagic machinery (*90*). Under these conditions, control fibroblasts significantly activated autophagy whereas LHON fibroblasts did not respond similarly, suggesting that they already have a high autophagic activity. Autophagic measurements through fluorescent microscopy using the GFP-LC3 probe confirmed these findings, highlighting a large number of green punctate structures in LHON fibroblasts (Figures 9A, 9B, and 9C). Interestingly,

LHON carrier fibroblasts showed a lower autophagic activity, despite the presence of the homoplasmic mutation. (Figure 9C).

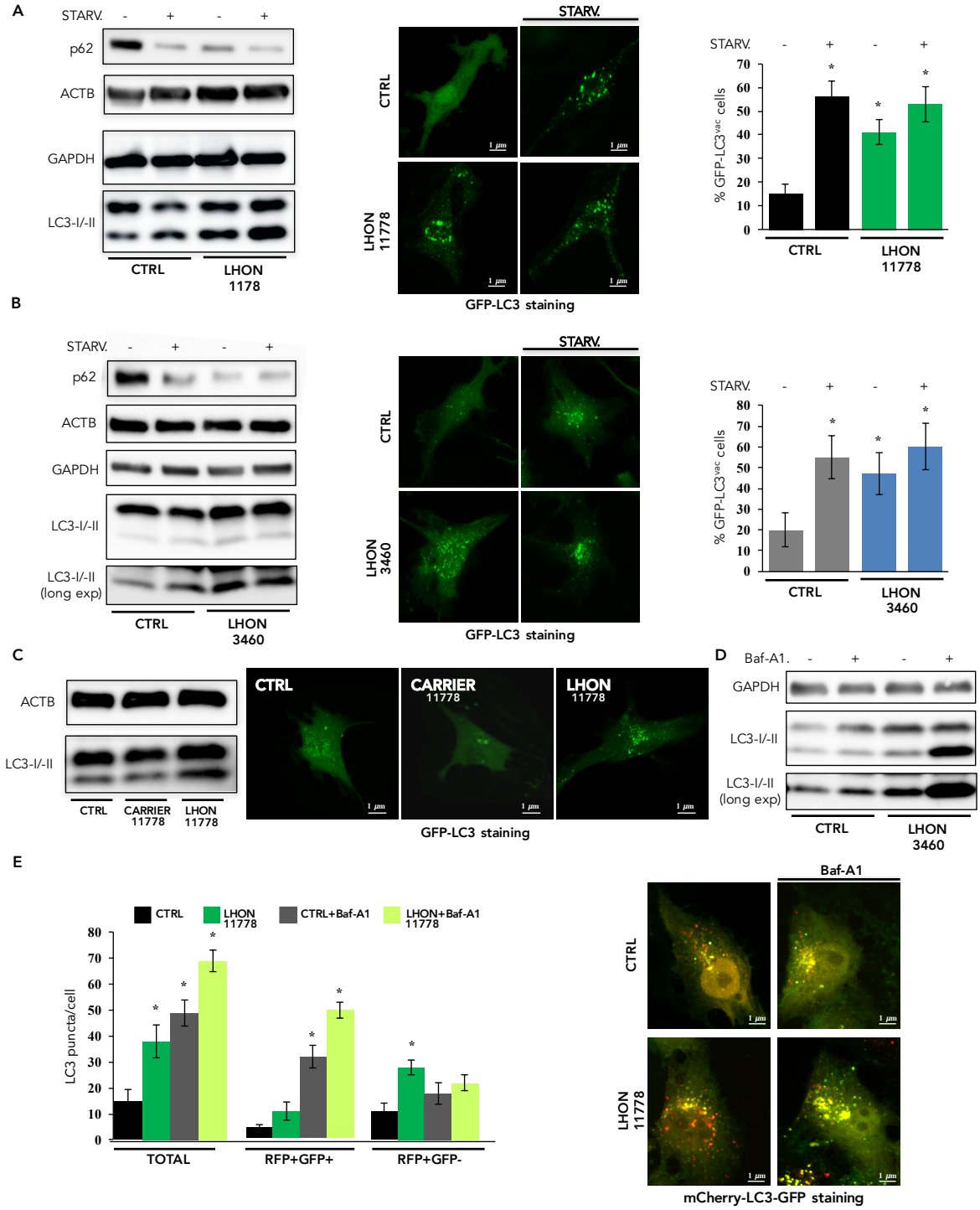

Figure 9 - Autophagy is pathologically increased in fibroblasts from LHON affected patients, but not in unaffected mutation carriers. A, B and C left panel: Detection of autophagic activity through immunoblot on LHON fibroblasts carrying m.11778G>A/MT-ND4 mutation (A and C) m.3460G>A/MT-ND1 mutation (B). N = 3 indipendent experiments. **A, B and C central panel**: Fibroblasts were transfected with a GFP-LC3-encoding plasmid and cultured in complete medium for 36 h. **A and B right panel:** GFP-LC3 punctae count. Where indicated, the cells were starved (STARV.) for 1 h. **D**: Autophagic flux analysis using a Bafilomycin A1 treatment in complete medium for 2h. **E:** Cells expressing mCherry-GFP-LC3 are evaluated on the relative ratio of mCherry/EGFP fluorescence which changes in response to the pH gradient as autophagosomes fuse with lysosomes to form autolysosomes (autophagic flux). Cells were treated with Bafilomycin A1 in complete medium for 2h. N = 20 visual fields per condition. * $p<0.05$

A common misconception is that increased number of autophagosomes invariably corresponds to an increased cellular autophagic activity. Autophagosomes accumulation, and thus, increased levels of autophagosomal marker LC3, may represent either autophagy induction or impaired degradation of autophagosomes. Consequently, in both conditions, the number of autophagosomes is increased (Mizushima, Yoshimori et al. 2010). To distinguish between these two scenarios, we performed autophagic flux analysis in control and LHON fibroblasts evaluating the induction of autophagy in the presence of Bafilomycin A1 (Baf A1), an inhibitor of the late phase of autophagy. Bafilomycin A1 prevents maturation of autophagic vacuoles by inhibiting fusion between autophagosomes and lysosomes. We found that treatment with BaF A1 induces abundant accumulation of the cleaved form of LC3 when compared to the untreated conditions. Noticeably, this occurs equally in control and LHON mutant fibroblasts (Figure 9D and 9E), indicating that the autophagic response is unaffected in our experimental condition. Taken together, these results demonstrate that the autophagic machinery is intrinsically activated in LHON mutant cells from affected individuals, whereas a compensatory mechanism operates in carriers, which behave similarly to control cells. However, autophagy also exists in selective forms, which in the case of mitochondria remove damaged organelles through the targeted process of mitophagy. Thus, we assessed the occurrence of mitophagy in control and LHON fibroblasts. The main method used to measure mitophagy is based on the simultaneous visualization of mitochondria as labeled by the mitoprobe MitoTracker green, and autophagolysosome as stained by the lysosome probe Lysotracker red, both imaged by confocal fluorescent microscopy (*91*). As shown in Figure 10A and B, mitophagy was activated only in LHON fibroblasts from affected individuals as compared with control and carrier fibroblasts owing the m.11778G>A/MT-ND4 mutation. A further confirmation has also been obtained through the use of transmission electron microscopy. Electron microscopy remains one of the most accurate methods for the detection of autophagy and quantification of autophagic accumulation; consequently, auto/mitophagic compartments can be identified by morphology. High mitophagic activity levels have also been founded through the use of this technique. (Figure 10C)

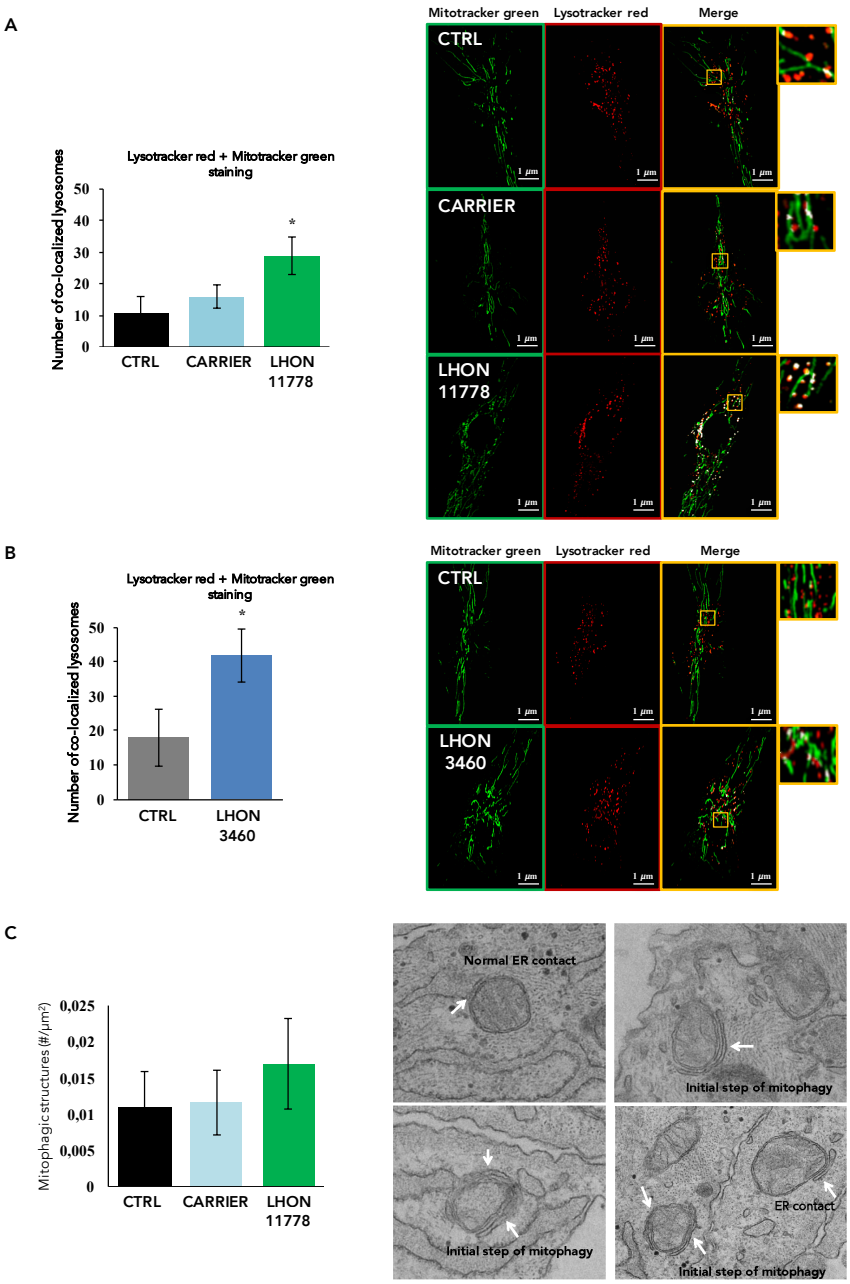

Figure 10 - LHON mutations drive to an increased mitophagic activity only in phenotype-manifesting patients. A and B: Confocal microscopy assessment of mitophagy in control, carrier and mutant fibroblasts harboring LHON mutations. Before experiments, control (CTRL), carrier and mutated cells (LHON) were loaded with LysoTracker Red (final concentration = 1 μM) and MitoTracker Green (final concentration = 1 μM) and incubated for 15 min to visualize lysosomes and mitochondria, respectively. The degree of the signal of lysosomes with mitochondria (merge) was calculated via cell live imaging microscopy. Sequentially zoomed regions (insets) from the fluorescent confocal merge images illustrate the lysosome (red signal) and mitochondria (green signal) colocalization, appearing as white areas indicative of mitophagy. Graphs represent the amount of colocalization between lysosomes (red signal) and mitochondria (green signal).. **C:** Electron microscopy analysis of mitophagic structures in CTRL and LHON fibroblasts, to assess mitophagic activity. N = 15 visual fields per condition. Data are presented as means ± SEM. *p < 0.05.

2.3.2 Complex I deficiency leads to altered mitochondrial function and network morphology in LHON affected individuals, which is partially compensated in carriers

Previous studies have shown that LHON mutations lead to impaired complex I-dependent ATP synthesis, increased oxidative stress, and increased sensitivity of cells to undergo apoptosis (*70, 72, 73, 75, 76*). To better define the mitochondrial dysfunction in fibroblasts we assessed cell respiration boosted by various substrates, complex I redox activity, mitochondrial membrane potential (Ψ_m), ROS production, and mitochondrial network morphology.

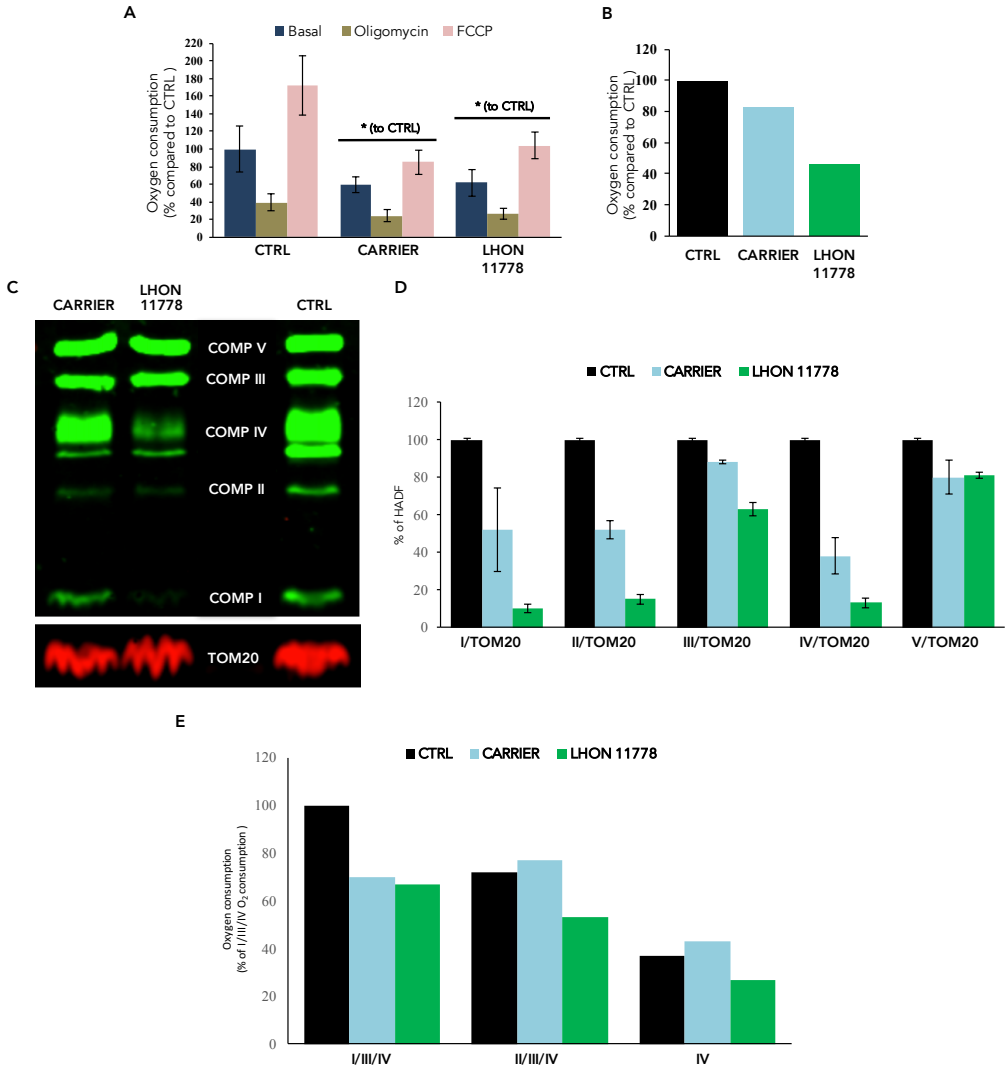

Figure 11 - Measurement of the oxygen consumption in intact and permeabilized human fibroblasts. A: Oxygen Consumption Rate (OCR) measured through micro-oxygraphy technique (SeahorseXF96 flux analyzer). Analysis of individual parameters for basal respiration, ATP production, and maximal respiration rate. Fibroblasts were seeded to 40,000 cells/well and incubate for 24 h. Oxygen consumption rate was measured in XF base medium supplemented with individual glutamine, glucose, sodium pyruvate, followed by the sequential addition of oligomycin (0.5 µM) and FCCP (1 µM). N = 3 independent experiments. **B:** OCR in human fibroblasts measured with a Clark electrode. **C:** Blue-native PAGE and complex I in-gel activity assay. The blue-native PAGE gels were immunoblotted with antibodies directed against specific individual subunits to assess the amount of each of the five fully assembled OXPHOS complexes. **D:** Quantification of the individual respiratory chain complexes rate normalized to the TOM 20 protein level. **E:** Measurement of individual respiratory chain complexes activity based on oxygen consumption measurements. Data are presented as means ± SEM. *p < 0.05

To evaluate cell respiration, we analyzed in real time the global Oxygen Consumption Rate (OCR) through micro-oxygraphy technique (SeahorseXF96 flux analyzer). OCR was measured under basal conditions and in the presence of oligomycin to evaluate ATPase inhibition, and FCCP (Carbonyl cyanide 4-(trifluoromethoxy)phenylhydrazone) to measure uncoupled stimulated respiration. The LHON mutant fibroblasts were significantly reduced for each of the respiratory conditions compared to control fibroblasts, confirming a defective respiratory function (Figure 11A). This also applied to the carrier fibroblasts, which displayed a reduced respiration comparable to that of patients' fibroblasts (Figure 11A). To further investigate on mitochondrial respiration the OCR in human fibroblasts was also measured with a Clark electrode. Obtained outcomes seem to support the Seahorse measurement results. Carrier cells have a bit lower basal respiration, measured in intact fibroblasts. LHON fibroblasts have markedly decreased basal respiration indicating an OXPHOS defect (Figure 11B). To deepen the contribution given by each respiratory chain complex, we decided to quantify the individual respiratory chain complexes concentration in cellular protein extracts (Figure 11C). Individual respiratory chain complexes assay (normalized to the TOM 20 protein level) show decreased levels of complexes I, II and IV in carrier and LHON fibroblasts; however, the decrease in carrier fibroblasts seem to be moderated. In LHON fibroblasts the level of above-mentioned complexes was dramatically lower (below 20% of control values). Moreover, the level of complex III is decreased to around the 60% in LHON fibroblasts and 85% in the carrier.

Analyzing complex V, both fibroblasts obtained from the carrier and LHON patients had a similar level (Figure 11C). In parallel, we measured (through the use of glutamate, malate, succinate and ascorbate as substrates and rotenone, antimycin A and azide as inhibitors) the individual respiratory chain complex activity, based on oxygen consumption measurements. Carrier and LHON fibroblasts have, as expected, a reduced respiration rate based on substrates for Complex I. When respiration is supported with succinate (substrate for Complex II), carrier fibroblasts have a good oxygen consumption rate (comparable to control cells), however LHON fibroblasts still have a relatively low respiration with succinate dependent-respiration (Figure 11E). This data indicates that mitochondria from carrier patients display an exclusive complex I deficiency. Measurement of Complex IV related oxygen consumption rate showed that LHON fibroblasts have a defect in Complex IV activity too.

Therefore, LHON fibroblasts are characterized by a decreased Complex I and Complex IV activity, while fibroblasts from carrier patients display a defect only on Complex I (Figure

11E). These data are fully supported by the data showing the level of individual respiratory chain complexes presented on Figure 11C: LHON fibroblasts are characterized by decreased Complex I and Complex IV levels. This could be one determining factor in patients exhibiting the disease phenotype.

Coupling of electron transfer with proton translocation through the activities of Complexes I to IV of the respiratory chain builds the electrochemical gradient across the inner mitochondrial membrane that sustains the mitochondrial membrane potential (Ψ_m) (*92*).

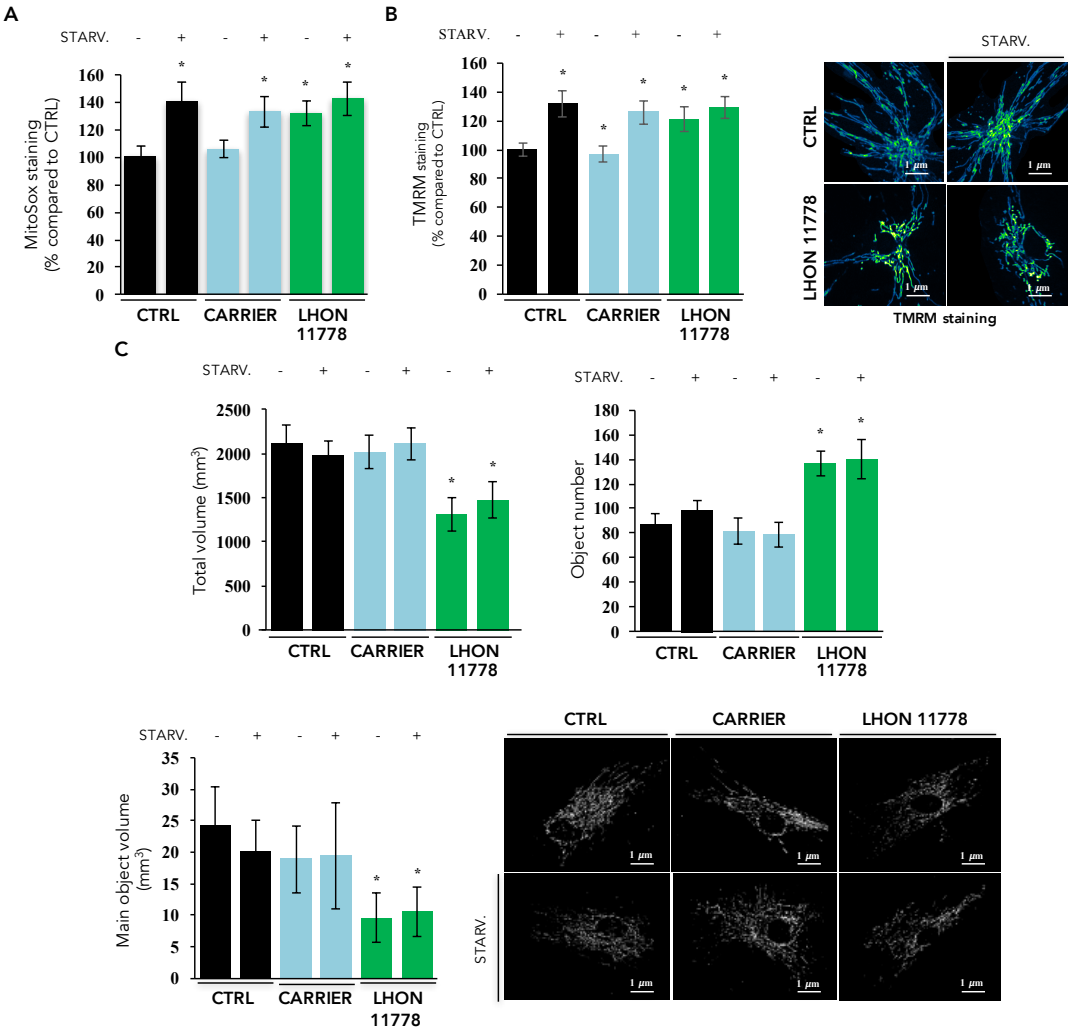

Figure 12 - Complex I deficiency leads to altered mitochondrial function and network morphology in LHON affected individuals, which is partially compensated in carriers. A: Measurement of mitochondrial ROS production in LHON-derived fibroblasts by using MitoSOX Red probe. **B**: The mitochondrial transmembrane potential (Ψ_m) of control (CTRL), carrier and LHON fibroblasts was detected by using the Ψ_m-sensitive probe TMRM. After imaging, the Ψ_m was depolarized by the mitochondrial uncoupler FCCP. When indicated, the cells were starved (STARV.) for 30 min before TMRM loading.
C: Cells were labeled with a red-fluorescent dye that stains mitochondria in live cells (MitoTracker Red), and the mitochondrial volume, number, and volume of single organelle was studied. Images acquired by confocal microscopy were deconvolved, 3D reconstructed and quantitatively analyzed. Where indicated, the cells were starved for 30 min. N = 15 visual fields per condition. Quantitative results (means ± SEM; $p < 0.01$) are depicted. *$p < 0.05$.

We evaluated the Ψ_m in LHON fibroblasts with Tetramethylrhodamine methyl ester (TMRM), a cell-permeant cationic red fluorescent dye that is readily sequestered by active mitochondria. As reported in Figure 12B, we found that Ψ_m in LHON fibroblasts appeared significantly increased. Moreover, the starvation treatment increased Ψ_m in control cells, at levels comparable to those of LHON cells in resting conditions, whereas it failed to exert any effect on LHON fibroblasts that remained hyperpolarized similar to the resting conditions (Figure 12B).

Complex I dysfunction is commonly associated with a mitochondrial increase of ROS production (mROS). We assessed mROS by using MitoSOX Red, a fluorogenic dye specifically targeted to mitochondria in live cells; this dye permeates live cells where it selectively targets mitochondria and is rapidly oxidized by superoxide. The oxidized product is highly fluorescent upon binding to nucleic acid. Fibroblasts with LHON mutations revealed higher levels of mROS compared to controls and starvation treatment, as expected, further increases these levels (Figure 12A).

Mitochondrial function is tightly linked to balanced dynamics of mitochondrial fission and fusion, regulating the mitochondrial network morphology. We assessed the mitochondrial structure and morphology by using MitoTracker fluorescent probes. Cells were analyzed in a confocal fluorescence microscope and, after deconvolution and 3D reconstitution, the images were analysed by evaluating three main aspects: the total network volume, the mitochondria number per cell and the main mitochondria volume. Fibroblasts from LHON affected individuals displayed a prevalent fragmented network compared to control cells (Figure 12C), with reduced total and individual mitochondrial volume and increased number of single mitochondria. The fibroblasts from carriers were similar to controls. These results highlight that LHON cells present a mitochondrial network morphology typically seen under stress conditions, whereas carriers can compensate despite the evidence of a respiratory deficiency, maintaining a fairly normal interconnected networking of mitochondria.

2.3.3 Pathological increase of autophagy and mitophagy, as well as defective mitochondrial function and network morphology, are co-transferred with mtDNA into the cybrid cell model

To establish if the pathological increase of autophagy/mitophagy and, more globally, if the functional mitochondrial alterations seen in fibroblasts derived from affected LHON patients are prominently driven by the mutant mtDNA, we evaluated these readouts on the cytoplasmic hybrid (cybrid) cell model, which is obtained by fusing Rho-zero cells (cells depleted of their own mtDNA) with patient-derived cytoplasts. In fact, cybrids remain a

valuable model to investigate the mtDNA-dependent phenotype, dissected from the influence of the original nuclear background of the patient. Nevertheless, cybrid cells also present several limitations: they are immortalized cells derived from cancer, not representative the LHON target tissue, which can mutate over time or adapt to the mutant mtDNA genotype.

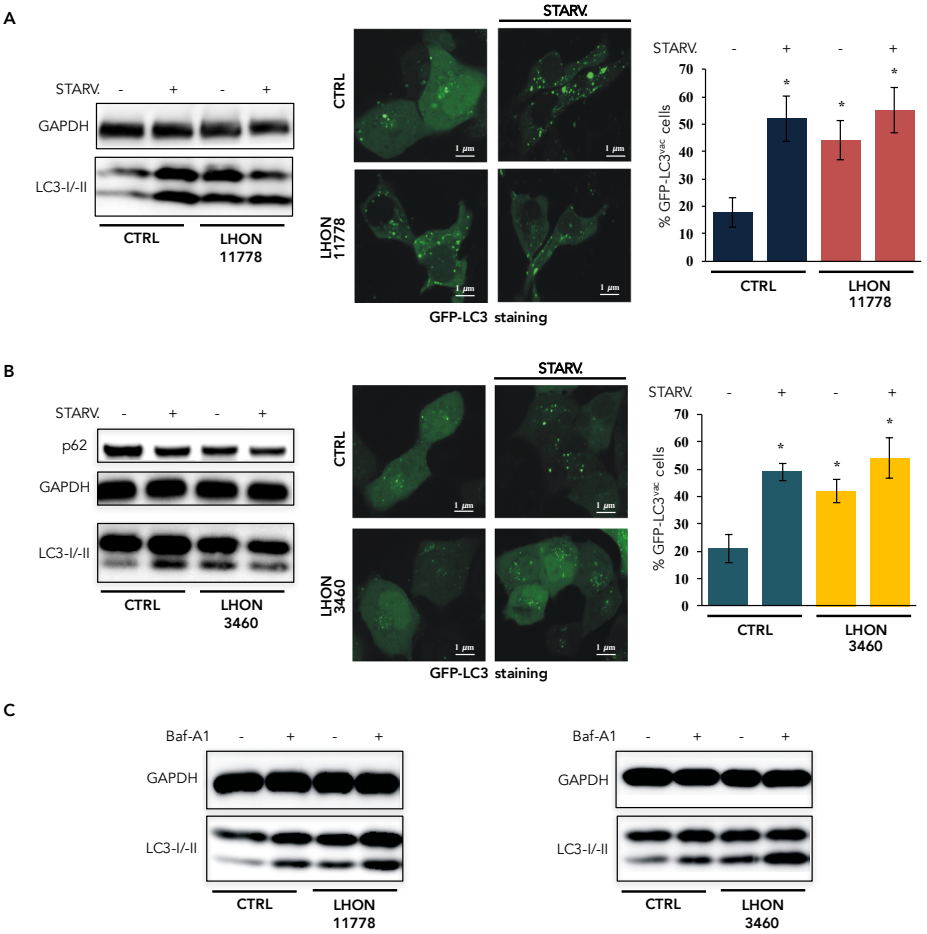

Figure 13 - Autophagy results increased in cybrids carrying LHON mutations. A and B left panel: Detection of autophagic activity through immunoblot on LHON cybrids carrying m.11778G>A/MT-ND4 mutation (A) and m.3460G>A/MT-ND1 mutation (B). N = 3 independent experiments. **A, and B central panel**: Cells were transfected with a GFP-LC3-encoding plasmid and cultured in complete medium for 36 h. N = 20 visual fields per condition. **A and B right panel:** GFP-LC3 punctae count. Where indicated, the cells were starved (STARV.) for 30 min. **C**: Autophagic flux analysis using a Bafilomycin A1 treatment in complete medium for 2h. N = 3 independent experiments. * $p<0.05$

We have assessed autophagy in cybrids obtained from healthy controls (marked as CTRL), and LHON affected patients carrying both the m.11778G>A/MT-ND4 and m.3460G>A/MT-ND1 (Figure 13). We confirmed in LHON cybrids the previous results obtained in fibroblasts: LHON mutations lead to a significant increase in the autophagic activity (Figure 13A and 13B). Similar results were also obtained with cybrids carrying the m.14484T>C/MT-ND6 mutation (data not shown). Autophagic flux analysis indicates that

the process is unaffected and autophagosomes are adequately degraded (Figure 13C).

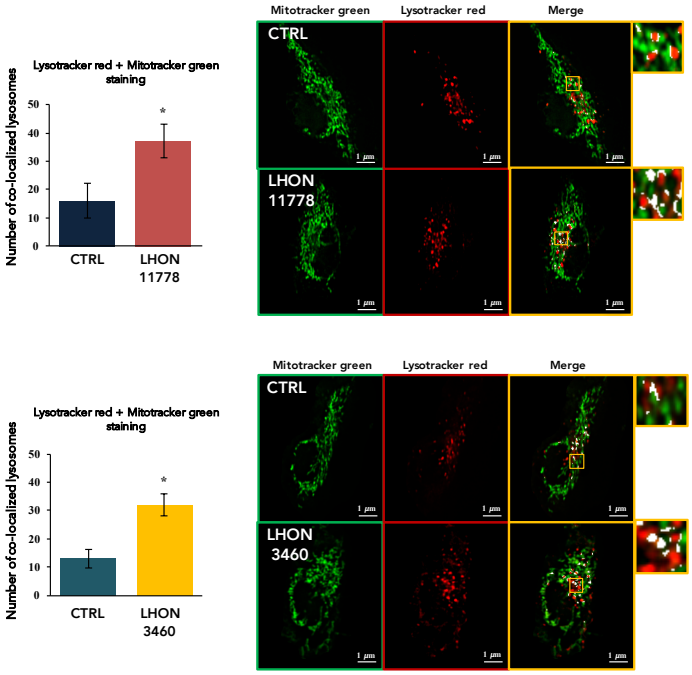

Figure 14 - LHON cybrids display an increased mitophagic activity. A and B: Confocal microscopy assessment of mitophagy in control and mutant fibroblasts harboring LHON mutations. Before experiments, control (CTRL) and mutated cells (LHON) were loaded with LysoTracker Red and MitoTracker Green to visualize lysosomes and mitochondria, respectively. The degree of the signal of lysosomes with mitochondria (merge) was calculated via cell live imaging microscopy by using a Nikon Swept Field confocal microscope equipped with a CFI Plan Apo VC60XH objective (numerical aperture N.A.= 1.4). Graphs represent the amount of colocalization between lysosomes (red signal) and mitochondria (green signal). The rate of colocalization of green and red signals was evaluated using the colocalization counter JACOP available in Fiji software. N = 20 visual fields per condition. Data are presented as means ± SEM. *$p < 0.05$.

Furthermore, also in cybrid cell model mitophagy activity results sustained in cells where the mtDNA have the typical LHON mutations (Figure 14).

As we described above, mitochondria play critical roles in cell health and survival thanks to their ability to produce energy through oxidative phosphorylation. However, mitochondria take part in cell death by regulating apoptosis and are also a primary source of Reactive Oxygen Species (ROS).

We then evaluated, also in this cell model, mitochondrial physiology parameters. Cybrids confirmed the trend of mitochondria carrying LHON mutations to produce and accumulate more ROS, to have an increased membrane potential and a more fragmented network (Figure 15).

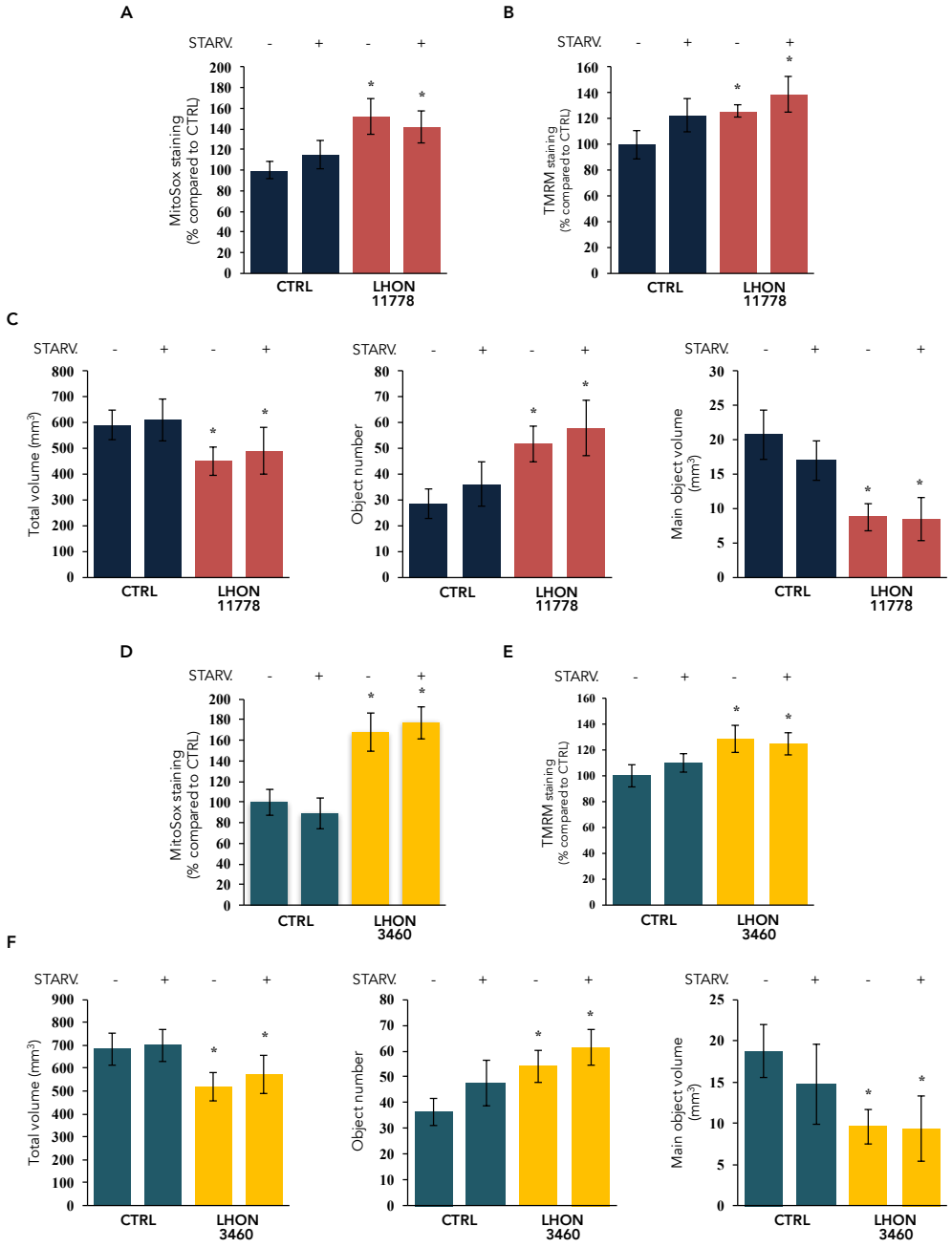

Figure 15 - Mitochondrial physiology parameters assessed in cybrids harboring LHON mutations. A and D: Measurements of mitochondrial ROS production in LHON cybrids carrying m.11778G>A/MT-ND4 (A) m.3460G>A/MT-ND1 (D) mutations by using MitoSOX Red probe. **B and E**: The mitochondrial transmembrane potential (Ψ_m) of control (CTRL), and LHON fibroblasts was detected by using the Ψ_m-sensitive probe TMRM. After imaging, the Ψ_m was depolarized by the mitochondrial uncoupler FCCP. When indicated, the cells were starved (STARV.) for 30 min before TMRM loading.
C and F: Cells were labeled with a red-fluorescent dye that stains mitochondria in live cells (MitoTracker Red), and the mitochondrial volume, number, and volume of single organelle was studied. Images acquired by confocal microscopy were deconvolved, 3D reconstructed and quantitatively analyzed. Where indicated, the cells were starved for 30 min. N = 15 visual fields per condition. Quantitative results (means ± SEM; $p < 0.01$) are depicted. *$p < 0.05$.

2.3.4 Generation of patient-derived iPSCs and differentiated neuronal cells

As reported above, LHON is primarily characterized by a progressive degeneration of retinal RGCs, the terminal retinal neurons forming optic nerve projecting to the brain. To confirm our findings in a cellular model closer to retinal neurons, we generated different clones of

transgene-free hiPSCs by reprogramming fibroblasts of one patient carrying the 3460G>A mutation and one control using Sendai virus-mediated expression of the four Yamanaka's factors (OCT3/4, SOX2, c-MYC and KLF4). To confirm stem cell pluripotency, we verified expression of specific markers by RT-PCR (NANOG, REX1, SOX2, OCT4) and immunofluorescence analysis (OCT4, NANOG, TRA1-60) (data not shown). We then obtained neuronal precursor (NPC) through embryoid body formation and then generated terminally differentiated neurons. When NPC reached a complete neuronal identity, expressing specific markers such as Beta-tubulin, Map2, and NeuN, we assessed autophagic activity and observed a higher concentration of LC3-II in LHON neurons as previously demonstrated in fibroblasts and cybrids. (Figure 16A)

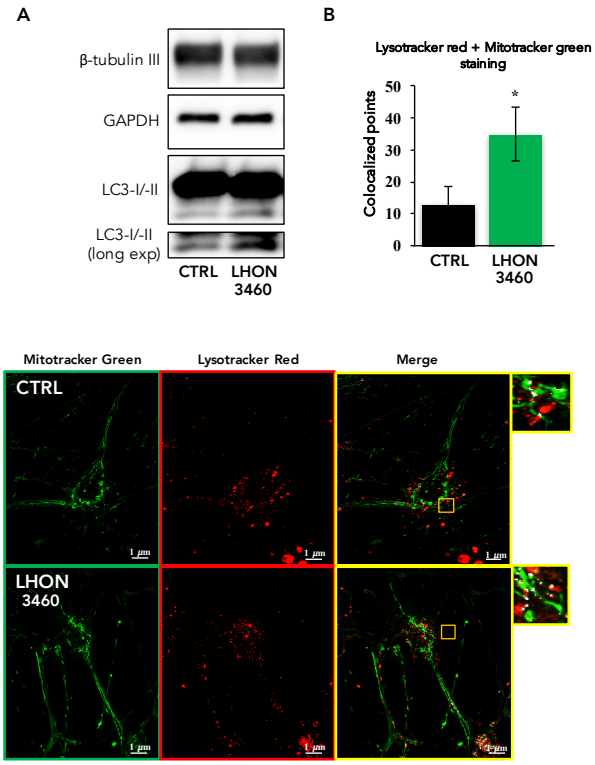

Figure 16 - Patient-derived iPSCs and differentiated neuronal cells confirm LHON-associated increased autophagic and mitophagic activity. A: Detection of autophagic activity through immunoblot on LHON iPSC derived neurons carrying m.3460G>A/MT-ND1 mutation. N = 3 independent experiments. **B:** Confocal microscopy assessment of mitophagic activity in control and LHON iPSC derived neurons. Bottom panel: representative images. N = 10 visual fields per condition. Quantitative results (means ± SEM; $p < 0.01$) are depicted. *$p < 0.05$.

iPSC-derived neurons also manifested the same tendency founded in fibroblasts and cybrids, highlighting a significant increased MitoTracker green/Lysotracker red colocalization rate and, consequently, an increased mitophagic activity. (Figure 16B)

2.3.5 Compensatory therapeutic approaches targeting autophagy, oxidative stress and mitochondrial biogenesis

As described above mitochondria can play a key role in the activation of the pathway of apoptosis and previous works correlate LHON to an increased sensitivity to apoptosis (*75*). To assess apoptotic levels on our cellular models, we performed immunoblot (using antibodies against the apoptotic markers poly (ADP-ribose) polymerase-1 (PARP-1) and Caspase 3) and cell viability assays (Figure 17). Cleavage of PARP-1, a major substrate of both Caspase 3 and Caspase 7, is a valuable marker of apoptosis. We highlighted a significant activation of the apoptotic pathway in LHON fibroblasts (Figure 17A and 17B), cybrids (Figure 17C and 17D) and iPSC-derived neurons (Figure 17E), confirming the increased sensitivity of LHON cells to undergo apoptosis.

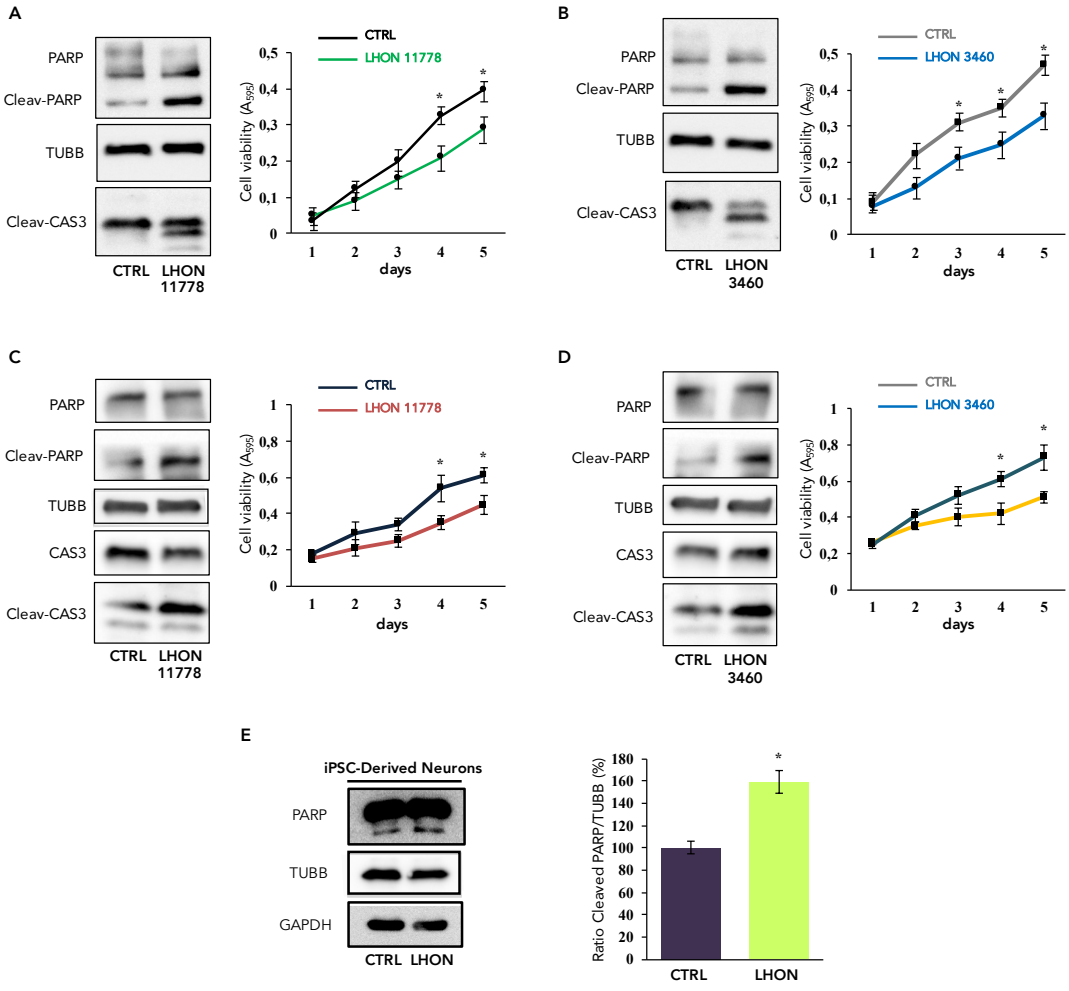

Figure 17 - LHON mutations give a higher predisposition to apoptotic death. A and B: Left side: Detection of apoptotic process in LHON fibroblasts by immunoblotting with antibodies against PARP-1 and Caspase 3 apoptotic markers. Right side: cell proliferation growth curves; cells were seeded at 35,000 per well in a 6-well plate (seeded on 6 plates per condition, one for each day). Every 24h a plate was fixed using 4% paraformaldehyde in PBS for 15 min. After 5 days, cells were stained with 0.1% crystal violet for 20 min. 1 ml 10% acetic acid was added to each well to extract the crystal violet from cells, and the absorbance at 595 nm was measured. **C and D:** Left side: Detection of apoptotic activity in LHON cybrids by immunoblotting

with antibodies against PARP-1 and Caspase 3 apoptotic markers. Right side: cell proliferation growth curves of LHON cybrids. **E:** Immunoblot with antibodies against the apoptotic marker PARP-1 to assess apoptotic activity on iPSC derived neurons and Cleaved Parp/TUBB ratio quantification (right side). N = 3 independent experiments. Quantitative results (means ± SEM; $p < 0.01$) are depicted. *$p < 0.05$.

All considered, our results indicate that LHON mutations activate the autophagic/mitophagic pathway and, finally, interfere with the normal apoptotic machinery. Thus, we hypothesized that modulating the excessive activity of autophagic/mitophagic pathway, we could modify the LHON pathogenic mechanism leading to RGCs degeneration and death; autophagy, in fact, can be finely pharmacologically adjusted through the targeting of the early or late stages of this process (*93*). To date, the most used inhibitor that targets autophagy early stage is 3-methyladenine (3-MA) (*93*); for late stage chloroquine (CQ) and clozapine (CZ) (*94*) are commonly wide used. 3-MA targets the class III phosphatidylinositol 3-kinase (PI3K class III), responsible for the autophagosomes assembly, whereas lysosomal lumen alkalizers (chloroquine and clozapine) are used to block autophagic progress by impairing lysosomes. As expected, treatment with autophagic inhibitors significantly reduced the autophagic process (Figure 18A and 18D). In addition to this, we founded an important reduction in the number of apoptotic markers cleaved PARP-1 and cleaved Caspase 3 and then an increased cell viability in treated LHON fibroblasts (Figure 18B and 18C) and cybrids (Figure 18E and 18F), consolidating the hypothesis that the autophagic pathway could play an essential role in the onset of the final phonotype of this neuropathy.

Our evidences indicate that, besides insufficient compensatory mitobiogenesis, the affected individuals present increased basal levels of autophagy and mitophagy. Thus, two parallel key pathways crucial for mitochondrial homeostasis are deregulated in LHON: mitobiogenesis and mitophagy. Considering our experimental evidences, we hypothesized that, more than in defective bioenergetics, the keystone could be located into the increased ROS production and accumulation. For this reason, in the last part of this work, we assessed autophagic levels after mitochondria biogenesis stimulation and after an antioxidant compound treatment, to reduce mROS levels.

Idebenone is a short-chain benzoquinone that acts as a potent antioxidant and lipid peroxidation inhibitor; therefore it protects cell membranes and mitochondria from oxidative damage (*95*).

Idebenone is the only disease-specific drug approved to treat visual impairment in patients with Leber's hereditary optic neuropathy. The mechanism of action of idebenone involves its ability to act as a mitochondrial electron carrier and, naturally, its antioxidant properties.

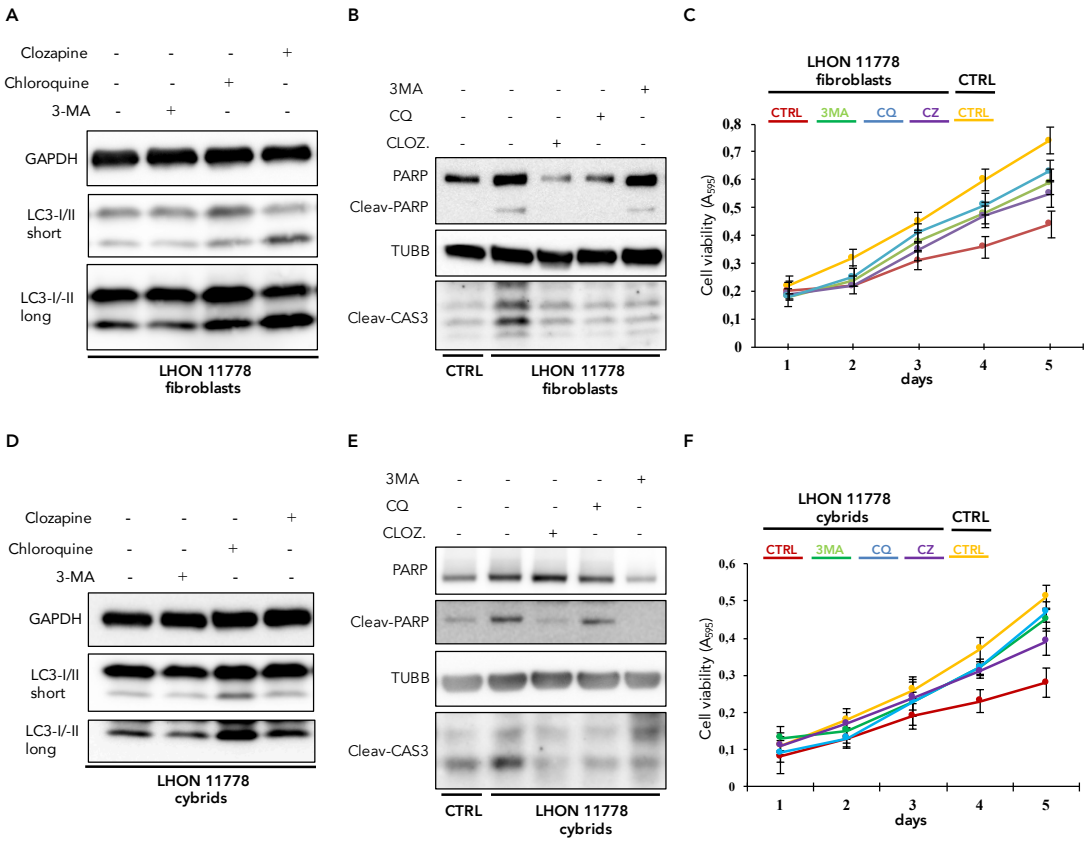

Figure 18 - Compensatory therapeutic approaches targeting autophagy reverts LHON cells predisposition to apoptotic death. A: Fibroblasts harboring LHON mutations were treated with different autophagic inhibitors [3-MA (inhibitor of autophagy at early steps), Chloroquine and Clozapine (inhibitors of autophagy at late steps)]. After 48h, detection of autophagic activity through immunoblot technique was performed on LHON fibroblasts, using antibodies against LC3 autophagic marker. **B and C:** Detection of apoptotic process activity on LHON fibroblasts treated with antiautophagic agents by immunoblotting with antibodies against PARP-1 and Caspase 3 apoptotic markers (B) and by cell proliferation growth curve assay (C). **D:** Detection of autophagic activity consequently antiautophagic treatments through immunoblot technique on LHON cybrids, using antibodies against LC3 autophagic marker. **E and F:** Detection of apoptotic process activity on LHON cybrids treated with antiautophagic agents by immunoblotting with antibodies against PARP-1 and Caspase 3 apoptotic markers (E) and by cell proliferation growth curve assay (F). N = 3 independent experiments. Quantitative results (means ± SEM; $p < 0.01$) are depicted. *$p < 0.05$.

After idebenone treatment in LHON mutated cells, we noticed a reduction of autophagic (Figure 19A) and apoptotic (Figure 19B) markers expression, mROS production and accumulation (Figure 19D), and a restored mitochondria network morphology (Figure 19E). It is interesting to note how, even in iPSC-derived neurons, idebenone performs an efficient antiautophagic activity (Figure 19C).

Similar results were obtained as a consequence of peroxisome proliferator-activated receptor gamma, coactivator 1 alpha (PGC-1α) overexpression, that is considered as the "master regulator" of mitochondrial biogenesis; PGC-1α acts improving the expression of nuclear genes encoding mitochondrial proteins (Figure 19F-I) (*96*).

This extended set of results link tightly mROS production, the major pathologic consequence of LHON mutations, with the autophagy/mitophagy pathway and mitobiogenesis as the key crossroad in the pathogenic mechanism of LHON, amenable to pharmacological corrective approaches from at least three different directions: correcting ROS production with antioxidants, inhibiting the autophagy/mitophagy pathway, increasing mitobiogenesis.

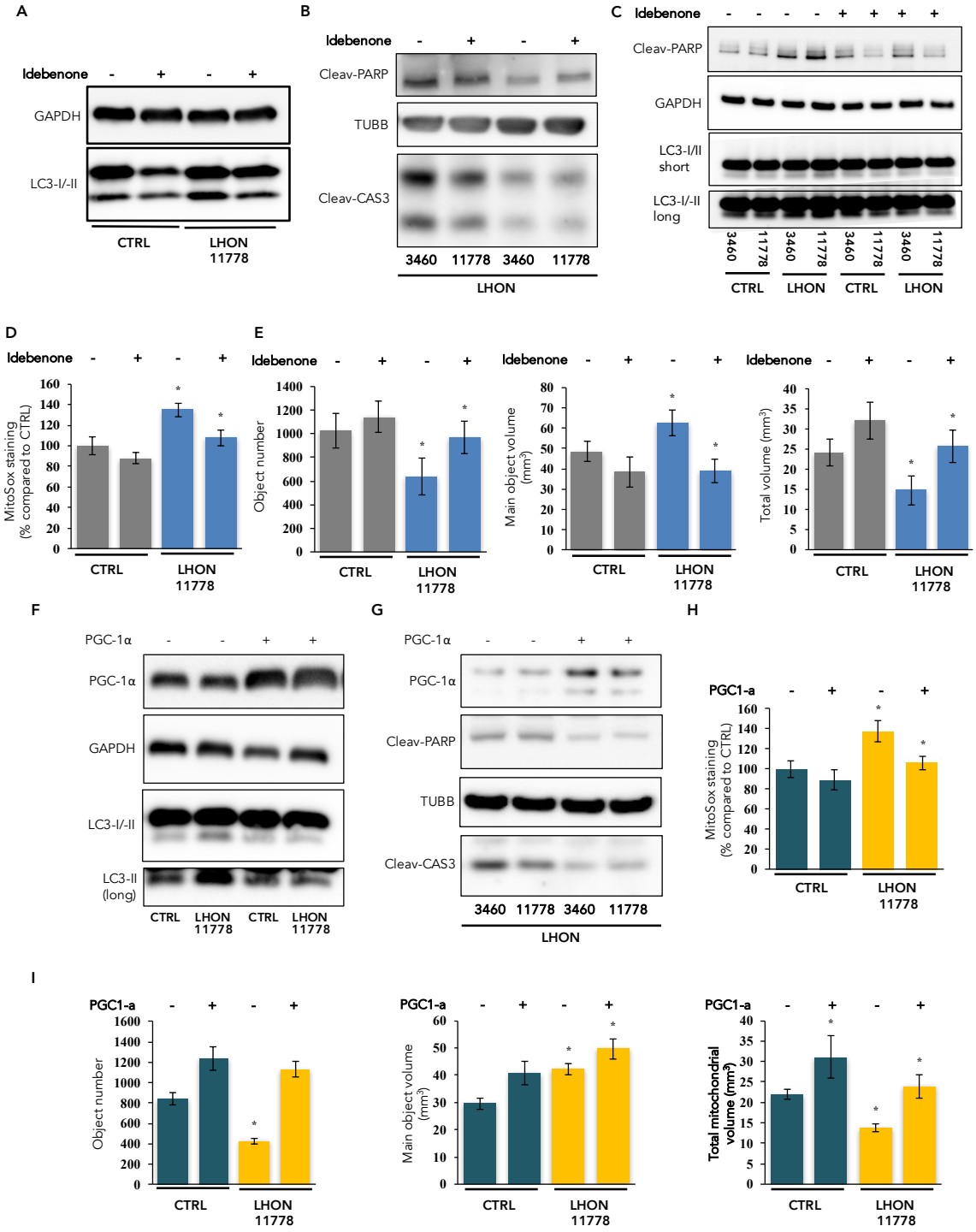

Figure 19 - Oxidative stress and mitochondrial biogenesis modulation contribute to decrease LHON cells autophagic activity and apoptotic death. After Idebenone treatment (10 μM for 3h), fibroblasts were harvested and immunoblotted for the autophagic marker LC3 (**A**) and apoptotic markers PARP-1 and Caspase 3 (**B**). In **C** autophagic and apoptotic assessment was made in iPSC derived neurons. **D:** Measurements of mitochondrial ROS production by using the MitoSOX Red probe. **E:** LHON fibroblasts, after Idebenone treatment, were labeled with a red-fluorescent dye that stains mitochondria in live cells (MitoTracker Red), and the mitochondrial volume, number, and volume of single organelle was studied. Images acquired by confocal microscopy were deconvolved, 3D reconstructed and quantitatively analyzed. Where indicated, the cells were starved for 30 min. **F and G:** Representative immunoblot in PGC1-alpha overexpressing cybrids. After 36 h, the cells were harvested and immunoblotted for the autophagic marker LC3 (F) and apoptotic markers PARP-1 and Caspase 3 (G). **H:** Measurement of mitochondrial ROS production in PGC1-alpha overexpressing cybrids by using the MitoSOX Red probe. **I:** mitochondrial volume, number and volume of the single organelle in PGC1-alpha overexpressing cybrids. N = 3 independent experiments. Quantitative results (means ± SEM; $p < 0.01$) are depicted. *$p < 0.05$.

2.4 DISCUSSION

Mitochondrial diseases were once thought of as rare disorders, in part due to failure to recognize the diagnosis because of the vast variability among phenotypes. They are increasingly recognized as a common cause of neurologic and visual dysfunction (*97*).

Leber's hereditary optic neuropathy (LHON) has been the first human disease to be associated with a maternally inherited missense mutation in mitochondrial DNA and is the most frequent mitochondrial disease (*67*).

The primary cell type that is lost in LHON is the retinal ganglion cell (RGC), which is highly susceptible to disrupted ATP production and oxidative stress.

The rapid loss of RGCs and their axons, with a subacute neurodegenerative process, leads to optic nerve atrophy in about one year, with severe loss of central vision, in most cases leaving the patient legally blind. Inheritance of LHON follows that of mitochondrial genetics, and it has a highly variable clinical phenotype, as other genetic and environmental factors also play a role (*98*).

Here we demonstrated that autophagic activity and the mitochondrial compartment-specific process (mitophagy) are expressed at high levels in LHON cellular models of increasing complexity, including skin-derived fibroblasts, cybrids, and iPSC-derived neurons.

Fibroblasts are obtained from healthy and LHON patients skin biopsy. Fibroblasts from patients that are mutation carriers but not become affected and don't manifest the LHON phenotype are named as "Carrier".

Cybrid (cytoplasmic hybrid) is a chimeric cell model that allows us to study the influence of mitochondrial DNA on cell function, without the contribution of the original patients' nuclear background. Cybrids are constructed by fusing enucleated cells harboring wild type or altered mtDNA of interest with ρ(0) cells in which the endogenous mtDNA has been depleted. Thus, cybrids are very useful in studying consequences of mtDNA alterations or other mitochondrial defects at the cellular level by excluding the influence of nuclear DNA mutations.

On the other hand, cybrid cells miss the phenotypic effect of the original nuclear background of the patient, can mutate over time or adapt to the mutant mtDNA genotype and are immortalized cells derived from cancer, distant from representing the LHON target tissue. The use of fibroblasts from LHON patients allows to overcome these issues and represents a more reliable cell model despite being more difficult to manage in culture. This difficulty is not present in cybrids; with this cellular model, we can incorporate human subject mitochondria and perpetuate its mtDNA-encoded components. The use of fibroblasts and

cybrids together allow us to observe effects which, if confirmed in both cellular models, can be exclusively attributed to LHON mutations in mitochondrial compartment.

To further corroborate our data in a cellular model more physiologically relevant for LHON disease, we generated iPSC-derived neurons in which we investigated some of the pathological phenotypes observed in fibroblasts and cybrids.

In this work, we tried to correlate the mitochondrial respiratory chain defect and apoptotic cell death, typical of Leber's neuropathy, to mROS production and accumulation and autophagic/mitophagic activity.

Autophagy is a bulk degradation process that occurs in the sequestration of proteins and organelles into double-membrane vesicles called autophagosomes and their subsequent degradation through the fusion of autophagosomes with lysosomes (*99, 100*). By selectively degrading damaged organelles or harmful protein aggregates, autophagy plays essential quality control functions within the cell, maintaining intracellular homeostasis (*101*).

Defective autophagy occurs in several pathological conditions, including cancers, neurodegenerative and cardiovascular diseases, and metabolic disorders (*102*). Nevertheless, the autophagic activity expressed at high levels can lead to cell death (*103*). Consequently, using a pharmacological approach to re-establish physiological levels of autophagy may be beneficial in treating certain diseases. Nevertheless, several clinical trials are currently based on the employment of agents acting on autophagy induction (*104*).

First of all, we assess autophagic activity on LHON fibroblasts, cybrids, and iPSC-derived neurons, highlighting an increased rate of the autophagy protein microtubule-associated protein 1 light chain 3 (LC3) and a consequent decrease of p62.

p62/SQSTM1 delivers ubiquitinated cargoes to the autophagosome, and p62 itself is incorporated into the autophagosome and subsequently degraded by autophagy (*105*). Cleaved and lipidated membrane-bound form of LC3 (LC3-II), which is localized to autophagosomes is the one used as a marker for this specific process. One typical trait of autophagy inhibition consists of increased amounts of the cytosolic non-lipidated form of LC3 (LC3-I) and total LC3 besides p62 accumulation (*106*).

The increase in LC3 levels in LHON fibroblasts, cybrids and iPSC-derived neurons, detected by Western Blot, corresponds to an increase in autophagosome' marker levels and, consequently, in autophagy activity. In fibroblasts and cybrids, the increased activity of this process was also assessed by fluorescence microscopy techniques using an LC3-GFP probe. In all these trials and in those that will follow, serum deprivation was used as positive control, causing lack of serum in the culture medium an intense autophagic activity.

Surprisingly, fibroblasts obtained from carrier patients display low basal levels of autophagy, comparable to controls; this contained autophagic activity in individuals carrying LHON' typical mitochondrial DNA mutations could be one of the discriminating features of LHON final phenotype.

To assess that autophagic flux is unaffected in these experimental conditions we evaluated the induction of autophagy in the presence of Bafilomycin A1 (Baf A1), an inhibitor of the late phase of autophagy, in control and LHON fibroblasts and cybrids.

Autophagosomes accumulation could, in fact, result from a defect in the process leading to their degradation, and not from a real increased autophagic activity.

Autophagic flux was equally preserved in control and LHON cells, indicating that the autophagic response is unaffected in our experimental conditions.

The compartment-specific process, named mitophagy, also results altered in LHON cells, but it is not significantly different from control fibroblasts in carriers.

We then decided to deepen mitochondrial physiology parameters, being the defect limited to this specific intracellular compartment.

We used two different techniques to evaluate the same parameter, that is the Oxygen Consumption Rate (OCR). Both through micro-oxygraphy method and through the use of the Clark electrode, we highlighted that LHON fibroblasts have a markedly decreased basal respiration compared to control cells; also fibroblasts from carrier patients display a bit lower basal respiration. To deepen this analysis, we then evaluated the activity of each single mitochondrial respiratory chain complex, finding that LHON fibroblasts are characterized by a decreased Complex I and Complex IV activity while fibroblasts from carrier patients display a defect restricted to Complex I.

The respiratory chain builds the electrochemical gradient across the inner mitochondrial membrane that sustains the mitochondrial membrane potential (Ψ_m). In LHON cells we found a significant increase in the mitochondrial membrane potential and an amplified production and accumulation of ROS. Even in this case, carrier fibroblasts behave as fibroblasts from control patients, supposing healthier mitochondria. Evaluating mitochondrial morphology is a suitable method to investigate mitochondria structure and state of health.

Cells were imaged in a confocal fluorescence microscope with the use of a mitochondria-localized probe and, after deconvolution and 3D reconstitution, we highlighted that LHON fibroblasts and cybrids displayed a prevalent fragmented network, compared to control cells. On the other hand, carrier fibroblasts exhibited a healthy mitochondrial network, not significantly different from that seen in control cells. These evidences indicate that Leber's

Neuropathy mutations, only in patients where LHON phenotype is evident, lead to sustained mitophagic activity, due to a dysfunctional and fragmented mitochondrial network.

Since LHON drives to RGCs cell death through the apoptotic process, we proceeded by assessing cell viability in all our cellular models. We found a higher PARP-1 and Caspase 3 amount, compared to control cells, and a lower predisposition to growth in colture of LHON fibroblasts, cybrids and iPSC-derived neurons.

To better define defective autophagy importance in this optic neuropathy context, we decided to try to revert the adverse viability effects we highlighted through the use of anti-autophagic agents. As a result, the mortality rate and cell viability have been significantly improved by the use of 3-MA, CQ and CZ, three of the most used anti-autophagic agents, acting in different stages of this degradative process. Of great importance is also the fact that two of these agents (CQ and CZ) are commonly used in various therapies and can be a viable option for future clinical trials. So, autophagy enhancement seems to be a crucial event for the promotion of lower cellular viability and apoptosis; in fact, only affected individuals who are characterized by a LHON phenotype display increased basal levels of autophagy and mitophagy. Mitobiogenesis and mitophagy are actually two crucial pathways for the deregulated mitochondrial homeostasis in LHON.

Considering our experimental evidences, we hypothesized that, more than in defective bioenergetics, the keystone could be located into the increased ROS production and accumulation.

Through the use of a benzoquinone that acts as a potent antioxidant, named Idebenone, we try to protect cell membranes and mitochondria from oxidative damage. Moreover, Idebenone at the moment is the only disease-specific drug approved for LHON treatment. A huge reduction of autophagy and apoptotic activity was observed following the use of Idebenone, not only in LHON fibroblasts and cybrids, but also and especially in iPSC-derived neurons. A further confirmation was obtained through the use of one of the most known master regulator of mitochondrial biogenesis that improve the expression of nuclear genes encoding mitochondrial proteins: PGC-1α.

The stimulation of mitochondrial biogenesis by overexpressing PGC-1α expression and, consequently, activating the PGC-1α pathway has been demonstrated to reduce ROS production. (*107*) Also PGC-1α overexpression, as well as Idebenone treatment, has led to a decreased apoptotic and autophagic activity and restored mitochondrial network morphology and integrity.

The results of this thesis work, globally clarify the alteration of the mitochondrial homeostasis and function determined by the major pathogenic mutations associated with LHON.

In conclusion our study suggests, for the first time, that autophagy and mitophagy processes could play an important role in the pathogenesis and the manifestation of the LHON phenotype.

Taken together our results, as well as assigning a key role to the auto/mitophagic process in the pathogenic mechanisms leading to LHON, proposes two different strategies to block the progressive optic nerve degeneration. Besides the use of Idebenone in this particular neuropathy treatment, it might be useful to act by stimulating mitochondrial biogenesis and with auto/mitophagic process inhibitors. Further studies are needed in order to get a valid therapy for this optic neuropathy, which represent the most frequent mitochondrial disease.

2.5 MATERIALS AND METHODS

2.5.1 Fibroblast and cybrids cell lines

Fibroblast cell lines were established from skin biopsies taken from five controls, seven affected (three m.11778G>A and two m.3460G>A) and one unaffected mutation carriers (m.11778G>A). Cells were grown in DMEM medium (EuroClone, Milano, Italy) containing 25 mM glucose and supplemented with 10% fetal bovine serum, 2 mM l-glutamine, 100 U/ml penicillin and 100 μg/ml streptomycin, maintained at 37 °C in a humidified atmosphere with 5% CO2. The functional experiments were carried out on sub-confluent cell cultures obtained from a comparable number of culture passages (10–20).

Cybrid cell lines were constructed using enucleated fibroblasts from two controls and six LHON probands as mitochondria donors and the osteosarcoma (143B.TK−)-derived 206 cell line as acceptor rho0 cell line. Both definition of the mtDNA haplogroup and identification of the LHON pathogenic mutations were performed by PCR/restriction fragment length polymorphism method. Parental and cybrid cell lines were grown in DMEM medium supplemented with 10% fetal calf serum, 2 mM L-glutamine, 100 units/ml penicillin, 100 μg/ml streptomycin, and 0.1 mg/ml bromodeoxyuridine. For the experiments, cells were seeded 4×10^5 cells/cm^2 and incubated in DMEM containing 25 mM glucose and supplemented with 10% fetal bovine serum, 2 mM l-glutamine, 100 U/ml penicillin and 100 μg/ml streptomycin at 37 °C in an incubator with a humidified atmosphere of 5% CO_2.

2.5.2 iPSC Generation and Characterization

Transgene-free induced Pluripotent Stem Cells were generated, from control and patient's fibroblasts, by CytoTune-iPS 2.0 Sendai Reprogramming Kit, introducing the four transcription factors proposed by Yamanaka, OCT4, SOX2, KLF4 and c-MYC. Characterization was performed according to (*108*).

2.5.3 Neural Precursor Cells Generation and Characterization

Starting by iPSC cultures, Neural Precursor Cells were obtained by multiple steps. Embryoid Bodies suspensions were cultured for 5 days and then plated on Matrigel-coated plates to generate neuroectodermal rosettes structures. After 5-7 days, rosettes were picked and plated on Polyornithine/Laminin to generate and maintain NPC cultures (*109*). NPC were characterized, after passage 3, by RT-PCR and immunofluorescence, looking for specific neuroectodermal markers like SOX1, PAX6 and NESTIN (*109*).

2.5.4 Neurons Generation and Characterization

Neural Precursor Cells were plated on glass support in Polyornithine/Laminin-coated plates. Next day Neuronal Differentiation Medium (DMEM/F-12, 1X N2 Supplement, 1X B27 Supplement, 30ng/ml BDNF, 30ng/ml GDNF, 1uM DAPT, 1X Penicillin/Streptomycin, 1X Glutamine and 1X Non-Essential Aminoacids) was added to the cells and then changed every other day. After 30 days, neurons can be characterized and analysed. Characterization was performed by immunofluorescence to verify the specific expression of typical neuronal markers like NEUN (Millipore), MAP2 (Cell Signaling) and βIII-TUBULIN (GenScript). The following dilutions were used: anti-NEUN 1:1000; anti-MAP2 1:200; anti-betaIII TUBULIN 1:500.

2.5.5 Immunoblotting

For immunoblotting cells were scraped into ice-cold phosphate –buffered saline and lysed in a modified 10mM Tris buffer pH 7.4 containing 150mM NaCl, 1% Triton X-100, 10% glycerol, 10mM EDTA and protease inhibitor cocktail. After 30 minutes of incubation on ice, the lysates were cleared via centrifugation at 12,000g at 4°C for 10 minutes. Protein concentration were determined by the Bio-Rad procedure. Protein extracts, 20 μg, were separated on 4-12% and 4-20% Bis-Tris acrylamide (Life technologies, NP0323 and EC6026) and electron-transferred to PVDF or Nitrocellulose membrane according to standard procedures. Unspecific binding sites were saturated by incubating membranes with TBS- Tween 20 (0.05%) supplemented with 5% non-fat powdered milk for 1h. Next, the membranes were incubated over-night with primary antibodies and the revelation was assessed by the employment of appropriate HRP-labeled secondary antibodies [SantaCruz, sc-2004 (goat anti-rabbit) and sc-2005 (goat anti-mouse)] plus a chemiluminescent substrate (Thermo Scientific, 34080).

2.5.6 Fluorescence microscopy and quantitative analysis of GFP-LC3 dots

Fibroblast and cybrid cells were cultured in a 24-mm glass coverslips and transfected with a standard calcium-phosphate procedure at 50% confluence with 6μg of plasmid DNA (GFP-LC3). Cells were cultured in a 24mm glass coverslips and transfected at 50% confluence. After 36h, images were taken on a Nikon LiveScan Swept Field Confocal Microscope (SFC) Eclipse Ti equipped of NIS-Elements microscope imaging software. For each condition, the number of GFP-LC3 dots was counted in at least 25 independent visual fields.

2.5.7 Mitophagy evaluation

Mitophagy experiments were performed in fibroblasts, cybrids and neurons. Cells were incubated with MitoTracker Green FM (final concentration: 1 μM) (Termo Fisher Scientific) for 30 minutes at 37°C and then extensively washed with PBS. LysoTracker Red DND-99 (Final concentration: 1 μM) (Termo Fisher Scientific) was then added and cells were immediately observed on a Nikon LiveScan Swept Field Confocal Microscope (SFC) Eclipse Ti equipped of NIS-Elements microscope imaging software. The rate of colocalization of green and red signals was evaluated using the colocalization counter JACOP available in Fiji software. For each condition, the colocalization of these two signals was also determined by manual counting of fluorescent puncta.

2.5.8 Quantitative analysis of the Autophagic-Flux

LHON fibroblasts cultured on 24-mm glass coverslips were transfected with a standard calcium-phosphate procedure with 6 μg of plasmid DNA (mCherry-eGFP-LC3). After 36h of expression, cells were imaged on a Nikon LiveScan Swept Field Confocal Microscope (SFC) Eclipse Ti with a 60x magnification and equipped of NIS-Elements microscope imaging software. Obtained puncta image were merge to compare the RFP signals with GFP signals using ImageJ software. For each condition, the colocalization of these two signals was determined by manual counting of fluorescent puncta in at least 20 independent visual fields.

2.5.9 Autophagy induction and inhibition

The autophagic process in vitro was triggered through serum deprivation (EBSS, 30 min). The pharmacological inhibition of autophagic machinery was performed by treating cells with 2.5 mM 3-MA (16 h), 5 μM CZ (16 h) or 5 μM CQ (16 h) in DMEM supplemented with 10% FBS. After treatment, the cells were fixed or lysed to detect the amount of autophagosome vesicles by fluorescence microscopy by immunoblot analysis (using LC3 antibody).

2.5.10 Microoxygraphy Experiments

The day before analysis, cells were plated at a density of 20000 cells per well in a 96-well multiwell plate and incubated over night at 37°C with 5% CO2. After 24 hours, medium was changed with a specific one containing 25mM glucose to perform analysis. Drugs added to cells during experiment were, in chronological order, Oligomycin 1 μM and FCCP

(Carbonyl cyanide 4-(trifluoromethoxy)phenylhydrazone) 2,1 μM. Measurements were done with Seahorse Bioscience XF96 and normalized on cell counts, calculated with CyQuant Direct Cell Proliferation Assay Kit. Statistical analysis was performed on three independent experiments by Student's t test.

2.5.11 Blue-native PAGE

Cells were grown on 10 cm plates in a high glucose medium DMEM (Lonza) containing 25 mM glucose and supplemented with 10% fetal bovine serum, 2 mM l-glutamine, 100 U/ml penicillin and 100 μg/ml streptomycin, maintained at 37 °C in a humidified atmosphere with 5% CO_2. Cell pellets were collected by trypsinization and lysed with the use of RIPA buffer supllemented with proteases and phosphatases inhibitors cocktails (Sigma Aldrich). After, protein concentration was measured using Bradford' method (BioRad) and the 1:5 (v:v) Laemmli sample buffer was added. 30 μg of sample was separated by SDS-PAGE and transferred onto PVDF membrane followed by 1 hour blocking in a 1:1 Li-COR Blocking Buffer. Next, membrane was incubated with primary antibodies against OXPHOS (abcam), TOM20 (Santa Cruz), HSP60 (Abcam), VDAC(Abcam) and Actin (Abcam) in a 1:1 Li-Cor blocking buffer (TBS-Tween 0,1%). Afterwards membrane was washed 3 times using TBS-Tween 0,1% buffer and incubated with fluorescent secondary antibodies 1:1 (Li-Cor) blocking buffer (TBS-Tween 0,1% and 5% BSA). Detection was performed with the Odyssey infrared Imaging System (Li-Cor Biosciences). Signal intensity was analyzed in Image™ Studio Lite (Li-Cor Biosciences).

Cells pellets were suspended in 50 mM Bis-Tris buffer supplemented with in 1 M aminocaproic acid (pH 7.0). Upon protein content quantification with the use of Protein Assay Kit (Bio-Rad), n-dodecylmaltoside was added (1% - final concentration), samples were incubated on ice for 30 min, and then centrifuged at 14000g for 20 min to remove insolubilized material. Thereafter, native lysates were combined with 5% Serva Blue G and 50 μg of protein was loaded and separated on a freshly prepared 5-12% polyacrylamide native gel. As an internal standard, 25 μg of protein from mouse liver mitochondria were used. At the end of the run in-gel activity assay has been performed.

2.5.12 Measurement of the oxygen consumption in intact and permeabilized human fibroblasts

The mitochondrial oxygen consumption rate (OCR) in human fibroblasts was measured with a Clark electrode (5300A biological oxygen monitor; YSI, Rye Brook, NY, USA). All measurements were performed at 25°C. Cells were detached with trypsin, sedimented by

centrifugation and suspended in 1 ml of measurement medium containing: 225 mM mannitol, 75 mM sucrose, 10 mM KCl, 0.5 mM EGTA, 1 mM MgCl2, 50 mM Tris-HCl (pH 7.4) and 5 mM pyruvate, 5 mM malate and 5 mM glutamate (used as respiratory substrates. The cell suspension was transferred to a measurement chamber and the following parameters were measured:

a) basal respiration in intact cels (in the presence of 5mM pyruvate),

b) cels were permeabilized by the addition of digitonin and recorded respiration was related to the electron flow along the Complexes I, III and IV with the use of glutamate and malate as substrates.

c) Rotenone was added to inhibit respiration supported from complex I substrates.

d) 5 mM succinate (substrate for complex II) was added and recorded respiration was related to the electron flow along complexes II, III and IV.

e) Antimicyn A (inhibitor of complex III) was added to inhibit respiration supported from complex II substrates.

f) TMPD and ascorbate were added to the measurement chamber and recorded respiration was related to the electron flow along complex IV.

g) Azide was added to inhibit complex IV related oxygen consumption.

The protein content in the chamber was measured with Bradford assay. The obtained results of oxygen consumption were normalized to the protein content in the cell suspension used in the measurement.

2.5.13 mROS measurements

Total release of ROS from mitochondria was estimated fluorimetrically by oxidation of MitoSOX Red probe and Tali™ Image-Based Cytometer. Fluorescence was measured using 510 ± 10 nm excitation and 595 ± 35 nm emission wavelengths for MitoSOX and DHE while 513 ± 10 nm excitation and 530 ± 25 nm emission.

2.5.14 Measurements of mitochondrial Ψ_m

Mitochondrial Ψ_m was measured by loading cells with 20nM tetramethyl rhodamine methyl ester (TMRM; Life Technologies, T-668) for 30 minutes at 37°C. Images were taken on an inverted microscope (Nikon LiveScan Swept Field Confocal Microscope (SFC) Eclipse Ti equipped of NIS-Elements microscope imaging software). TMRM excitation was performed at 560nm and emission was collected through a 590–650nm band-pass filter. Images were taken every 5s with a fixed 20ms exposure time. FCCP (carbonyl cyanide p-trifluoromethoxyphenylhydrazone, 10 μM), an uncoupler of oxidative phosphorylation, was

added after 12 acquisitions to completely collapse the electrical gradient established by the respiratory chain.

2.5.15 Mitochondrial morphology analysis

The cells were seeded before transfection onto 24-mm glass coverslips, allowed to grow to 50% confluence and then labelled with a MitoTracker Red fluorescent probe (10 μM) (Thermo Fisher). At 24 hours after labelling, cells were imaged with a laser scanning confocal Zeiss LSM 510, illuminating at 543 nm. Z stack of 51 planes were obtained with an objective Plan-Apo 63x/1.4 Oil Ph3 with a voxel size of 105 x 105 x 200 nm (X x Y x Z). To obtain the best object reality, images were next deconvolved using the open source software Fiji (http://fiji.sc/wiki/index.php/Fiji), and especially through the 3D iterative deconvolution plugin (http://www.optinav.com/Iterative- Deconvolve-3D.htm). A theoretical PSF were build using the "PSF generator" plugin available at http://bigwww.epfl.ch/algorithms/psfgenerator/.

Once reconstructed a mitochondrial and endoplasmic reticulum mask were manually chosen to obtain a binarized image of overlapping areas. The resulting areas were described in number and volume, using the 3D object counter, available in Fiji.

2.15.16 Cell proliferation and viability assay

Cells were seeded at 15,000 per well in a 6-well plate. Cells were seeded on 5 plates; one plate for each day. Every 24 hours after seeding, washed 1x with PBS and fixed in 4% paraformaldehyde in PBS for 15 min. Cells were stained with 0.1% crystal violet for 20 min. and then washed 3x with water. 1 ml 10% acetic acid to each well was added and incubate 20 min with shaking (extraction). Absorbance was measured at 590 nm.

3. IMPLICATIONS OF THE MITOCHONDRIAL UNIPORTER PORE FORMING SUBUNIT MCUb IN CELL CYCLE AND CANCER PROGRESSION.

3.1 ABSTRACT

The regulation of cell cycle progression is a complex and finely controlled process that involves proteases action, kinases cascades, production of second messengers and a large number of other activities. In recent years, a great amount of Ca^{2+} binding proteins have been proposed to mediate the effect of Ca^{2+} on the cycle. Moreover, recently increasing evidences interestingly suggest that changes in the Ca^{2+} intracellular concentration could play an essential role, especially in transitions between cell cycle phases. In this work, we decided to evaluate the role of mitochondria in cell cycle progression, and to analyze the mitochondrial Ca^{2+} variations that occur between cell cycle transitions. We observed a marked change in the composition of MCU complex, the mitochondrial Ca^{2+} uniporter, which is responsible for the uptake of Ca^{2+} cations into mitochondrial matrix. By modifying the expression of the dominant negative isoform MCUb, we observed proportional changes in mitochondrial Ca^{2+} uptake, mROS production and accumulation, cell viability, migration potential and cell cycle progression rate. Ca^{2+} transients have been observed to occur at the awakening from quiescence, at the G1/S transition, and especially in mitosis, the phase in which MCUb expression is at its maximum. Besides assigning a potential oncogenic connotation to the MCUb subunit, this thesis work places for the first time the mitochondria at the center of a $[Ca^{2+}]_c$ buffering action that allows the correct progression through the cell cycle.

3.2 INTRODUCTION

Cell division is an essential process for living organisms, and it allows growth, reproduction, and development of the organism. The regulation of this process represents the basis to maintain genetic integrity, which is essential to cell survival and proliferation. At this time, alterations to proteins involved in cell cycle regulation are of remarkable interest, because they are directly involved in tumor development. Therefore, understanding all the mechanisms that regulate cell proliferation and growth becomes crucial.

The cell cycle itself consists of an ordered set of events, ultimately resulting in cell growth and division to produce daughter cells. In mammals, cell cycle consists of two main phases: interphase (that occupies most of the time of cell division) and mitosis. Interphase, in turn, can be divided into three stages known as G1, S and G2. Briefly:

- **G1 phase**: this period, also known as gap-phase 1, prepares the cell for the genetic material division with size increase and synthesis of numerous proteins and organelles such as mitochondria and ribosomes. At a certain point - the restriction point - the cell is committed to division and moves into the S phase.
- **S phase**: is defined as the stage in which DNA synthesis occurs. Each chromosome now consists of two sister chromatids.
- **G2 phase**: is the second gap-phase, which accompanies the cell up to mitotic division. It is characterized by a high metabolic activity and the synthesis of the mitotic spindle;

The term G0 is used to describe cells that have exited the cell cycle and become quiescent. G0 phase is the phase in which cells do not divide for many reasons: they can be already differentiated, or it may be a waiting phase which will lead to a delayed division. Most of the lymphocytes in human blood are in G0. However, with proper stimulation, such as encountering the appropriate antigen, they can be stimulated to reenter the cell cycle at G1 phase.

The **mitotic phase** includes the most significant events of cell division and can be divided into two phases: mitosis and cytokinesis. During interphase, chromosomes are not visible individually, but they are condensed in the form of chromatin, an association of DNA and protein present in the nucleus; in the step of the division the chromatin coils in individual chromosomes that will then be divided.

The mechanism of division involves the diploid somatic cells (2n): they consist of two pairs of homologous chromosomes that carry both genes that control the same characteristics.

A class of proteins directly involved in cell cycle progression is cyclins, discovered in 1983 by Tim Hunt and his colleagues (*110*). Cyclins levels vary drastically through the phases of the cell cycle as a result of transcriptional changes and degradation mediated by the proteasome.

There are eight cyclins involved in cell cycle progression: cyclin A1 and A2, B1-B2-B3, C, D1-D2-D3, E1-E2, F, G1-G2, H. All these show a 150 aminoacid residues region called cyclin box; this domain consisting of five helices (*111*) is responsible for the binding of the N-terminal part of specific Cdk (*112*).

The fluctuation of the expression levels of these proteins has been demonstrated by the fact that cyclins A and B are accumulated at the beginning of S phase and in the late G2 phase respectively, while in G1 phase cyclin D1 levels increase and remain high until the mitosis. While cyclins A and B contain a "destruction box", cyclins D and E contain a PEST sequence, or a segment of amino acid residues rich in proline (P), glutamic acid (E), serine (S) and threonine (T). These sequences are required for efficient proteolysis ubiquitization-mediated at the end of each phase of the cell cycle (*113*). Cyclin H forms complexes with Cdk7 to constitute an enzyme known as CAK (kinase activated by Cdk); CAK is involved in the activation of CDC2 and Cdk2, respectively, by phosphorylation of residues Thr 160 and Thr 161. Together with the Cdk 7 and MAT-1 (protein menage-a - trois- 1), cyclin H form a tertiary complex which modulates transcription by acting on the activity of RNA polymerase II (RNA pol II). Cyclin T does not seem to be directly involved in cell cycle regulation, but his bond with the Cdk9 makes active in various processes such as transcription, signal transduction and differentiation (*112*).

Cyclin F has some similarities with cyclins A and B; it seems to interact with the cyclin B and Cdk1 to form a trimeric complex. Cyclins G (G1-G2) are the p53 target, and they appear to be involved in the arrest of the cycle in G2/M phases after DNA damage.

Cyclins activate specific Cdks, a family of serine/threonine protein kinases (*112*), and the activation occurs in specific phases of the cell cycle (*113*).

The formation of specific complexes cyclin/Cdk ensures the progression of the cell cycle; cyclins have a high expression at particular times and, then, they are degraded, guaranteeing the periodic activation of the Cdk, which on the contrary have constant expression levels.

So, the cell cycle is one of the most regulated mechanisms of the cell.

It has long been known the role of Ca^{2+} as a second messenger which can be influenced by a large number of effector proteins and as explained previously mitochondrial Ca^{2+} homeostasis is crucial for the destiny of the cell.

Therefore, it was interesting to investigate a possible link between mitochondrial Ca^{2+} homeostasis and cell cycle. On the other hand, mitochondrial Ca^{2+} uptake by MCU complex has a great importance for the regulation of cell life and energy production. It will be particularly interesting to investigate if MCU complex could be a pivotal regulator of cell cycle.

3.3 RESULTS

3.3.1 Synchronized T98G cells display significantly lower mitochondrial calcium concentration in mitosis, compared to the other cell cycle phases.

The starting idea of this work comes from some evidence that correlates precise and recurring Ca^{2+} fluctuations to cell cycle progression. Spontaneous Ca^{2+} oscillations at the G1/S phase transition have been described in synchronized immortalized cell lines and, these swings accompany DNA replication (*114*). As described in the introductory part of this thesis work, mitochondria play an essential role in calcium homeostasis. For this reason, we decided to evaluate mitochondrial calcium concentration ($[Ca^{2+}]_m$) during cell cycle progression.

To correctly discriminate different phases of the cell cycle we had to fine-tune a cellular synchronization protocol. We found in T98G cell line a good candidate for obtaining a healthy synchronized cell population. In fact, most of the commercial cell lines require the use of pharmacological agents to achieve a well synchronized cell population.

T98G cells derive from a human glioblastoma tumor, and the synchronization procedure is based on Serum Starvation technique (0.1% FBS), which allows cells to enter in the G0 stationary phase. Then, after serum addition (final concentration: 10% of the medium) leads the cells to re-enter in the cell cycle. Cells were harvested at intervals of two hours for 40h. The correct synchronization in the desired phase was assessed by western blot, using specific markers of the cell cycle. In particular (as described previously), Cyclins A, B and F are markers of S-G2 phase, phosphohistone H3 (pHH3) is a tag of M phase, and Skp1 is used as protein loading control. After 4h from release cells are in G1 phase, in G1/S after 12h, S in 24h, G2 in 30h and mitosis after 36h. As can be observed in Figure 20A, we obtained a good synchronization protocol and after 36h (from serum addiction) most of the cells are in mitosis. Asynchronous cells were used as a control, and each cellular homogenate was taken together with the corresponding homogenate in synchronized cells. To have further confirmation, we perform a cell phase analysis using a specific reagent from Thermo Fisher's Tali cell cycle kit. This single-addition reagent is composed of propidium iodide (PI), RNase A, and Triton X-100 and provides a convenient and accurate determination of the percentage of cells in each phase of the cell cycle, using the Tali Image-Based Cytometer. Most of the cellular population results synchronized by analyzing the data generated by the instrument, with the 74% of the cells in G1 phase after 4 hours from serum addiction, and the 57% in G2/M after 30 hours. (Figure 20B)

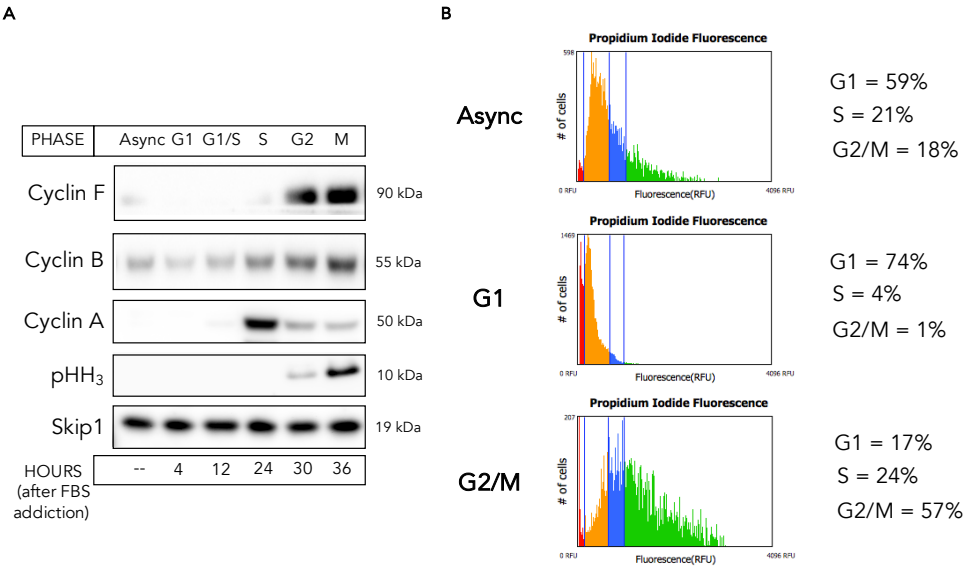

Figure 20 - T98G cells synchronization. **A:** Western Blot analysis from T98G cells synchronization. Cyclin A was used as a marker of S-G2 phases, Cyclin B was used as a marker of G2-M phases, Cyclin F was used as a late G2/M marker, pHH3 is used as a marker of M phase, Skp1 was used as protein loading control. **B:** Cell cycle analysis in asynchronized, G1 and G2/M T98G cells using the Tali® Image-Based Cytometer. Percentages are referred to the number of cells in each phase of cell cycle. N = 3 indipendent experiments.

At this point, having obtained a suitable protocol for T98G cell line synchronization, we believed it could be interesting to investigate a possible link between mitochondrial Ca^{2+} homeostasis and cell cycle.

Indeed, Ca^{2+} is a second messenger able to control a considerable number of cellular processes, such as muscle contraction, gene transcription, learning, memory, cell proliferation, fertilization, secretion and development (*115*).

The intracellular Ca^{2+} concentration influences signals that control cell cycle progression, although such substantial evidence, still little attention is focused on the role of Ca^{2+} in the cell cycle (*116*).

Ca^{2+} regulates cell cycle progression and arrest and apoptosis in a wide variety of cells and developmental stages (especially in meiotic mammalian oocytes) (*117*). Cell cycle progression requires Ca^{2+} influx from both intra- and extracellular sources. A moderate increase in $[Ca^{2+}]_c$ and the levels of reactive oxygen species (ROS) is essential for cell cycle progression.

ROS production is closely related to the Ca^{2+} signaling network; furthermore, ROS are involved in cell cycle regulation via ubiquitination and phosphorylation and act on trans-activating growth factor receptors (*118*). A moderate increase in $[Ca^{2+}]_c$ above the physiological threshold may lead to metaphase-II cell cycle arrest in oocytes. On the other

hand, a massive increase in $[Ca^{2+}]_c$ generates oxidative stress, which induces Fas ligand- and mitochondria-mediated apoptosis (*119*).

Disorders of cell cycle control may also be critical for the prevention and development of cancer, and these disorders may result from differences in $[Ca^{2+}]$ caused by various mechanisms (*120*). Constitutive IP3R3-mediated Ca^{2+} transfer to mitochondria through MAMs is essential for cancer cell viability. If this signal is non-functional or perturbed, normal healthy cells restrict their entry into the cell cycle; in contrast cancer cells bypass the Ca^{2+} checkpoints and undergo necrotic collapse during cytokinesis (*121*).

A lot of proteins are modulated by the Ca^{2+} signal, due to this ion versatility and ability to diffuse. Some examples are represented by CaMK (activated by CaM), which regulates the G1/S transition and the exit from mitosis (*122*) and calcineurin that plays a role in mediating the entry into G1 phase and the continuation in the S phase (*123*). During the resting state, Ca^{2+} undergoes fluctuations that alter its concentration, to carry out its functions. Mitochondrial and ER networks are fundamental for the maintenance of cellular homeostasis and the determination of cell fate under stress conditions (*124*). Ordinarily, Ca^{2+} ions are stored in these organelles and only in response to stimulation they are released to be transferred into the cytosol. The communication between the two organelles takes place via a zone of close contact between ER and mitochondria, called MAM (*125*).

For $[Ca^{2+}]$ assessments in intracellular compartments, we transfected T98G cells with cDNA coding for mitochondrial and cytosolic aequorin. Upon binding of Ca^{2+} ions, the coelenterazine (aequorin' hydrophobic prosthetic group) is oxidized to coelenteramide, with a concomitant release of carbon dioxide and emission of light; this is an irreversible reaction where one photon is emitted. The possibility of using aequorin as a calcium indicator is based on the existence of a well-characterized relationship between the rate of photon emission and the free Ca^{2+} concentration. For these $[Ca^{2+}]$ assessments, in addition to the classical cytoplasmic-locating form, we used a particular type of recombinant aequorin, that can be expressed in mitochondria by including specific targeting sequencing in the engineered cDNA. These measurements were conducted in asynchronous and synchronized cells. Cells are stimulated with 100 μM Instamine to enable Ca^{2+} mobilization. This agonist selectively binds the membrane receptor coupled to a trimeric G protein: in particular, the α subunit can activate phospholipase C which hydrolyzes phosphatidylinositol-4,5-bisphosphate (PIP2) generating diacylglycerol (DAG) and inositol 1,4,5-trisphosphate (IP3). The IP3 binding to its receptor on the ER causes an increase in $[Ca^{2+}]$ in the cytoplasm and mitochondrial matrix.

Thus, $[Ca^{2+}]_m$ measured after agonist stimulation is 3.684 ± 0.176 µM in asynchronous cells, 4.867 ± 0.472 µM in G1 phase, 3.980 ± 0.111 µM in G1/S phase, 2.814 ± 0.075 µM in S phase, 3.022 ± 0.163 µM in G2 phase and 1.600 ± 0.254 µM in mitosis. (Figure 21A)

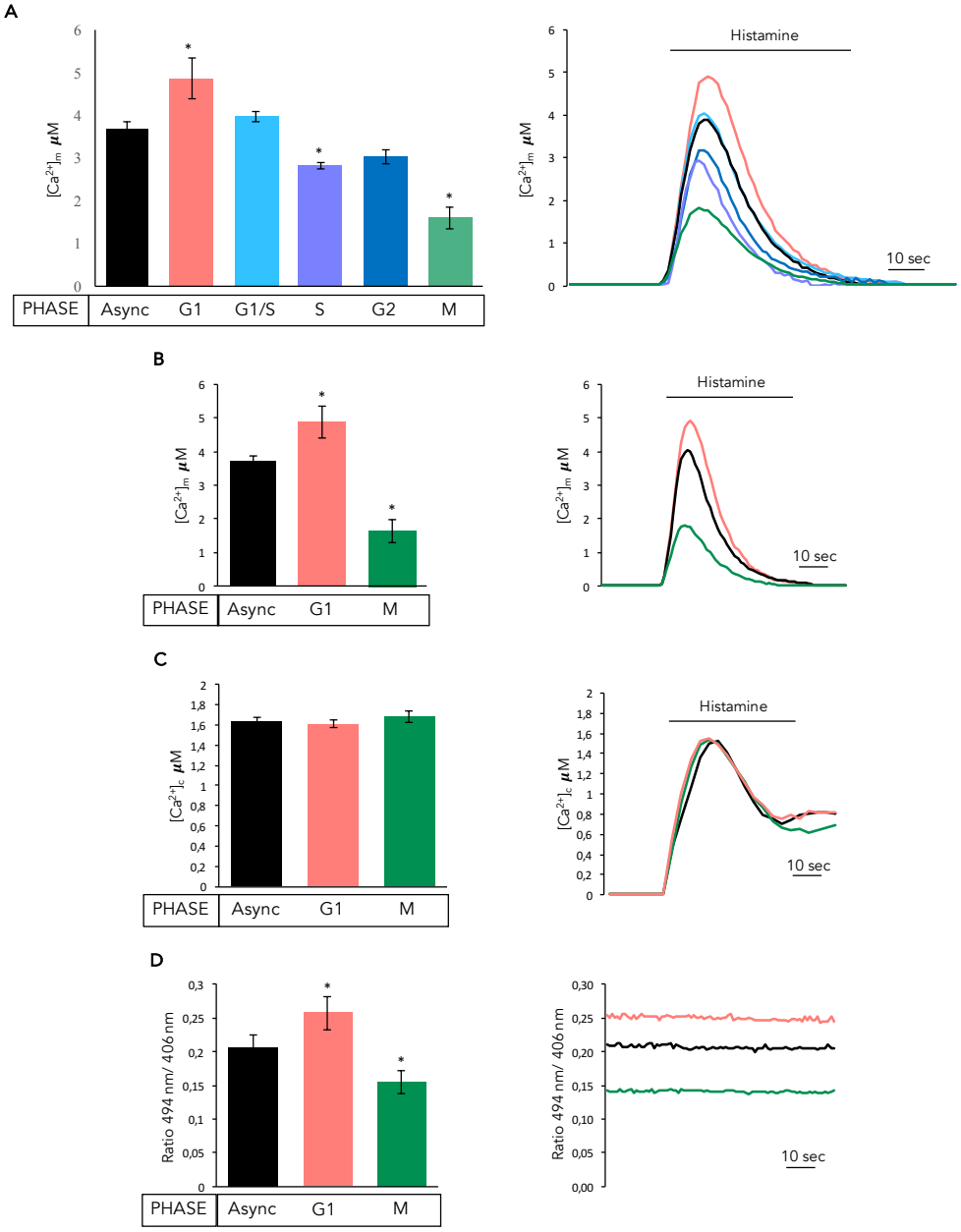

Figure 21 - T98G cell display a very low $[Ca^{2+}]_m$ in mitosis. A: Measurement of $[Ca^{2+}]$ using recombinant aequorin upon agonist (100 µM Instamine) stimulation in mitochondria. Cells were synchronized in G1, G1/S, S, G2 and M phase. On the right panel representative traces. **B:** Asynchronous, G1 and mitotic cells measures of A grouped, with representative traces. **C:** Measurement of $[Ca^{2+}]$ using aequorin upon agonist (100 µM Instamine) stimulation into the cytosol. Cells were synchronized in G1 and M phase. **D:** Assessment of mitochondrial Ca^{2+} loading on nonstimulated cells through the use of a ratiometric high-affinity GFP-based fluorescent Ca^{2+} indicator (2mtGCaMP6m) with representative traces. N = 48 experiments per condition The data are presented as means ± SEM *p<0.05.

Then, we decided to focus on G1 and M phases, both for experimental simplification and because, as we have previously observed, this transition displays more significant changes in $[Ca^{2+}]_m$.

The mitotic and G1 phases are also considered the most critical phases for cell destiny; G1 phase is particularly important because it determines whether a cell commits to the division or to leaving the cell cycle in the G1 checkpoint and mitosis and cytokines control the division into two healthy and functional cells.

In Figure 21B we grouped the values obtained from non-synchronized, G1 and mitotic cell measurements; cells in G1 phase display significantly higher $[Ca^{2+}]$ after agonist-induced stimulation and, on the contrary, cells in M phase highlight deficient mitochondrial calcium concentrations.

After evaluating calcium maximum uptake capacity at mitochondrial compartment, we wanted to assess the cytosolic concentration of this cation. This measurement can be useful to understand if the differences we have found in calcium concentration are attributable only to the mitochondrial compartment and not, for example, to differences in calcium release from intracellular stores. We founded no significant differences in $[Ca^{2+}]_c$ after agonist stimulation in the conditions under consideration. (Figure 21C)

Having attributed the effect we saw on $[Ca^{2+}]_m$ only to mitochondria compartment itself, we then evaluated $[Ca^{2+}]$ in the mitochondrial matrix in resting conditions.

By using a ratiometric high-affinity GFP-based fluorescent Ca^{2+} indicator (2mtGCaMP6m), we measured mitochondrial Ca^{2+} loading of nonstimulated cells. We can appreciate that, even in resting conditions, mitochondria follow a trend similar to the one highlighted after agonist stimulation. In particular, asynchronous T98G cells have a $[Ca^{2+}]_m$ of 0.206 ± 0.018 μM, 0.257 ± 0.024 μM in G1 and 0.155 ± 0.016 μM in M phase. (Figure 21D)

3.3.2 The mitochondrial calcium uniporter subunit MCUb accumulates through cell cycle phases, reaching its maximum in mitosis.

Ca^{2+} ions, released from the ER by IP3Rs, cross the freely permeable OMM through voltage-dependent anion channels (VDACs). Here calcium reaches the inner mitochondrial membrane (IMM), and accumulate in the matrix via the mitochondrial Ca^{2+} uniporter (MCU) complex, thanks to these microdomains which overcome the low apparent Ca^{2+} affinity of the MCU.

As described in the introductive section of this thesis work, MCU complex is composed of the pore-forming subunit MCU and some other proteins that act as regulators for calcium uptake into the mitochondria. Among them certainly stand out MICU1 (that stabilizes the

closed state of the MCU complex and cooperates with MCU to allow Ca^{2+} accumulation inside the matrix), EMRE (that interacts with MICU1 at IMS and with MCU oligomers in the inner membrane acting as a bridge between the Ca^{2+}-sensing activity of MICU1 and the channel properties of MCU) MCUb (that act as an endogenous dominant-negative isoform; the insertion of one or more MCUb subunits in the multimer negatively alter Ca^{2+} permeation) and MCUR1 (that seems to be necessary for mitochondrial Ca^{2+} uptake).

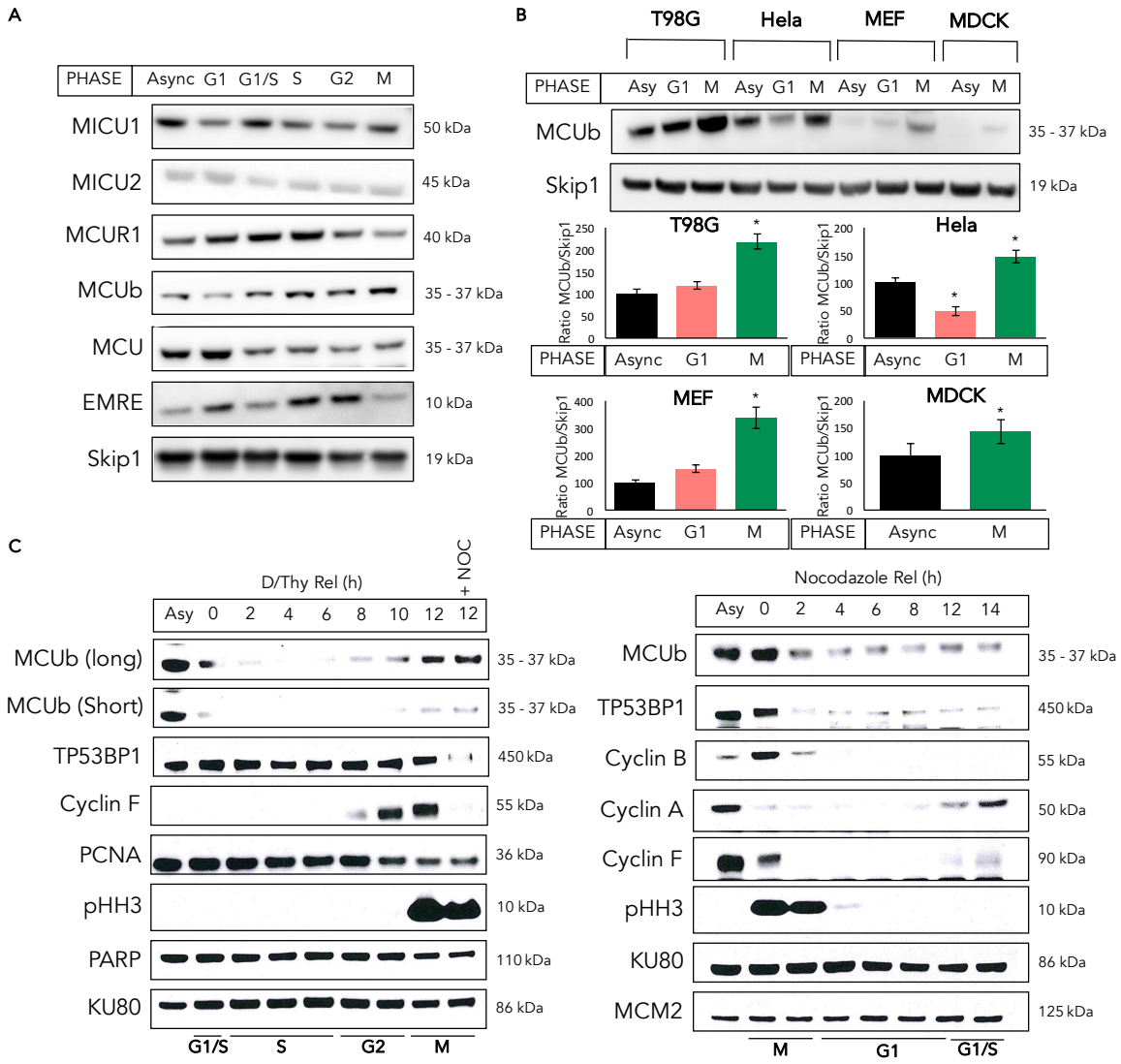

Figure 22 - The increased expression in M phase of the mitochondrial uniporter dominant negative subunit MCUb could explain the low $[Ca^{2+}]_m$. A: Western Blot analysis of the MCU complex subunits on synchronized T98G cells. Antibodies against MCU, MCUb, MICU1, MICU2, MCUR1 and EMRE was used. Skp1 was used as protein loading control. **B:** Immunoblot with antibody against MCUb performed in asynchronized, G1 and M phase T98G, Hela, MEF and MDCK cells. Skp1 was used as protein loading control. On the bottom: MCUb/Skip1 ratio quantifications. **C:** Double Thymidine release (left) and Nocodazole block and release (right) techniques are used to synchronize and analyze through Western Blot T98G cells. Cyclin F, pHH3, TP53BP1, Cyclin B and Cyclin A was used as synchronization marker, PCNA, PARP, KU80, and MCM2 was used as protein loading controls. N = 3 independent experiments per condition. The data are presented as means ± SEM *p<0.05.

Having highlighted these fluctuations in mitochondrial calcium concentration, we have thought to evaluate protein amount of the MCU complex subunits through cell cycle phases. To reach this goal, we performed Western Blot analysis in synchronized T98G cells, using antibodies against MCU, EMRE, MICU1, MCUb, MICU2 and MCUR1. As can be observed from Figure 22A, the concentration of MCU complex-forming proteins changes, in some conditions also significantly. However, the data that most closely correlate with our previous observations concerning $[Ca^{2+}]_m$ is located in MCUb stripe. In fact, MCUb, being the dominant-negative isoform of MCU, have no affinity to Ca^{2+} and prevents the passage of this ion into the mitochondrial matrix. The significant amount of MCUb in M phase could explain the poor uptake of mitochondrial calcium in this particular phase of the cell cycle. Therefore, we decided to extend this assessment to other cellular models, coming from different organisms and compartments. This experiment will serve as confirmation or denial of this tendency. For this test, we used T98G, Hela (from human cervix epitheloid carcinoma), MEF (mouse embryo fibroblast) and MDCK (from canine Cocker Spaniel kidney).

We obtained that MCUb amount is significantly enriched in mitosis compared to asynchronous and G1 phase cells in all cell types. (Figure 22B)

We then analyzed the degradation/accumulation of MCUb through the cell cycle in Hela cells and we used two of the most popular synchronization methods: double-thymidine arrest and release and nocodazole block and release. We utilized Hela cells for this experiment as they have a faster cell cycle (about 20 hours, versus 36 hours needed to T98G cells to complete an entire cycle) and because using nocodazole block and release we can follow cells even after M phase. Furthermore, as we have observed in Figure 22B, the behavior of MCUb protein in Hela is similar to that seen in T98G cells.

In this manner, it was possible to see how MCUb gradually accumulates throughout the cell cycle, reaching the maximum amount in mitosis. After M phase, MCUb concentration progressively decreases. PARP, Ku80 and MCM2 are used as loading markers. (Figure 22C)

3.3.3 MCUb-overexpressing and MCUb-shRNA clones differ in mitochondrial calcium uptake, chiefly in M phase.

Having noticed and confirmed this MCUb accumulation in mitosis, even in different cell types, we thought to characterize the role of MCUb upon genetic manipulation. We aimed to evaluate whether the altered expression of MCUb can cause perturbations in cell cycle progression. Most cell biology experiments utilize transient transfection protocols that afford peak gene expression between 24-96 hours post-transfection. However, if sustained gene

expression is required, generation of stable cell lines is a viable option. We generate four T98G pcDNA3 (which we will use as a control condition) and four T98G MCUb-overexpressing clones. We have selected two pcDNA3 (Clone 1 and 2) and two MCUb (Clone 1 and 3) representative clones, which will be used in future experiments to obtain good statistics. (Figure 23A) Similarly, two control clones (plko 1 and 2) and MCUb-silencing clones (MCUb-shRNA 1 and 4) were selected. (Figure 23B)

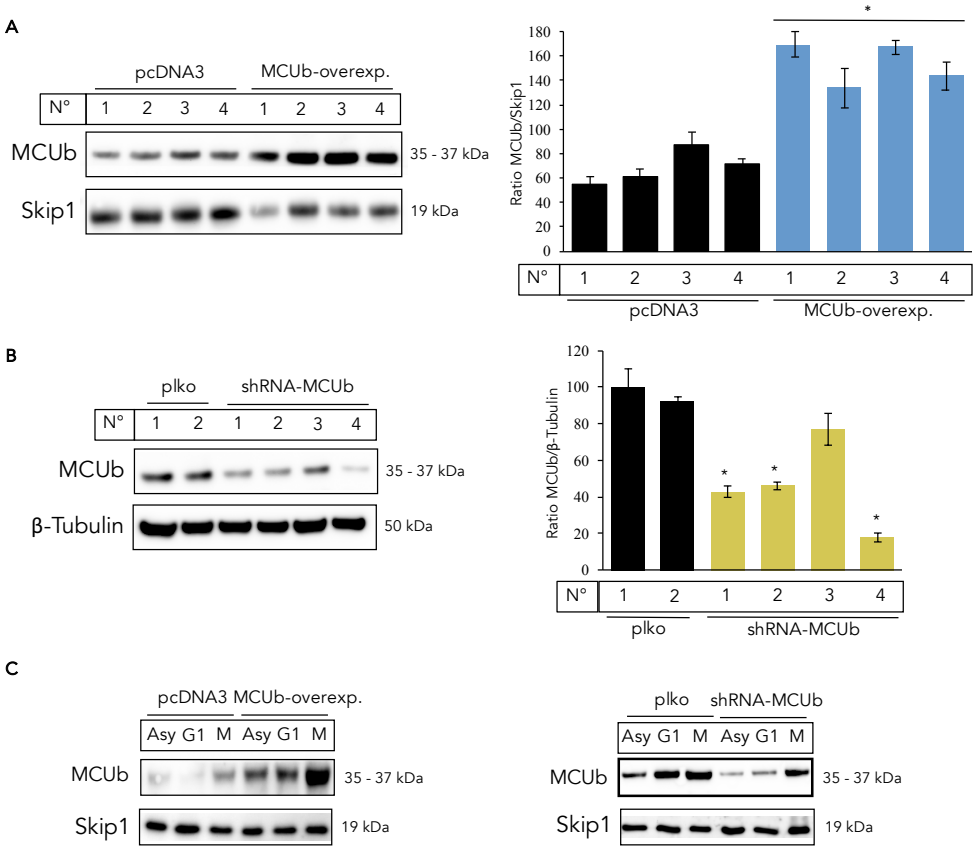

Figure 23 - Generation of MCUb-overexpressing and MCUb-shRNA Clones. A: T98G cells were transfected with the cDNA for pcDNA3 (empty vector) and pcDNA3-MCUb and, after 36h , transfected cells were selected with the addiction of G418 to the medium (0,8 mg/ml). A western blot analysis was performed with antibody against MCUb to select the best clones. Skp1 was used as protein loading control. On the right side: MCUb/Skip1 ratio quantifications. **B:** T98G cells were infected by adding plko (vector) and MCUb shRNA lentiviral particles to the culture. To select stable clones expressing the shRNA, puromycin (8 μg/ml) was added to colture medium. A western blot analysis was performed with antibody against MCUb to select the best clones. Skip1 was used as protein loading control. On the right side: MCUb/Skip1 ratio quantifications. **C:** MCUb assessment through Western Blot technique in synchronized MCUb overexpressing and MCUb-shRNA clones. N = 3 independent experiments per condition. The data are presented as means ± SEM. *p<0.05

Firstly, we want to evaluate the MCUb expression pattern in newly generated clones during the cell cycle. As can be seen in Figure 23C, MCUb concentration variations have been maintained, but amplified in clones over-expressing the protein and attenuated in MCUb-shRNAs. Anyhow, mitosis continues to be the cell phase in which MCUb is more expressed in all clones. (Figure 23C)

After that, we moved to mitochondrial calcium in clones. We measured $[Ca^{2+}]_m$ after agonist stimulation both in overexpressing and silenced MCUb clones. What we want to evaluate is whether there are any differences between cell cycle phases, as happens in our cellular model.

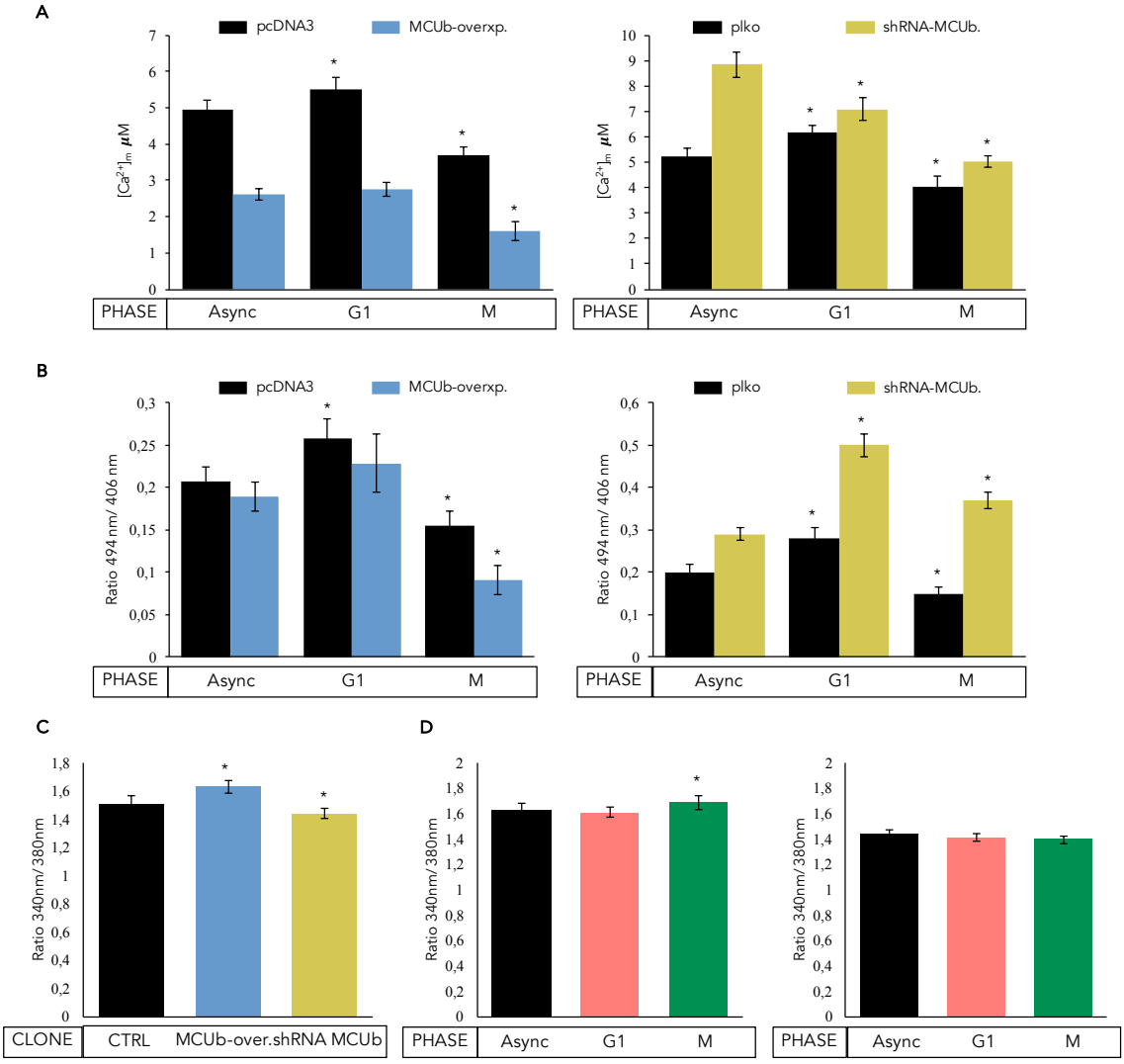

Figure 24 - Calcium assessments on MCUb overexpressing and silenced clones confirm the key role of this uniporter subunit in mitochondrial calcium uptake in mitosis. A: Measurement of $[Ca^{2+}]$ using recombinant aequorin upon agonist (100 µM Instamine) stimulation in mitochondria. Assessments in asynchronous and in G1 and M phase synchronized MCUb overexpressing (left panel) and silenced (right panel) clones. N = 48 independent experiments per condition. **B:** Assessment of mitochondrial Ca^{2+} loading on nonstimulated asynchronous and G1 and M phase synchronized clones through the use of 2mtGCaMP6m. Measurements were made on MCUb overexpressing (left panel) and silenced (right panel) clones. **C:** Clones cytosolic free Ca^{2+} concentration was evaluated using fluorescent Ca^{2+} indicator Fura-2/AM (Molecular Probes, Inc.). **D:** Cytosolic free Ca^{2+} concentration measurements in asynchronous and in G1 and M phase synchronized MCUb overexpressing (left panel) and silenced (right panel) clones. N = 25 visual fields per condition. The data are presented as means ± SEM. *p<0.05

We noticed that the major effect of MCUb overexpression in mitochondrial calcium uptake is achieved in phase M; $[Ca^{2+}]_m$ results decreased in all cell cycle phases analyzed (asynchronized pcDNA3 clones= 4,943 ± 0,285 µM; asynchronized MCUb-overexpressing

clones = 2,599 ± 0,156 μM), but in mitosis reaches significantly lower levels (M phase pcDNA3 clones = 3,685 ± 0,233 μM; M phase MCUb-overexpressing clones = 1,593 ± 0,263 μM). (Figure 24A) In asynchronous MCUb silenced clones, after agonist stimulation $[Ca^{2+}]_m$ is much higher than non-synchronized T98G controls (plko clones = 5,208 ± 0,353 μM; MCUb-shRNA clones = 8,844 ± 0,511 μM). Such differences are attenuated in G1 and M phases while maintaining a higher concentration of mitochondrial calcium than cells in which MCUb expression has not been muted. (Figure 24B)

Even in resting $[Ca^{2+}]_m$, the most significant differences were found in mitosis, confirming the hypothesis that MCUb can play an important role in this specific phase of cell cycle. (Figure 24A and B) A further confirmation of this statement arises from $[Ca^{2+}]_c$ measurements; both in overexpressing and in silenced MCUb clones, we didn't find significant differences in the cytosolic compartment, apart from an increase in mitotic MCUb over-expressing cells. (Figure 24D)

Still looking at the cytosolic level, there are appreciable differences in $[Ca^{2+}]_c$ between the two clone types that we attribute to a sort of "mitochondrial buffering action" that we will discuss later. In fact, in nonstimulated cells, cytosolic $[Ca^{2+}]$ follow the trend we highlighted in mitochondria. Control clones have a basal $[Ca^{2+}]_c$ which stands out 1.511 ± 0.051 μM, 1,628 ± 0.041 μM for MCUb-overexpressing cells and 1,439 ± 0.038 μM for MCUb-silenced clones. (Figure 24C)

3.3.4 MCUb-overexpressing clones present a tumoral connotation.

At this point, having realized that MCUb plays an important role in controlling $[Ca^{2+}]_m$ and uptake during the mitotic process, we went to evaluate whether modulation of this protein expression would influence cell cycle progression and cell viability. A fascinating aspect of Ca^{2+} signaling that highlights its dramatic importance in the evolution of multicellular organisms is its capacity to regulate cell death. Indeed, multicellular organisms require tight control of the cellular Ca^{2+} concentrations to allow proper tissue homeostasis; loss of this control results in excess proliferation (which may lead to malignancies) or loss of tissue function (neurodegenerative pathologies). MCUb high expression in M phase may be, for any reason, a useful mechanism adopted from the cell to attenuate calcium entry into the mitochondria. By modulating this protein expression, in next experiments, we evaluated if any change in cell cycle progression and/or cell health occurs.

First of all, we perform a growth assay; we sowed the same number of cells in plates, and then fixed to regular time intervals (24 h), to evaluate their growth in culture. In the end, we labeled cell DNA with the triarylmethane dye crystal violet. The amount of DNA in each

cell remains constant for a given cell line or cell type, so assays based on DNA content can be used to provide an accurate and straightforward measure of cell number. As we can see in Figure 25A, after five days we could find a more significant amount of MCUb-overexpressing cells compared to pcDNA3 clones. On the other hand, cells, where MCUb was silenced, have a significantly lower/slower growth in culture.

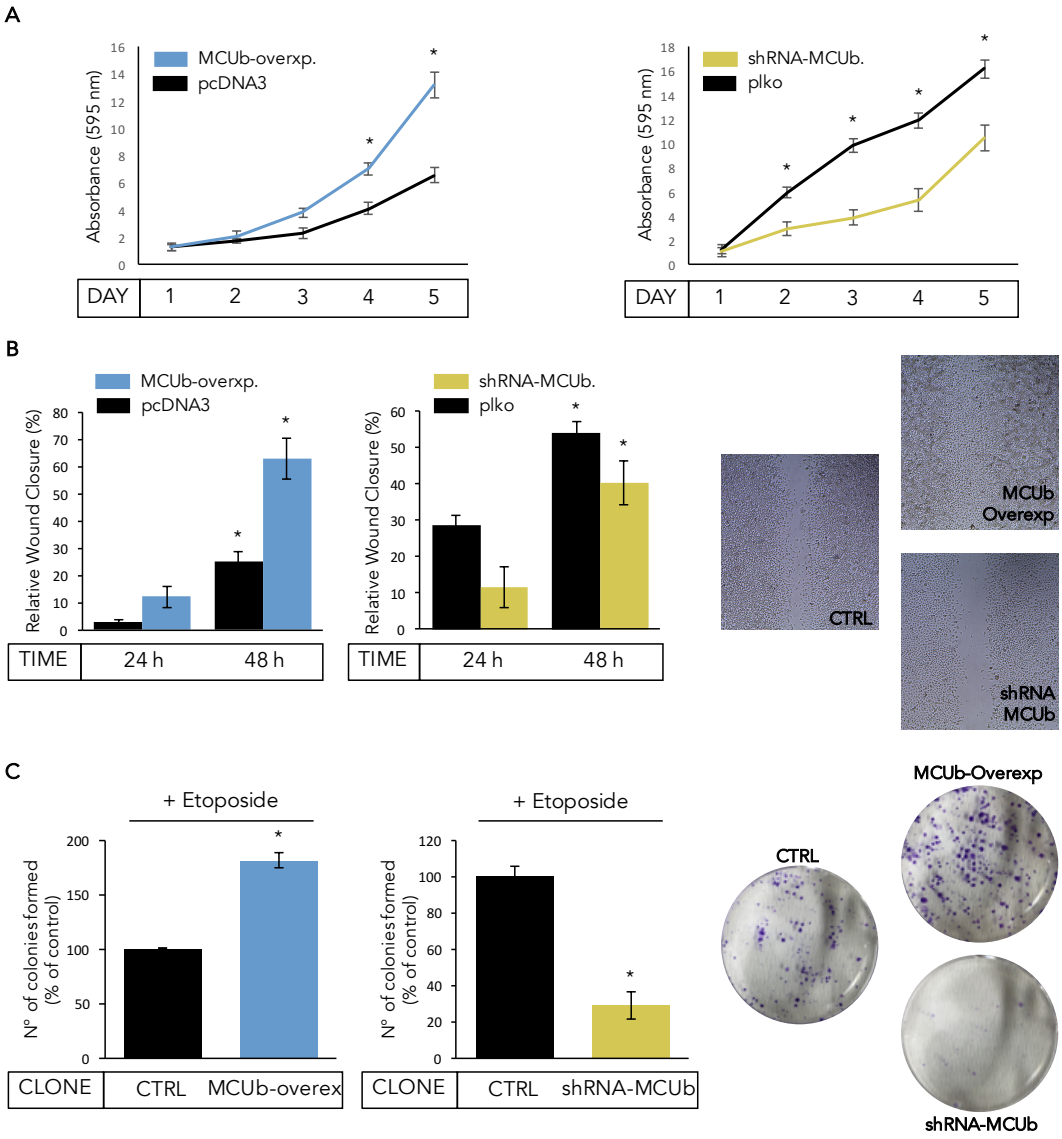

Figure 25 - MCUb clones demonstrate a different predisposition to growth in culture, invasiveness and ability to produce progeny following genotoxic damage. A: MCUb-overexpressing (left) and shRNA-MCUb (right) clones growth curves. Cells were seeded (15000 cells x well) in 6-well plates, seeded on 5 plates; one plate for each day. Every 24h a plate was fixed using 4% paraformaldehyde in PBS for 15 min. After 5 days cells was stained with 0.1% crystal violet for 20 min. 1 ml 10% acetic acid was added to each well to extract the crystal violet from cells, and the absorbance at 595 nm was measured. **B:** Wound healing assay was made in both MCUb overexpressing (left) and MCUb silencing (center) clones with 24 and 48 hours of recovery. On the left: representative images. **C:** Analysis of clonogenic survival in MCUb overexpressing (left) and MCUb silencing (center) clones exposed to Etoposide (10 µM) treatment in vitro. On the right: representative images of clonogenic assays. Before seeding, cells were pre-treated with 10 µM Etoposide for 3h. Cells were than detached and seeded into 6-well plates at a density of 1000 cells per well. 25 days after, the cells were fixed and a clonogenic assay was carried out. All the data are the average of 3 independent experiments. The data are presented as means ± SEM. *p<0.05

To study clones migration potential and the coordinated movement of the cell population we decided to perform the wound-healing assay. By comparing the tracks of MCUb-overexpressing and silenced clones with surrounding control cells under the same experimental conditions we can assert that MCUb could cover a role in the regulation of directional cell migration. (Figure 25B)

The clonogenic (or colony forming) assay enables an assessment of the differences in reproductive viability (capacity of cells to produce progeny) between control untreated cells and cells that have undergone various treatments. We perform this experiment following a pre-treatment with Etoposide 10 μM. Etoposide is a topoisomerase II inhibitor, known to induce DNA strand breaks.

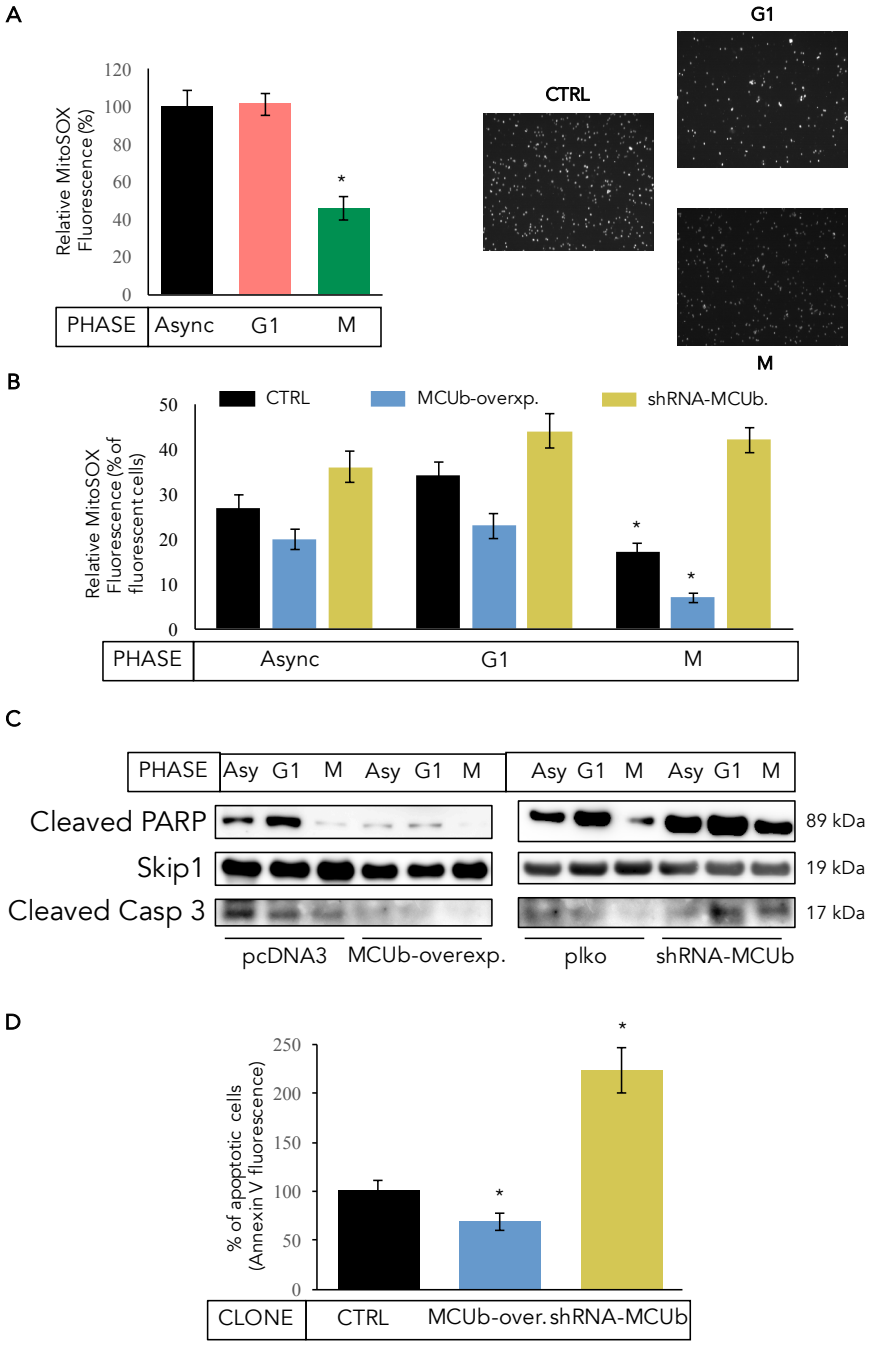

Figure 26 - MCUb overerxpression protects cells from ROS production and accumulation and apoptotic death. A: Meaurement of mitochondrial ROS production in T98G cells by using MitoSOX Red (final concentration: 5 μM) probe and evaluated by using the Tali Image-Based Cytometer. On the right: representative images of MitoSOX Red fluorescence intensity. **B:** Measurement of mitochondrial ROS production in MCUb overexpressing and MCUb silencing clones by using MitoSOX Red (final concentration: 5 μM) probe and evaluated by using the Tali Image-Based Cytometer. **C:** Detection of apoptotic activity in MCUb clones by immunoblot technique using antibodies against cleaved-PARP-1 and cleaved-Caspase 3 apoptotic markers. **D:** apoptotic rate detected by The Tali Apoptosis Assay Kit–Annexin V Alexa Fluor 488 nm. N = 3 independent experiments per condition. The data are presented as means ± SEM. *p<0.05

The data indicated a different ability to produce progeny following genotoxic damage, precisely in favor of MCUb-overexpressing clones, also denoting a possible tumor potential of these cells. (Figure 25C) Taken together these data suggest that MCUb could play an essential role in the progression of the cell cycle by regulating the proper course of one of the most delicate phases: mitosis.

After evaluating cell viability, we focused on the production and accumulation of oxygen reactive species and cell death. We performed ROS measurements by using MitoSOX Red probe; this probe permeates live cells where, selectively targeting mitochondria, is rapidly oxidized by superoxide. The oxidized product is highly fluorescent and signal intensity was evaluated by using the Tali Image-Based Cytometer. We founded a significant lower production and accumulation of ROS in mitosis in T98G cells, but no differences were highlighted in asynchronous and G1 phase cells. (Figure 26A) Moreover, the differences were noticed much more markedly by going to analyze the fluorescence produced by ROS in MCUb clones. shRNA-MCUb clones show a sustained ROS production in all the considered conditions; red fluorescence has been very intense. This fluorescence doesn't explain any significant differences because, we think, it's at its highest. Clones overexpressing MCUb mainly display a lower production and accumulation of ROS, with negligible levels in M phase. (Figure 26B) After that we switched to apoptosis in clones with two different detection techniques. We evaluated PARP and Caspase 3 expression (two of the most widely used apoptotic markers) through Western blot analysis, highlighting a sustained apoptotic activity in MCUb-silenced clones compared to control and even more compared to MCUb-overexpressing clones. Noteworthy, in all conditions taken in the study, mitosis is the phase in which we have noticed the lesser expression of apoptotic markers. (Figure 26C) To confirm data obtained from Western Blot, we proceeded with an apoptotic death analysis using the Annexin V probe. Highly fluorescent Annexin V conjugates provide quick and reliable detection method for studying the externalization of phosphatidylserine that happens in the intermediate stages of apoptosis. Even using this technique, we have been able to appreciate an increase in apoptotic mortality rate, which is attested to more than 200%. (Figure 26D)

Having seen that MCUb influences viability but also cell growth we have decided to deepen the cell cycle progression analysis in the clones we generated. For a thorough study, we have developed a pulse and chase protocol using propidium iodide (PI) and the thymidine analog bromodeoxyuridine (BrdU) as probes and a cytofluorimeter. BrdU can be incorporated into the newly synthesized DNA of replicating cells during the S phase of the cell cycle, substituting for thymidine during DNA replication. Clones were pulse-labeled for 30 min with BrdU and then chased for increasing times with BrdU-free medium. In this way, BrdU is incorporated into newly synthesized DNA in cells entering and progressing through the S phase of the cell cycle.

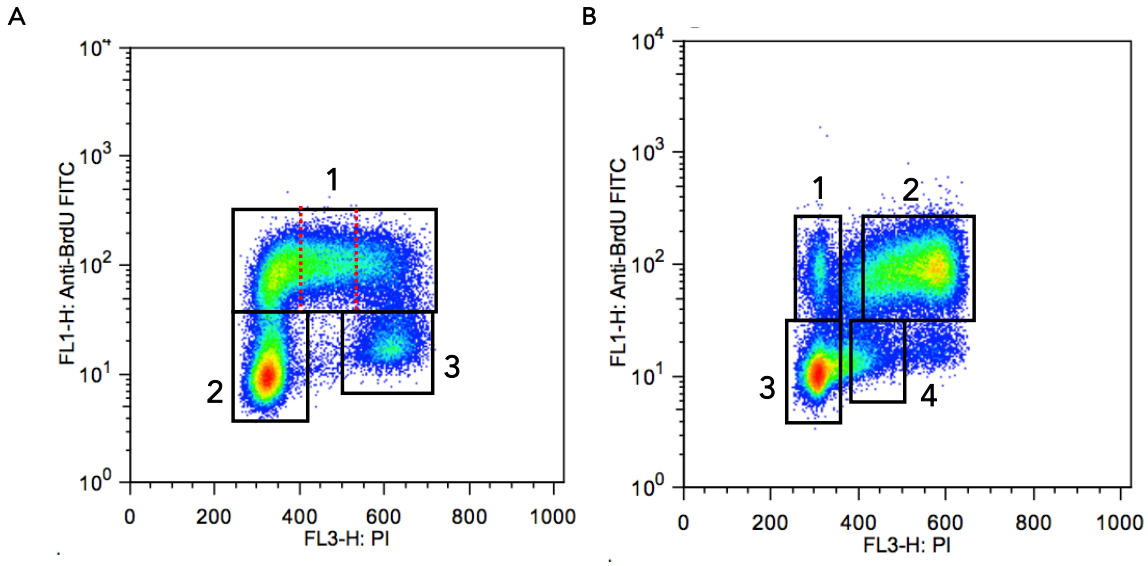

Figure 27 - Representative images from flow cytometric BrdUrd-pulse-chase assay for measurements of progression through the cell cycle: contour plots of DNA content versus log BrdUrd-FITC histograms of asynchronously growing T98Gs and their subdivision into cell cycle compartments. **A**: exponentially growing, asynchronous population of T98Gs analyzed immediately after a 30-min pulse labeling with BrdUrd; **1:** BrdUrd-positive undivided S-phase cells; **2:** BrdUrd-negative G1 cells; **3:** BrdUrd-negative G2 cells; **B:** BrdUrd pulse-labeled T98G cells were followed in culture for 8h in BrdUrd-free regular growth medium before analysis. Four cell cycle compartments were identified as follows: **1:** BrdUrd-positive G1 cells that have completed cell division; **2:** BrdUrd-positive undivided S-phase cells; **3:** BrdUrd-negative G1 cells; **4:** BrdUrd-negative S-phase cells.

The incorporated BrdU is then stained with specific fluorescently labeled anti-BrdU antibodies, and the levels of cell-associated BrdU measured using flow cytometry. What will result will be a histogram like those shown in Figure 27. Typically, what can be seen in Figure 27A is an exponentially growing, asynchronous population of cells that are analyzed immediately after BrdU labelling. In Figure 27B there is an example of what we could see when cells were labelled and allowed to grow in BrdU-free medium for 12 h before analysis. Five cell-cycle compartments are identified: Figure 27A-1 BrdU-positive undivided cells; Figure 27B-1 BrdU-positive G1 divided cells that have completed a cell division; Figure

27A-3 BrdUrd-negative G2 cells; Figure 27A-2 and 27B-3 BrdU-negative G1 cells and Figure 27B-4 BrdU-negative G1/S cells.

At the beginning of the chase, all cells in S phase were labeled with BrdU, while the majority of the cells in G1 and G2/M phases were negative for BrdU staining. Using as a method of analysis the only quantification of cells in S phase, thus eliminating the BrdU negative cells, we can divide the histogram into three zones: cells in early S phase (with a 2n genetic make-up), in middle S phase (2/4n) and in late S phase (4n genetic make-up).

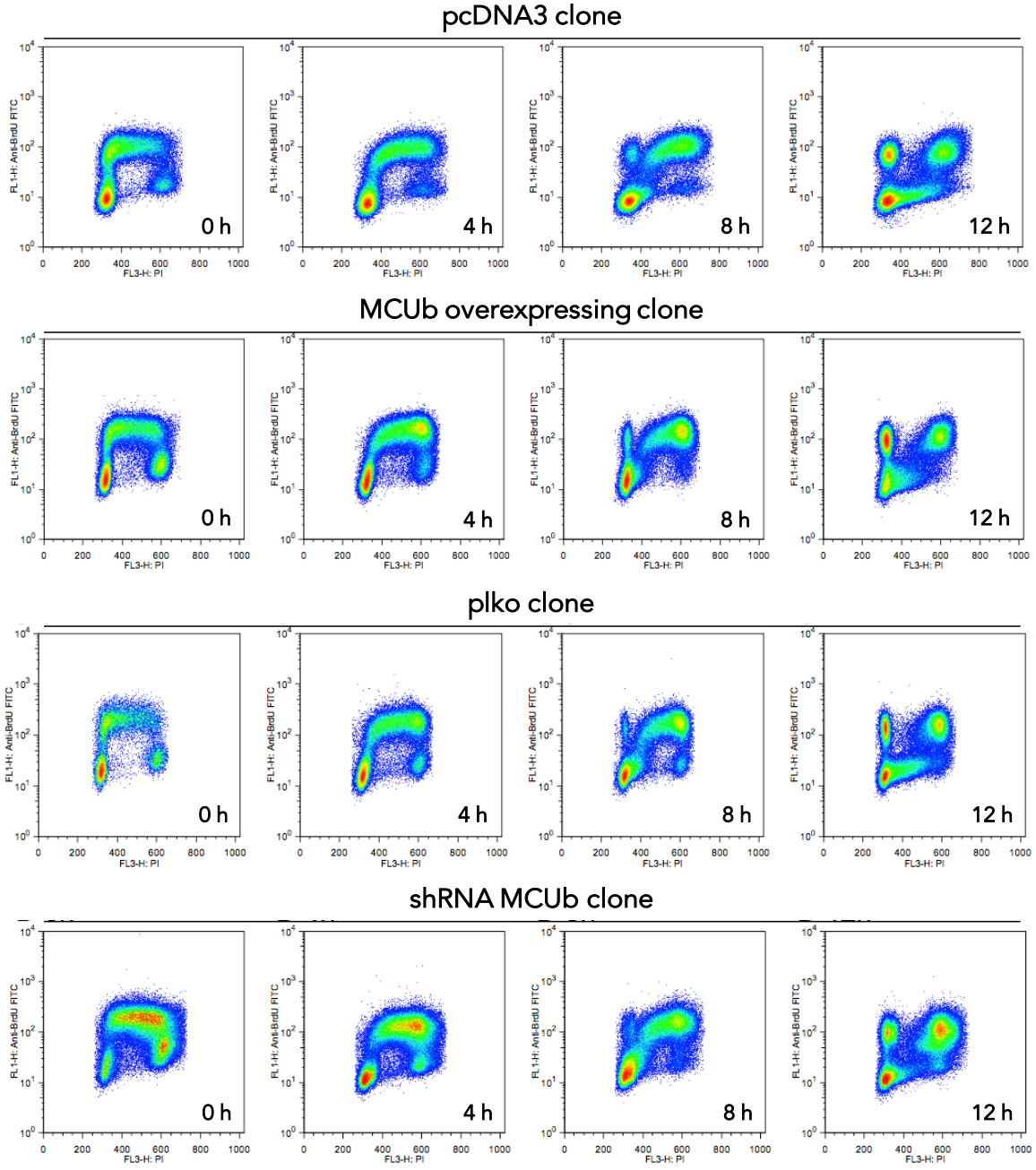

Figure 28 - BrdUrd-pulse-chase assay on MCUb clones for the measurement of the progression through the cell cycle. Pulse and chase protocol using propidium iodide (PI) and the thymidine analog bromodeoxyuridine (BrdU) as probes in a citofluorimeter. MCUb overexpressing and MCUb silencing clones were pulse-labeled for 30 min with BrdU and then chased for increasing times (0h, 4h, 8h and 12h) with BrdU-free medium.

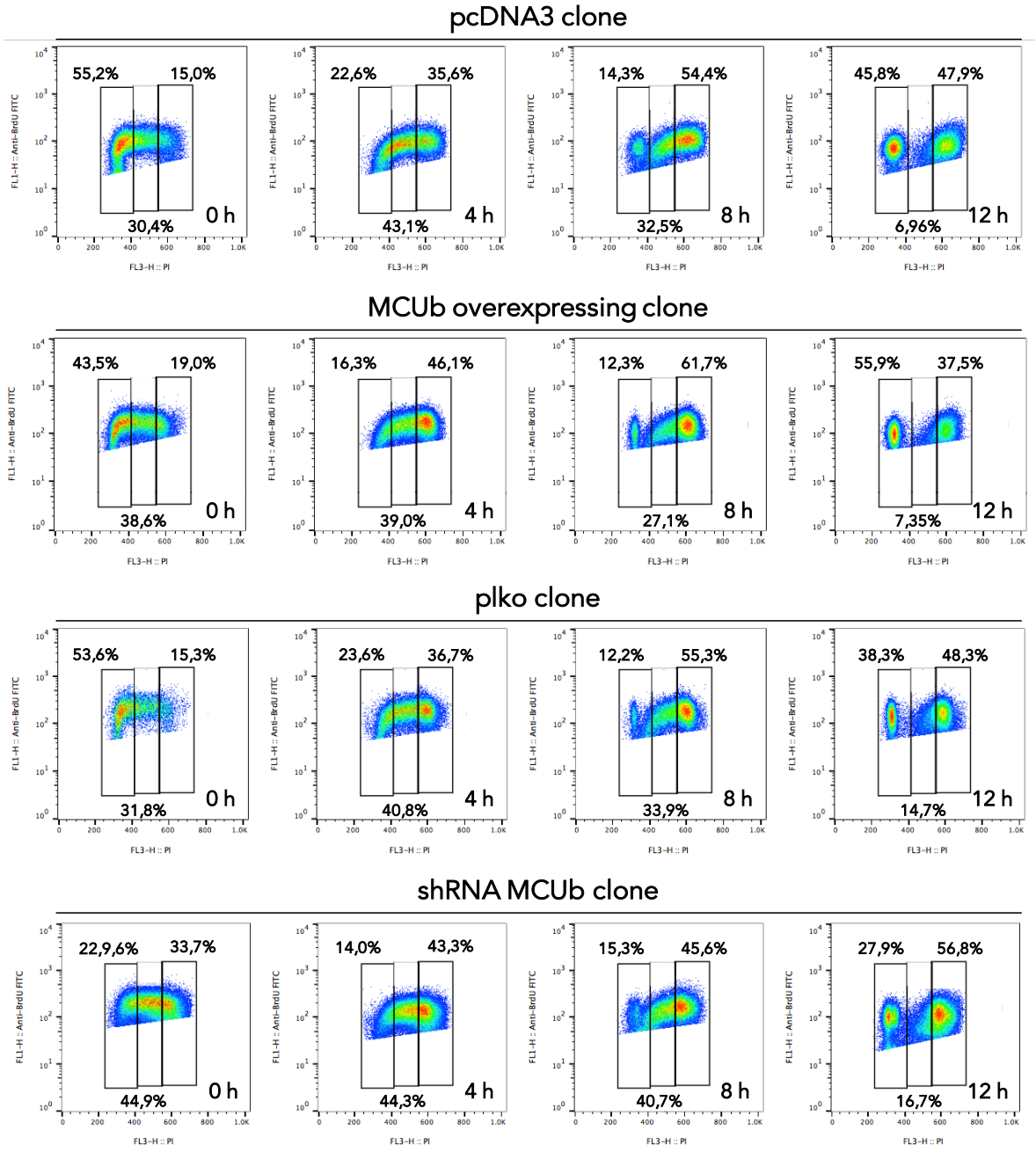

Figure 29 - BrdUrd-pulse-chase analysis on MCUb clones for the measurement of the progression through the cell cycle. Clones negative for BrdU staining were ecluded from histograms and early S (2n), middle S (2n-4n) and late S (4n) cells are divided and quantified (expressed as a percentage) through the use of FlowJo analysis software. Percentages are referred to the number of cells in each phase.

This discrimination is made possible by the use of PI, a fluorescent intercalating agent used as a DNA stain in flow cytometry to evaluate DNA content in cell cycle analysis. After a chase of 8 h, BrdU-positive pcDNA3 and plko clones cells were enriched in middle/late S phase. In late S phase, we could find in fact the 54,4% of pcDNA3 clones and the 55,3% of plko cells. (Figure 29) The majority of BrdU-positive MCUb-overexpressing clones cells are instead in late S phase (even the 61,7%). MCUb-silenced clones cells were primarily in early/middle S phase, only the 45,6% of cells could be found in late S phase. These data

indicate that there are different progression velocities through the cell cycle, and clones overexpressing the MCUb protein cycle faster. Another evidence is represented by BrdU-positive cells divided after a chase of 12 h. In MCUb overexpressing clones, the 55,9% of the population is adequately divided; only the 27,9% of MCUb-silenced clones have completed a whole cell cycle and are now again in early S phase. (Figure 29)

3.3.5 Mitotic MCUb accumulation allows the correct calcium signaling through intracellular calcium transients.

Low $[Ca^{2+}]_m$, due to the higher concentration of MCUb subunits in MCU complex in mitosis, improve cell cycle velocity and protect cells from apoptosis and ROS production and accumulation. It remains to be clarified how this could happen. We hypothesized that the core was to be sought in cytoplasmatic calcium concentration, rather than in the mitochondrial one.

In fact, spontaneous Ca^{2+} events have been observed in various stem cell lines, including carcinoma and mesenchymal stem cells. Indeed, during cell cycle progression, cells exhibit Ca^{2+} transients during the G1 to S transition and mitosis, suggesting that these oscillations may play some role in cell cycle progression (*126*). This evidence, associated with the fact that in many cell type it was demonstrated that mitochondrial Ca^{2+} uptake contributes to buffering physiological Ca^{2+} loads, has led us to formulate a thought about how everything will work. We think that cell synthesizes a more considerable amount of MCUb during the mitotic phase, preventing the mitochondria from performing its buffering action; this event should be used to obtain more extended and intense cytoplasmic calcium transients. Then, these Ca^{2+} transients could play their essential role in the progression or the exit from the mitotic phase.

We made 30 min basal $[Ca^{2+}]_c$ measurements using Fura-2 AM probe in asynchronous, G1/S, early M and G1 post-M phases MCUb-silenced clones. Afterwards, we counted the number of peaks, and we evaluated their area, to have an estimate of their amplitude. We noticed calcium transients with peaks of different size, width and frequency between the conditions under consideration. In specific, control cells in M phase show many more peaks of Ca^{2+} with also a higher area under the curve, compared to cells in G1/S phase. Contrariwise, MCUb-silenced clones highlight a smaller number of peaks, with a significantly reduced area below the curve. (Figure 30)

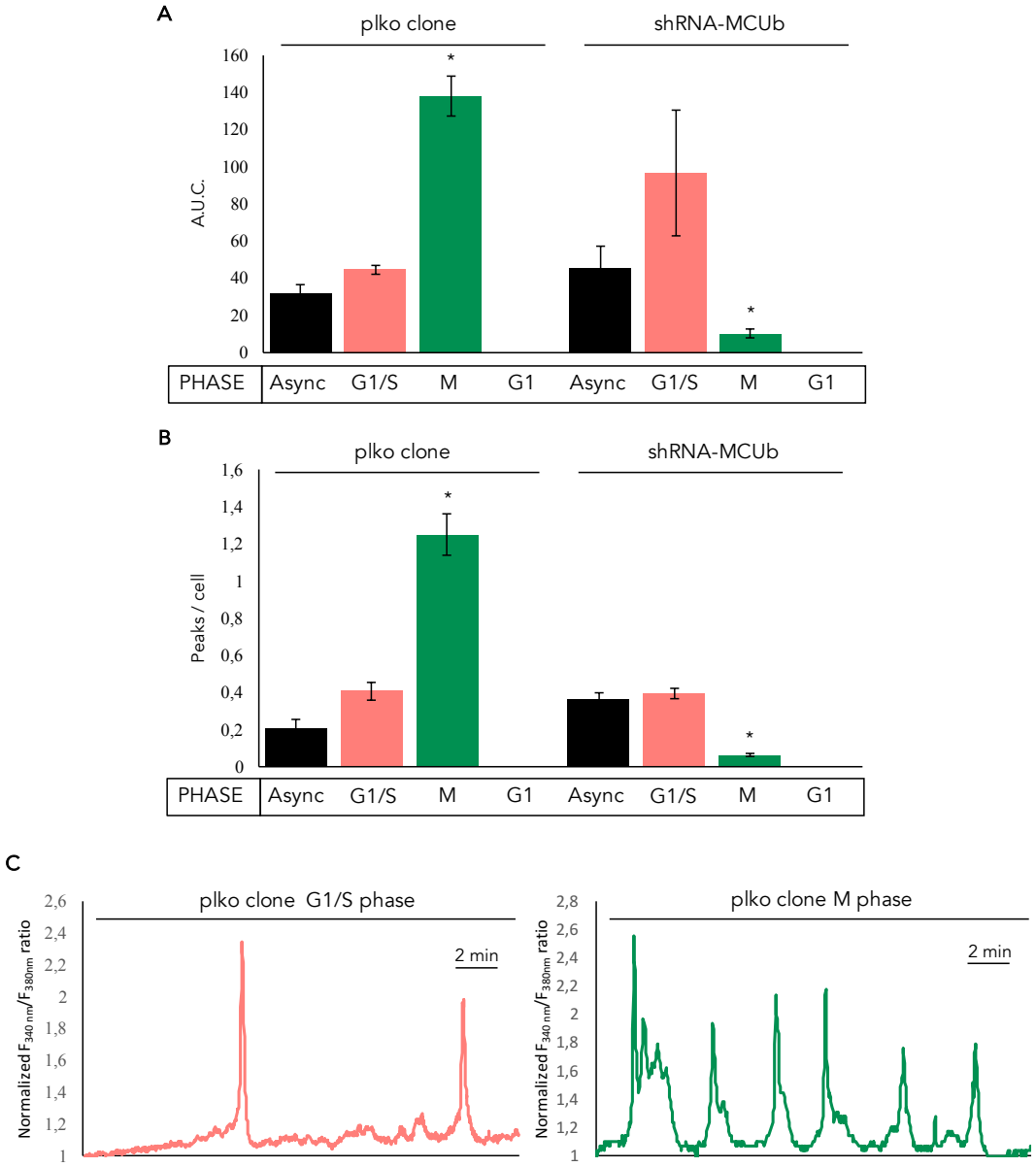

Figure 30 - Calcium handling in MCUb clones. A: summary data for Ca^{2+} transient peak amplitude measured as the area under the curve (A.U.C.), as indicated by the 340 nm-to-380 nm fura-2AM ratio. **B:** summary data for Ca^{2+} transient peak number per cell. Measurements were made in asynchronous, G1/S, early M phase and in G1 after M phase and citokynesis both in MCUb overexpressing and MCUb silencing clones. **C:** representative traces of Ca^{2+} transients in plko clones in G1/S phase (left) and in mitosis (right). N = 12 visual fields per condition. The data are presented as means ± SEM. *p<0.05

3.4 DISCUSSION

The precise regulation and respect of the order of cell cycle progression result necessary for the correct development of an organism. Proteins alterations can trigger an uncontrolled proliferation that often leads to tumor formation. Thus, it is critical that all the events of the cycle are adjusted on multiple levels. The most studied control system is represented by the cyclin/cyclin-dependent kinase (Cdk) complex. Cdks are a family of serine/threonine protein kinase that forms specific complexes with cyclins and ensures cell cycle progression. Cyclins are proteins which are expressed differently in cell cycle phases, as a result of proteasome degradation and transcriptional changes; Cdk, instead, shows constant levels of expression.

A huge number of Ca^{2+}-binding proteins (CaM, CaMK and calcineurin) are involved in the regulation of certain phases of the cell cycle. In fact, several recent works highlight that Ca^{2+}/CaM-dependent pathways contribute to the modulation of cyclin/Cdk complexes at different phases of the cell cycle. (*127-129*)

In the intracellular environment, Ca^{2+} acts as a pleiotropic second messenger that triggers numerous physiological processes such as fertilization of oocytes, differentiation, embryonic pattern formation, proliferation, and cell death (*20*).

In early G1, Ca^{2+} modulates the transcription of immediate early genes, which are essential for cell proliferation. Ca^{2+}/CaM activates the CdK4/cyclin D1 complex, which regulates retinoblastoma protein (RB1) (the primary inhibitor of DNA synthesis) and the progression from G1 to S phase (*130*). The essential involvement of the Ca2+/CaM complex has also mainly been reviewed in the past concerning the transition from G2 to M phase (*131*). In any case, reduction of CaM prevents cells from entering mitosis (*132*). An increase in [Ca^{2+}] is detected just before nuclear envelope breakdown (NEB) maybe because of Ca^{2+} release from local stores. This free Ca^{2+} may activate the CDK1/cyclin B complex leading to disassembly of the nuclear envelope (*133*). The implication and the role of Ca^{2+} in the cell cycle, however, is still a matter of debate.

The majority of the paper published focus on the cytosolic compartment, and for this reason, we thought to analyze, if present, differences in mitochondrial Ca^{2+} uptake.

The first thing to do was to fine-tune a synchronization protocol as accurate as possible. Many of these protocols involve the use of pharmacologic agents that, in addition to being able to act on other cellular processes besides cell cycle, could affect cell health. For this reason, we chose as the primary cellular model a line that doesn't need pharmacologic agents

to get a well-synchronized population. T98G are cells derived from a human glioblastoma tumor that can exit from cell cycle and enter into a quiescent state (G0) after almost complete serum-deprivation from the medium (0,1% FBS). Once the cellular population is in this state of quiescence, cells are washed and released into DMEM plus 10% FBS. At this point, the entire cell population is free to progress through the cell cycle synchronously. For the development of this protocol, we harvested T98G cells every two hours from serum starvation release for 40h; protein expression levels of cell cycle marker were then tested. After 4h from release cells are in G1 phase, in G1/S after 12h, S in 24h, G2 in 30h and mitosis after 36h. After that, we used Cyclin F, Cyclin B, Cyclin A and Phospho-histone H3 (pHH3) levels to confirm the correct synchronization of T98G cell population. An additional confirmation was carried out through the use of a ready-to-use reagent included in a Thermo Fisher' kit for an image-based cytometer named Tali.

Therefore, we proceeded to calcium assessments using the Ca^{2+} sensitive photoprotein aequorin.

$[Ca^{2+}]_m$, measured after agonist stimulation, undergoes a significant change compared to an asynchronous population, in G1 phase, S phase and mitosis. In particular, in the G1 phase, we noticed a substantial increase in $[Ca^{2+}]_m$, and a decrease in S phase that becomes much more pronounced in M.

At this point, we decided to consider only the two most significant phases, both for an experimental simplification and why, as we have seen, those are the stages in which there are more substantial changes in $[Ca^{2+}]_m$. Measurement of mitochondrial calcium concentration after a stimulus gives us an indication of what can be the maximum Ca^{2+} uptake capacity of the organelle. However, these differences may also arise from other non-mitochondrial factors, such as the different release of Ca^{2+} from intracellular stores. To exclude external contributions and attribute the differences we found in $[Ca^{2+}]$ only to the mitochondria compartment, we measured $[Ca^{2+}]_c$. We found no differences in $[Ca^{2+}]_c$, to testify that the differences in mitochondrial calcium uptake we noticed are due to a mitochondrial factor alone. At this point we evaluated $[Ca^{2+}]$ in a "resting condition" mitochondria, i.e., in the absence of agonist stimuli; even in this case, we have seen significantly higher $[Ca^{2+}]_m$ in G1 phase and less in mitosis, compared to non-synchronized cells.

We, therefore, tried to explain these differences by analyzing mitochondria and, specifically, the channel responsible for calcium uptake in the matrix. Relatively recently, it has been identified the mitochondrial Ca^{2+} uniporter MCU, a protein of ≅ 40 kDa expressed in all tissues, which is located in the IMM, with the N-terminal and the C-terminus facing the

matrix. MCU is a low affinity-channel, but it has been shown that mitochondria are exposed to microdomains with high [Ca^{2+}], which represent the contact sites between mitochondria and ER (*134*). The uniporter was recently shown to be a macromolecular complex consisting of pore-forming and regulatory subunits. The pore is physically formed by oligomers of MCU, MICU1 performs a gatekeeping function, stabilizing the closed state of the MCU complex, MICU2 interacts with both MICU1 and MCU, EMRE acts as a bridge between MICU1 activity and the channel proprieties of MCU, MCUb acts as an endogenous dominant-negative isoform interposing between MCU subunits in the pore, MCUR1 seems to be necessary for mitochondrial Ca^{2+} uptake and maintenance of healthy cellular bioenergetics. We then evaluate the endogenous expression of MCU complex proteins in each phase of the cell cycle in T98G by western blot. The concentration of MCU complex-forming proteins changes, in some conditions also significantly, and the data that most closely correlates with lower $[Ca^{2+}]_m$ in mitosis is the great amount of MCUb in M phase we highlighted. The accumulation in mitosis of this protein that prevents calcium access into the mitochondria could explain the reduced uptake in this particular phase of the cell cycle. Of particular interest is the fact that there is a gradual accumulation of MCUb up to M phase, then decreasing in subsequent G1 and S phases. Even more interesting is to have highlighted how this greater protein concentration is maintained in different cell types, coming from both organisms and organs very different from each other.

As it was logical to continue this work we generated a cell line that stably overexpresses and one that stably silences MCUb expression. We selected the clones that showed the highest expression and the lesser expression of MCUb and we used them as a reference cell model in the next experiments. MCUb-overexpressing clones display, as was foreseeable, a lower $[Ca^{2+}]_m$, both at resting conditions and after agonist stimulus; conversely, shRNA-MCUb clones show higher levels of mitochondrial Ca^{2+}. This phenomenon is undoubted to be attributed to the dominant negative action of MCUb on the uniporter complex. In particular, it is interesting to note that MCUb action is particularly amplified in mitosis with deficient calcium concentrations in overexpressing cells and unusually high in shRNA-MCUb clones. In the latter, they reach $[Ca^{2+}]_m$ levels comparable to those highlighted in non-synchronized control cells after stimulus from agonist, and even a lot more talking about basal $[Ca^{2+}]_m$. Even in clones, there are still no differences between cell phases regarding $[Ca^{2+}]_c$, apart from an increase in M phase in MCUb-overexpressing clones. Modifying the MCUb expression has, however, achieved to make a significant difference in $[Ca^{2+}]_c$ and we think this could be due to a sort of “mitochondrial buffering action”.

As we have repeatedly stated in this dissertation work, Ca^{2+} plays essential functions in the mitochondrial compartment; among the most important, there is undoubtedly the regulation of cell growth and cell death. In fact, one of the most well-studied Ca^{2+}-induced cell death pathways is the cross-talk between the ER and mitochondria. These compartments communicate through selective signals in MAMs. At these sites, Ca^{2+} release from the ER is directly taken up by the mitochondria through specialized microdomains. The primary physiological role of Ca^{2+} uptake involves the control of the mitochondrial metabolic activity, as revealed by the ATP production rate. Indeed, the Ca^{2+}-sensitive mitochondrial dehydrogenases (i.e., pyruvate-, α-ketoglutarate- and isocitrate-dehydrogenases) are activated by Ca^{2+}. These three enzymes represent the rate-limiting steps of the Krebs cycle and thus control the supply of electrons into the respiratory chain and the generation of the proton gradient across the inner membrane, which is necessary for Ca^{2+} uptake and ATP production.

In contrast to these physiological parameters, prolonged accumulation of mitochondrial Ca^{2+} may lead to a phenomenon known as the mitochondrial permeability transition (MPT).

For these reasons, we conducted cell growth and cell viability assays in clones, and we could highlight substantial differences, directly associated and proportional to the modulation of the expression of this particular mitochondrial uniporter subunit. We founded that MCUb increases the growth in colture, plays an essential role in the regulation of directional cell migration and increase the ability to produce progeny following genotoxic damage. Taken together these data suggest that MCUb could play a protagonist role in the progression of the cell cycle by regulating the proper course of one of the most delicate phases: mitosis. For some reason still unknown, the cell accumulates MCUb at M phase to keep calcium concentration low in the mitochondrial matrix. We know that a high concentration of calcium into the mitochondria leads to a high production and accumulation of ROS and, if at high levels, to cell death through the apoptotic process. Evaluating ROS production in T98G cells, we found significantly lower oxygen reactive species levels in M phase compared to asynchronous and G1 phase cells, which are mutually comparable. Clones overexpressing MCUb show a further decline in ROS concentration, supporting MCUb' protective function on ROS production and accumulation. Clones where the expression of MCUb is silenced, however, showed always very sustained levels in all the phases we have analyzed, with no significant differences. A similar observation can be made about apoptotic cell death, with a lower concentration of apoptotic markers and externalized phosphatidylserine in MCUb-overexpressing clones. MCUb, if overexpressed, would seem to have an oncogenic connotation, increasing cell growth and invasiveness and protecting

cells from apoptotic death. To deepen clones' behavior concerning growth, we then focused on progression speed through the cell cycle. Through the use of a cytofluorimeter and the synthetic nucleoside analog of thymidine BrdU (that can be incorporated into the newly synthesized DNA, marking cells in S phase) we have noticed a higher rate of progression through the cell cycle by clones overexpressing MCUb, and a slower progress in shRNA-MCUb clones, compared to control cells.

Therefore MCUb, in addition to preventing the entry of Ca^{2+} in the mitochondrial matrix, favors cell growth in culture by increasing proliferation rate and protecting from ROS and apoptosis.

What remains to be clarified is why, under physiological conditions, the cell accumulates MCUb and prevents calcium entry into the mitochondria.

Spontaneous Ca^{2+} spikes have been observed in various stem cell lines; during cell cycle progression, cells exhibit Ca^{2+} transients during the G1 to S transition and mitosis, suggesting that these oscillations may play some role in cell cycle progression. We thought that increased MCUb concentration is useful to keep these transients with the correct amplitude and intensity in the cytosol rather than to only prevent calcium entering into the mitochondria. In fact, it was demonstrated that mitochondrial Ca^{2+} uptake contributes to buffering physiological Ca^{2+} loads. So, we decided to move our attention from the mitochondrial compartment to the cytosol. Control cells in M phase show many Ca^{2+} transients compared to cells in G1/S phase. Inversely, clones with a silenced expression of MCUb showed a smaller number of peaks, with significantly reduced size, width and frequency.

Taken together, all these evidences lead us to conclude that, under physiological conditions, the mitotic cell regulates mitochondria calcium uptake through a sustained expression of MCUb, the dominant negative subunit of the mitochondrial calcium uniporter. This event has the dual utility of protecting the cell from oxidative stress and apoptosis and preventing a mitochondrial buffering action. In this way, transient cytosolic calcium peaks in cytosol perform their function correctly, allowing the correct cell progression to the next phase of the cell cycle.

The blocking of mitochondrial buffering action, due to MCUb accumulation and to a uniporter composition stoichiometric change, could be a crucial event for many processes related to the mitotic $[Ca^{2+}]_c$ increase. In the future, it will be necessary to deepen the role of MCUb expression in mitotic processes where intracellular calcium is known to be involved, such as nuclear envelope breakdown, Ca^2 -CaM signaling pathway and cytokinesis.

Furthermore, this work proposes a new oncogenic role to this relatively new discovered component of the MCU complex. Supplementary and more detailed studies, both in vivo and in vitro, will serve in the future to clarify the possible role of this protein in a tumor context.

3.5 MATERIALS AND METHODS

Cell colture and transfection

T98G cells were maintained in a humidified 5% CO_2, 37°C incubator in Dulbecco's modified Eagle's medium (DMEM) supplemented with 10% fetal bovine serum (FBS; Life technologies, 10270) 100 U/ml penicillin (EuroClone, 3001D), 100 mg/ml streptomycin (EuroClone, 3000D). T98G cells were transfected with a standard calcium-phosphate procedure. For aequorin measurements, we used mtAEQ and cytAEQ. All measurements were performed 24 h after transfection.

Also mouse embryonic fibroblast (MEFs), Hela and MDCK cells were maintained in a humidified 5% CO2, 37°C incubator in Dulbecco's modified Eagle's medium (DMEM) supplemented with 10% fetal bovine serum (FBS; Life technologies, 10270) 100 U/ml penicillin (EuroClone, 3001D), 100 mg/ml streptomycin (EuroClone, 3000D).

T98G cells synchronization protocol

T98G cells were subjected to a synchronization protocol by the use of Serum Starvation (SS). Cells are seeded in wells and then subjected to SS, in particular with DMEM high glucose supplemented with only 0.1% FBS (the total absence of serum leads cells to autophagy) for 48-72 h. After this time cells was in G0 phase. Cells was then washed with PBS and subsequently additioned with complete medium with 10% FBS (Serum Readdition (SR)). After 4 h from SR cells are in G1 phase, after 12h in G1/S phase. S phase was reached after 24h from SR, G2 phase after 30h and mitosis after 36h.

Immunoblotting

For immunoblotting cells were scraped into ice-cold phosphate –buffered saline and lysed in a modified 10mM Tris buffer pH 7.4 containing 150mM NaCl, 1% Triton X-100, 10% glycerol, 10mM EDTA and protease inhibitor cocktail. After 30 minutes of incubation on ice, the lysates were cleared via centrifugation centrifuged at 12,000g at 4°C for 10 minutes. Protein concentration were determined by the Bio-Rad procedure. Protein extracts, 20 μg, were separated on 4-12% and 4-20% Bis-Tris acrylamide (Life technologies, NP0323 and EC6026) and electron- transferred to PVDF or Nitrocellulose membrane according to standard procedures. Unspecific binding sites were saturated by incubating membranes with TBS- Tween 20 (0.05%) supplemented with 5% non-fat powdered milk for 1h. Next, the membranes were incubated over-night with primary antibodies and the revelation was

assessed by the employment of appropriate HRP-labeled secondary antibodies [SantaCruz, sc-2004 (goat anti-rabbit) and sc-2005 (goat anti-mouse)] plus a chemiluminescent substrate (Thermo Scientific, 34080).

Cell cycle analysis

T98G cells were trypsinized and fixed in 70% ethanol overnight. Fixed cells were then treated with a mixture of Propidium Iodide, RNAseA and Triton-X-100 and analyzed for DNA content in different phases of the cell cycle in a TALI-Image based cytometer (Thermo Fisher).

mROS measurements

Total release of ROS from mitochondria was estimated fluorimetrically by oxidation of MitoSOX Red probe and Tali™ Image-Based Cytometer. Fluorescence was measured using 510 ± 10 nm excitation and 595 ± 35 nm emission wavelengths for MitoSOX and DHE while 513 ± 10 nm excitation and 530 ± 25 nm emission.

Cell proliferation and viability assay

Cells were seeded at 15,000 per well in a 6-well plate. Cells were seeded on 5 plates; one plate for each day. Every 24 hours after seeding, washed 1x with PBS and fixed in 4% paraformaldehyde in PBS for 15 min. Cells were stained with 0.1% crystal violet for 20 min. and then washed 3x with water. 1 ml 10% acetic acid to each well was added and incubate 20 min with shaking (extraction). Absorbance was measured at 590 nm.

Aequorin Measurements

Cells were grown on 13-mm-round glass coverslips at 50% confluence were transfected with the appropriate cytosolic (cyt), or mitochondrial (mt) targeted aequorin (Aeq). All aequorin measurements were performed in KRB. Agonist (Instamine 100 μM) was added to the medium as specified in the figure legends. The experiments were terminated by lysing the cells with 100 μM digitonin in a hypotonic Ca^{2+}-rich solution (10 mM $CaCl_2$ in H_2O), thus discharging the remaining aequorin pool. The light signal was collected and calibrated into $[Ca^{2+}]$ values.

The mitochondrial Ca^{2+} uptake rate was calculated as the first derivative by using OriginLab software. The higher value reached during Ca^{2+} addition represents the maximal Ca^{2+} uptake rate.

Fura-2 Measurements

The cytosolic Ca^{2+} response was evaluated using the fluorescent Ca^{2+} indicator Fura-2 AM (Life Technologies, Invitrogen). T98G cells were grown on 24-mm coverslips and incubated at 37 °C for 30 min in 1 mM Ca^{2+}/KRB supplemented with 2.5 mM Fura-2 AM, 0.02% Pluronic Acid F-68 (SigmaAldrich), and 0.1 mM sulfinpyrazone (Sigma-Aldrich). The cells were then washed and supplemented with 1 mM Ca^{2+}/KRB. To determine the cytosolic Ca^{2+} response, the cells were placed in an open Leyden chamber on a 37°C thermostat-controlled stage and exposed to 340 nm/380 nm wavelength light using the Olympus xcellence multiple-wavelength high-resolution fluorescence microscopy system equipped with an ORCA ER CCD camera (Hamamatsu Photonics) and an Uplan FLN 40× oil objective (Olympus). The fluorescence data collected are expressed as emission ratios.

Mitochondrial Ca^{2+} concentration measurements with 2mtGCaMP6m

T98G cells were grown on 24 mm coverslips and transfected with a standard calcium-phosphate procedure with 2mtGCaMP6m-encoding plasmids. After 24 or 48 hr, coverslips were placed in 1 ml of KRB and imaging was performed in an open Leyden chamber on a 37°C thermostat-controlled stage and exposed to 494 nm/406 nm wavelength light using the Olympus xcellence multiple-wavelength high-resolution fluorescence microscopy system equipped with an ORCA ER CCD camera (Hamamatsu Photonics) and an Uplan FLN 40× oil objective (Olympus). The fluorescence data collected are expressed as emission ratios.

Generation of Clones

For MCUb-overexpressing clones: T98G cells were transfected with a standard calcium-phosphate procedure with the cDNA for an empty vector epression (pcDNA3) and the MCUb cDNA. After 36h of expression complete medium including the selection antibiotic G418 (Geneticin, Gibco-BRL) at 800 ug/ml was added. After 16h the selection medium was changed with a 200 µg/ml G418 concentration. Selection medium was changed every 3 to 4 days for 3 to 4 weeks until large colonies of cells are clearly visible. Then, cells can be picked, expanded and assayed.

For MCUb shRNAs: Lentiviruses were produced by transfecting shRNA-targeting plasmids together with helper plasmids pCMV–VSVG and pCMV–dR8.74 into HEK293T cells. Cell supernatants were collected 24 and 48 h after transfection and were used to infect cells. To obtain stable cell lines, T98G cells were infected at middle/low confluence (35%) for 24 h with lentiviral supernatants diluted 1:1 with normal culture media in the presence of 5 ng

ml−1 of Polybrene (Sigma Aldrich). Cells were subjected to Puromycin selection 24 h after infection. After the selection, cells were expanded and assayed. Lentiviral ShRNAs were obtained from Sigma (MISSION ShRNA).
The resulting ShMCUb T98G cells were maintained in complete DMEM plus 2 μg/ml of Puromycin.

Wound healing assay

Clones were seeded in 6-well plates and grown to 90% confluence. The cell monolayer was wounded with a P200 pipette tip. Cells were monitored and captured after 24 and 48 hours of recovery by phase-contrast microscopy (a Leica phase-contrast microscope equipped with an ICC50 HD camera and a 4X objective). Then, the percentage of the open scratched area was measured using the Wound Healing Tool available in the software Fiji. Four replicates each of three independent experiments were performed.

Colony formation assay

Aliquots of T98G controls, MCUb-overexpressing and MCUb-silencing clone cells (1,000/well) were placed in 6-well plates 3 hours after 10 μM Etoposide pre-treatment and maintained in complete medium for 25 days. Colony formation was evaluated by staining the cells with 0.1% crystal violet. The rate of colony formation was calculated using the following equation: Colony formation rate = (number of colonies/number of seeded cells) × 100%. The experiments were performed in duplicate.

BrdU pulse and chase assay

T98G clones were cultured in 10 cm dishes to obtain a 85% confluency. BrdU was added to the cells for 30 minutes; cells were washed twice with PBS and incubated for 0-4-8 or 12 hours in fresh growth media. Labeled cells were collected by trypsinization, washed twice with PBS, and resuspended in 0.5 ml PBS. The cells were fixed overnight in 4 ml of 70% ethanol. The fixed cells were collected by centrifugation, and rehydrated in 5 ml PBS for 10 minutes. The cells were again collected by centrifugation and DNA was denatured for 30 minutes in 0.3 ml of a solution of 0.2 mg/ml pepsin in 2M hydrochloric acid. Following denaturation, the acid was neutralized with 1 ml of a solution of 3.8% sodium tetraborate (pH 8.5). The cells were then washed once with 1 ml of FACS buffer (2% BSA, 0.1% Triton-X 100, 0.1% sodium azide in PBS) and incubated with anti-BrdU antibody (diluted 1∶8 in FACS buffer) for 1 hour at room temperature. The cells were washed once with FACS buffer and resuspended in PI staining solution (0.1% Triton X 100, 0.1% RNAase cocktail

[Ambion], 0.02 mg/ml PI in PBS). The stained cells were analyzed by flow cytometry on a BD FACSCalibur Benchtop Analyzer. Scatter charts were analyzed with FlowJo v8.8.6.

Annexin V Binding Assay

To confirm the induction of apoptosis, the binding of Annexin V to externalized phosphatidylserine on the outer cellular surface, was assessed. Cells were washed twice in phosphate buffer saline (PBS). Subsequently, cells were resuspended and incubated in Annexin V binding buffer (10 mM HEPES, 10 mM NaOH, 140 mM NaCl, 1 mM CaCl2, pH 7.6) with Annexin V AlexaFluor-488 (1∶50) (Invitrogen, Canada, Cat No. A13201) for 15 minutes. In the final 10 minutes of incubation, 10 μM Hoechst and 1 mg/ml propidium iodide were added to the microcentrifuge tube and incubated for the final 10 minutes in the dark. The fluorescence was then evaluated through the use of the Tali Image-Based Cytometer.

4. BIBLIOGRAPHY

1. A. Rimessi, C. Giorgi, P. Pinton, R. Rizzuto, The versatility of mitochondrial calcium signals: from stimulation of cell metabolism to induction of cell death. *Biochim Biophys Acta* **1777**, 808-816 (2008).
2. G. A. Perkins, C. W. Renken, T. G. Frey, M. H. Ellisman, Membrane architecture of mitochondria in neurons of the central nervous system. *J Neurosci Res* **66**, 857-865 (2001).
3. M. E. Perotti, W. A. Anderson, H. Swift, Quantitative cytochemistry of the diaminobenzidine cytochrome oxidase reaction product in mitochondria of cardiac muscle and pancreas. *J Histochem Cytochem* **31**, 351-365 (1983).
4. L. Margulis, Symbiotic theory of the origin of eukaryotic organelles; criteria for proof. *Symp Soc Exp Biol*, 21-38 (1975).
5. C. N. Poston, S. C. Krishnan, C. R. Bazemore-Walker, In-depth proteomic analysis of mammalian mitochondria-associated membranes (MAM). *J Proteomics* **79**, 219-230 (2013).
6. J. M. Suski *et al.*, Isolation of plasma membrane-associated membranes from rat liver. *Nat Protoc* **9**, 312-322 (2014).
7. B. Kornmann, The molecular hug between the ER and the mitochondria. *Curr Opin Cell Biol* **25**, 443-448 (2013).
8. W. W. Franke, J. Kartenbeck, Outer mitochondrial membrane continuous with endoplasmic reticulum. *Protoplasma* **73**, 35-41 (1971).
9. D. J. Morre, W. D. Merritt, C. A. Lembi, Connections between mitochondria and endoplasmic reticulum in rat liver and onion stem. *Protoplasma* **73**, 43-49 (1971).
10. D. E. Copeland, A. J. Dalton, An association between mitochondria and the endoplasmic reticulum in cells of the pseudobranch gland of a teleost. *J Biophys Biochem Cytol* **5**, 393-396 (1959).
11. J. A. Lewis, J. R. Tata, A rapidly sedimenting fraction of rat liver endoplasmic reticulum. *J Cell Sci* **13**, 447-459 (1973).
12. A. E. Rusinol, Z. Cui, M. H. Chen, J. E. Vance, A unique mitochondria-associated membrane fraction from rat liver has a high capacity for lipid synthesis and contains pre-Golgi secretory proteins including nascent lipoproteins. *J Biol Chem* **269**, 27494-27502 (1994).
13. P. J. Meier, M. A. Spycher, U. A. Meyer, Isolation and characterization of rough endoplasmic reticulum associated with mitochondria from normal rat liver. *Biochim Biophys Acta* **646**, 283-297 (1981).
14. M. R. Wieckowski, C. Giorgi, M. Lebiedzinska, J. Duszynski, P. Pinton, Isolation of mitochondria-associated membranes and mitochondria from animal tissues and cells. *Nat Protoc* **4**, 1582-1590 (2009).
15. E. A. Schon, E. Area-Gomez, Mitochondria-associated ER membranes in Alzheimer disease. *Mol Cell Neurosci* **55**, 26-36 (2013).
16. A. Raturi, T. Simmen, Where the endoplasmic reticulum and the mitochondrion tie the knot: the mitochondria-associated membrane (MAM). *Biochim Biophys Acta* **1833**, 213-224 (2013).
17. H. A. Krebs, L. V. Eggleston, The oxidation of pyruvate in pigeon breast muscle. *Biochem J* **34**, 442-459 (1940).
18. D. O. Lambeth, K. N. Tews, S. Adkins, D. Frohlich, B. I. Milavetz, Expression of two succinyl-CoA synthetases with different nucleotide specificities in mammalian tissues. *J Biol Chem* **279**, 36621-36624 (2004).
19. S. Amemori *et al.*, Oral dimethyl sulfoxide for systemic amyloid A amyloidosis complication in chronic inflammatory disease: a retrospective patient chart review. *J Gastroenterol* **41**, 444-449 (2006).
20. M. J. Berridge, P. Lipp, M. D. Bootman, The versatility and universality of calcium signalling. *Nat Rev Mol Cell Biol* **1**, 11-21 (2000).

21. E. Chevet, P. H. Cameron, M. F. Pelletier, D. Y. Thomas, J. J. Bergeron, The endoplasmic reticulum: integration of protein folding, quality control, signaling and degradation. *Curr Opin Struct Biol* **11**, 120-124 (2001).
22. M. D. Bootman, O. H. Petersen, A. Verkhratsky, The endoplasmic reticulum is a focal point for co-ordination of cellular activity. *Cell Calcium* **32**, 231-234 (2002).
23. J. J. MacKrill, Protein-protein interactions in intracellular Ca2+-release channel function. *Biochem J* **337 (Pt 3)**, 345-361 (1999).
24. T. Litjens *et al.*, Phospholipase C-gamma1 is required for the activation of store-operated Ca2+ channels in liver cells. *Biochem J* **405**, 269-276 (2007).
25. M. Iwai *et al.*, Molecular cloning of mouse type 2 and type 3 inositol 1,4,5-trisphosphate receptors and identification of a novel type 2 receptor splice variant. *J Biol Chem* **280**, 10305-10317 (2005).
26. K. Mikoshiba, IP3 receptor/Ca2+ channel: from discovery to new signaling concepts. *J Neurochem* **102**, 1426-1446 (2007).
27. M. Hirata, E. Suematsu, T. Hashimoto, T. Hamachi, T. Koga, Release of Ca2+ from a non-mitochondrial store site in peritoneal macrophages treated with saponin by inositol 1,4,5-trisphosphate. *Biochem J* **223**, 229-236 (1984).
28. L. Missiaen, C. W. Taylor, M. J. Berridge, Luminal Ca2+ promoting spontaneous Ca2+ release from inositol trisphosphate-sensitive stores in rat hepatocytes. *J Physiol* **455**, 623-640 (1992).
29. J. B. Smith, L. Smith, B. L. Higgins, Temperature and nucleotide dependence of calcium release by myo-inositol 1,4,5-trisphosphate in cultured vascular smooth muscle cells. *J Biol Chem* **260**, 14413-14416 (1985).
30. I. Bezprozvanny, B. E. Ehrlich, ATP modulates the function of inositol 1,4,5-trisphosphate-gated channels at two sites. *Neuron* **10**, 1175-1184 (1993).
31. S. Marchi, P. Pinton, Alterations of calcium homeostasis in cancer cells. *Curr Opin Pharmacol* **29**, 1-6 (2016).
32. S. Marchi, P. Pinton, The mitochondrial calcium uniporter complex: molecular components, structure and physiopathological implications. *J Physiol* **592**, 829-839 (2014).
33. J. M. Baughman *et al.*, Integrative genomics identifies MCU as an essential component of the mitochondrial calcium uniporter. *Nature* **476**, 341-345 (2011).
34. F. Perocchi *et al.*, MICU1 encodes a mitochondrial EF hand protein required for Ca(2+) uptake. *Nature* **467**, 291-296 (2010).
35. Y. Sancak *et al.*, EMRE is an essential component of the mitochondrial calcium uniporter complex. *Science* **342**, 1379-1382 (2013).
36. A. Raffaello *et al.*, The mitochondrial calcium uniporter is a multimer that can include a dominant-negative pore-forming subunit. *EMBO J* **32**, 2362-2376 (2013).
37. B. S. Jhun *et al.*, The mitochondrial Ca2+ uniporter: regulation by auxiliary subunits and signal transduction pathways. *Am J Physiol Cell Physiol* **311**, C67-80 (2016).
38. K. Mallilankaraman *et al.*, MCUR1 is an essential component of mitochondrial Ca2+ uptake that regulates cellular metabolism. *Nat Cell Biol* **14**, 1336-1343 (2012).
39. M. Patron *et al.*, MICU1 and MICU2 finely tune the mitochondrial Ca2+ uniporter by exerting opposite effects on MCU activity. *Mol Cell* **53**, 726-737 (2014).
40. L. Galluzzi *et al.*, Essential versus accessory aspects of cell death: recommendations of the NCCD 2015. *Cell Death Differ* **22**, 58-73 (2015).
41. G. Kroemer *et al.*, Classification of cell death: recommendations of the Nomenclature Committee on Cell Death. *Cell Death Differ* **12 Suppl 2**, 1463-1467 (2005).
42. J. F. Curtin, T. G. Cotter, Apoptosis: Historical perspectives. *Essays Biochem* **39**, 1-10 (2003).
43. G. Kroemer, L. Galluzzi, C. Brenner, Mitochondrial membrane permeabilization in cell death. *Physiol Rev* **87**, 99-163 (2007).

44. C. Garrido *et al.*, Mechanisms of cytochrome c release from mitochondria. *Cell Death Differ* **13**, 1423-1433 (2006).
45. M. M. Hill, C. Adrain, S. J. Martin, Portrait of a killer: the mitochondrial apoptosome emerges from the shadows. *Mol Interv* **3**, 19-26 (2003).
46. L. Ravagnan, T. Roumier, G. Kroemer, Mitochondria, the killer organelles and their weapons. *J Cell Physiol* **192**, 131-137 (2002).
47. P. Pinton *et al.*, The Ca2+ concentration of the endoplasmic reticulum is a key determinant of ceramide-induced apoptosis: significance for the molecular mechanism of Bcl-2 action. *EMBO J* **20**, 2690-2701 (2001).
48. N. N. Danial, S. J. Korsmeyer, Cell death: critical control points. *Cell* **116**, 205-219 (2004).
49. R. J. Youle, M. Karbowski, Mitochondrial fission in apoptosis. *Nat Rev Mol Cell Biol* **6**, 657-663 (2005).
50. M. Bonora *et al.*, Molecular mechanisms of cell death: central implication of ATP synthase in mitochondrial permeability transition. *Oncogene* **34**, 1475-1486 (2015).
51. P. O. Seglen, P. Bohley, Autophagy and other vacuolar protein degradation mechanisms. *Experientia* **48**, 158-172 (1992).
52. M. Tsukada, Y. Ohsumi, Isolation and characterization of autophagy-defective mutants of Saccharomyces cerevisiae. *FEBS Lett* **333**, 169-174 (1993).
53. R. Kang, H. J. Zeh, M. T. Lotze, D. Tang, The Beclin 1 network regulates autophagy and apoptosis. *Cell Death Differ* **18**, 571-580 (2011).
54. B. Ravikumar *et al.*, Regulation of mammalian autophagy in physiology and pathophysiology. *Physiol Rev* **90**, 1383-1435 (2010).
55. R. A. Gottlieb, R. S. Carreira, Autophagy in health and disease. 5. Mitophagy as a way of life. *Am J Physiol Cell Physiol* **299**, C203-210 (2010).
56. H. Koh, J. Chung, PINK1 as a molecular checkpoint in the maintenance of mitochondrial function and integrity. *Mol Cells* **34**, 7-13 (2012).
57. D. Narendra, L. A. Kane, D. N. Hauser, I. M. Fearnley, R. J. Youle, p62/SQSTM1 is required for Parkin-induced mitochondrial clustering but not mitophagy; VDAC1 is dispensable for both. *Autophagy* **6**, 1090-1106 (2010).
58. G. Ashrafi, T. L. Schwarz, The pathways of mitophagy for quality control and clearance of mitochondria. *Cell Death Differ* **20**, 31-42 (2013).
59. J. Zhang *et al.*, Mitochondrial clearance is regulated by Atg7-dependent and -independent mechanisms during reticulocyte maturation. *Blood* **114**, 157-164 (2009).
60. M. Giacomello, I. Drago, P. Pizzo, T. Pozzan, Mitochondrial Ca2+ as a key regulator of cell life and death. *Cell Death Differ* **14**, 1267-1274 (2007).
61. S. Marchi *et al.*, Downregulation of the mitochondrial calcium uniporter by cancer-related miR-25. *Curr Biol* **23**, 58-63 (2013).
62. Y. Liao *et al.*, Mitochondrial calcium uniporter protein MCU is involved in oxidative stress-induced cell death. *Protein Cell* **6**, 434-442 (2015).
63. A. N. Antony *et al.*, MICU1 regulation of mitochondrial Ca(2+) uptake dictates survival and tissue regeneration. *Nat Commun* **7**, 10955 (2016).
64. A. Tosatto *et al.*, The mitochondrial calcium uniporter regulates breast cancer progression via HIF-1alpha. *EMBO Mol Med* **8**, 569-585 (2016).
65. P. Yu-Wai-Man, P. G. Griffiths, N. Howell, D. M. Turnbull, P. F. Chinnery, The Epidemiology of Leber Hereditary Optic Neuropathy in the North East of England. *Am J Hum Genet* **98**, 1271 (2016).
66. D. Bargiela, P. Yu-Wai-Man, M. Keogh, R. Horvath, P. F. Chinnery, Prevalence of neurogenetic disorders in the North of England. *Neurology* **85**, 1195-1201 (2015).
67. D. C. Wallace *et al.*, Mitochondrial DNA mutation associated with Leber's hereditary optic neuropathy. *Science* **242**, 1427-1430 (1988).

68. V. Carelli, F. N. Ross-Cisneros, A. A. Sadun, Mitochondrial dysfunction as a cause of optic neuropathies. *Prog Retin Eye Res* **23**, 53-89 (2004).
69. P. Yu-Wai-Man, P. G. Griffiths, P. F. Chinnery, Mitochondrial optic neuropathies - disease mechanisms and therapeutic strategies. *Prog Retin Eye Res* **30**, 81-114 (2011).
70. A. Baracca *et al.*, Severe impairment of complex I-driven adenosine triphosphate synthesis in leber hereditary optic neuropathy cybrids. *Arch Neurol* **62**, 730-736 (2005).
71. A. Korsten *et al.*, Patients with Leber hereditary optic neuropathy fail to compensate impaired oxidative phosphorylation. *Biochimica et biophysica acta* **1797**, 197-203 (2010).
72. S. Beretta *et al.*, Leber hereditary optic neuropathy mtDNA mutations disrupt glutamate transport in cybrid cell lines. *Brain* **127**, 2183-2192 (2004).
73. M. Floreani *et al.*, Antioxidant defences in cybrids harboring mtDNA mutations associated with Leber's hereditary optic neuropathy. *FEBS J* **272**, 1124-1135 (2005).
74. C. S. Lin *et al.*, Mouse mtDNA mutant model of Leber hereditary optic neuropathy. *Proceedings of the National Academy of Sciences of the United States of America* **109**, 20065-20070 (2012).
75. A. Ghelli *et al.*, Leber's hereditary optic neuropathy (LHON) pathogenic mutations induce mitochondrial-dependent apoptotic death in transmitochondrial cells incubated with galactose medium. *The Journal of biological chemistry* **278**, 4145-4150 (2003).
76. C. Zanna *et al.*, Caspase-independent death of Leber's hereditary optic neuropathy cybrids is driven by energetic failure and mediated by AIF and Endonuclease G. *Apoptosis : an international journal on programmed cell death* **10**, 997-1007 (2005).
77. C. Giordano *et al.*, Efficient mitochondrial biogenesis drives incomplete penetrance in Leber's hereditary optic neuropathy. *Brain* **137**, 335-353 (2014).
78. A. A. Sadun, P. H. Win, F. N. Ross-Cisneros, S. O. Walker, V. Carelli, Leber's hereditary optic neuropathy differentially affects smaller axons in the optic nerve. *Trans Am Ophthalmol Soc* **98**, 223-232; discussion 232-225 (2000).
79. B. X. Pan *et al.*, Mathematically modeling the involvement of axons in Leber's hereditary optic neuropathy. *Invest Ophthalmol Vis Sci* **53**, 7608-7617 (2012).
80. V. Ramos Cdo *et al.*, Association of optic disc size with development and prognosis of Leber's hereditary optic neuropathy. *Invest Ophthalmol Vis Sci* **50**, 1666-1674 (2009).
81. C. Giordano *et al.*, Oestrogens ameliorate mitochondrial dysfunction in Leber's hereditary optic neuropathy. *Brain* **134**, 220-234 (2011).
82. V. Carelli, C. Giordano, G. d'Amati, Pathogenic expression of homoplasmic mtDNA mutations needs a complex nuclear-mitochondrial interaction. *Trends Genet* **19**, 257-262 (2003).
83. V. Carelli *et al.*, Parsing the differences in affected with LHON: genetic versus environmental triggers of disease conversion. *Brain* **139**, e17 (2016).
84. L. Giordano *et al.*, Cigarette toxicity triggers Leber's hereditary optic neuropathy by affecting mtDNA copy number, oxidative phosphorylation and ROS detoxification pathways. *Cell death & disease* **6**, e2021 (2015).
85. G. Twig, O. S. Shirihai, The interplay between mitochondrial dynamics and mitophagy. *Antioxidants & redox signaling* **14**, 1939-1951 (2011).
86. S. Patergnani, P. Pinton, Mitophagy and mitochondrial balance. *Methods Mol Biol* **1241**, 181-194 (2015).
87. L. Thukral *et al.*, The Molecular Mechanism Underlying Recruitment and Insertion of Lipid-Anchored LC3 Protein into Membranes. *Biophys J* **109**, 2067-2078 (2015).
88. N. J. Dolman, K. M. Chambers, B. Mandavilli, R. H. Batchelor, M. S. Janes, Tools and techniques to measure mitophagy using fluorescence microscopy. *Autophagy* **9**, 1653-1662 (2013).
89. Y. Katsuragi, Y. Ichimura, M. Komatsu, p62/SQSTM1 functions as a signaling hub and an autophagy adaptor. *FEBS J* **282**, 4672-4678 (2015).

90. R. Chen *et al.*, The general amino acid control pathway regulates mTOR and autophagy during serum/glutamine starvation. *The Journal of cell biology* **206**, 173-182 (2014).
91. T. Kanki, K. Okamoto, Assays for autophagy II: Mitochondrial autophagy. *Methods Mol Biol* **1163**, 165-173 (2014).
92. M. L. Genova, G. Lenaz, Functional role of mitochondrial respiratory supercomplexes. *Biochimica et biophysica acta* **1837**, 427-443 (2014).
93. C. Li *et al.*, Impact of autophagy inhibition at different stages on cytotoxic effect of autophagy inducer in glioblastoma cells. *Cell Physiol Biochem* **35**, 1303-1316 (2015).
94. J. Park *et al.*, Haloperidol and clozapine block formation of autophagolysosomes in rat primary neurons. *Neuroscience* **209**, 64-73 (2012).
95. V. Carelli *et al.*, Idebenone treatment in Leber's hereditary optic neuropathy. *Brain* **134**, e188 (2011).
96. A. Dabrowska *et al.*, PGC-1alpha controls mitochondrial biogenesis and dynamics in lead-induced neurotoxicity. *Aging (Albany NY)* **7**, 629-647 (2015).
97. H. A. Tuppen, E. L. Blakely, D. M. Turnbull, R. W. Taylor, Mitochondrial DNA mutations and human disease. *Biochimica et biophysica acta* **1797**, 113-128 (2010).
98. V. Carelli, Keeping in shape the dogma of mitochondrial DNA maternal inheritance. *PLoS Genet* **11**, e1005179 (2015).
99. Z. Xie, D. J. Klionsky, Autophagosome formation: core machinery and adaptations. *Nature cell biology* **9**, 1102-1109 (2007).
100. Y. Feng, D. He, Z. Yao, D. J. Klionsky, The machinery of macroautophagy. *Cell research* **24**, 24-41 (2014).
101. N. Mizushima, M. Komatsu, Autophagy: renovation of cells and tissues. *Cell* **147**, 728-741 (2011).
102. B. Levine, G. Kroemer, Autophagy in the pathogenesis of disease. *Cell* **132**, 27-42 (2008).
103. Y. Tsujimoto, S. Shimizu, Another way to die: autophagic programmed cell death. *Cell death and differentiation* **12 Suppl 2**, 1528-1534 (2005).
104. P. Jiang, N. Mizushima, Autophagy and human diseases. *Cell research* **24**, 69-79 (2014).
105. M. Komatsu *et al.*, Homeostatic levels of p62 control cytoplasmic inclusion body formation in autophagy-deficient mice. *Cell* **131**, 1149-1163 (2007).
106. N. Mizushima, T. Yoshimori, B. Levine, Methods in mammalian autophagy research. *Cell* **140**, 313-326 (2010).
107. K. Fujisawa *et al.*, TZDs reduce mitochondrial ROS production and enhance mitochondrial biogenesis. *Biochem Biophys Res Commun* **379**, 43-48 (2009).
108. D. I. Orellana *et al.*, Coenzyme A corrects pathological defects in human neurons of PANK2-associated neurodegeneration. *EMBO Mol Med* **8**, 1197-1211 (2016).
109. N. Moya, J. Cutts, T. Gaasterland, K. Willert, D. A. Brafman, Endogenous WNT signaling regulates hPSC-derived neural progenitor cell heterogeneity and specifies their regional identity. *Stem Cell Reports* **3**, 1015-1028 (2014).
110. A. W. Murray, Recycling the cell cycle: cyclins revisited. *Cell* **116**, 221-234 (2004).
111. M. Malumbres, Cyclin-dependent kinases. *Genome Biol* **15**, 122 (2014).
112. J. V. Harper, G. Brooks, The mammalian cell cycle: an overview. *Methods Mol Biol* **296**, 113-153 (2005).
113. K. Vermeulen, D. R. Van Bockstaele, Z. N. Berneman, The cell cycle: a review of regulation, deregulation and therapeutic targets in cancer. *Cell Prolif* **36**, 131-149 (2003).
114. A. D. Russa, C. Maesawa, Y. Satoh, Spontaneous [Ca2+]i oscillations in G1/S phase-synchronized cells. *J Electron Microsc (Tokyo)* **58**, 321-329 (2009).
115. M. Murgia, C. Giorgi, P. Pinton, R. Rizzuto, Controlling metabolism and cell death: at the heart of mitochondrial calcium signalling. *J Mol Cell Cardiol* **46**, 781-788 (2009).

116. L. Santella, E. Ercolano, G. A. Nusco, The cell cycle: a new entry in the field of Ca2+ signaling. *Cell Mol Life Sci* **62**, 2405-2413 (2005).
117. J. Humeau *et al.*, Calcium signaling and cell cycle: Progression or death. *Cell Calcium*, (2017).
118. E. H. Verbon, J. A. Post, J. Boonstra, The influence of reactive oxygen species on cell cycle progression in mammalian cells. *Gene* **511**, 1-6 (2012).
119. M. Tiwari, S. Prasad, T. G. Shrivastav, S. K. Chaube, Calcium Signaling During Meiotic Cell Cycle Regulation and Apoptosis in Mammalian Oocytes. *J Cell Physiol* **232**, 976-981 (2017).
120. D. Skrajnowska, B. Bobrowska-Korczak, A. Tokarz, Disorders of mechanisms of calcium metabolism control as potential risk factors of prostate cancer. *Curr Med Chem*, (2017).
121. C. Cardenas *et al.*, Selective Vulnerability of Cancer Cells by Inhibition of Ca(2+) Transfer from Endoplasmic Reticulum to Mitochondria. *Cell Rep* **14**, 2313-2324 (2016).
122. R. E. Shackelford, W. K. Kaufmann, R. S. Paules, Cell cycle control, checkpoint mechanisms, and genotoxic stress. *Environ Health Perspect* **107 Suppl 1**, 5-24 (1999).
123. C. R. Kahl, A. R. Means, Regulation of cell cycle progression by calcium/calmodulin-dependent pathways. *Endocr Rev* **24**, 719-736 (2003).
124. A. Danese *et al.*, Calcium regulates cell death in cancer: Roles of the mitochondria and mitochondria-associated membranes (MAMs). *Biochim Biophys Acta* **1858**, 615-627 (2017).
125. S. Missiroli *et al.*, Endoplasmic reticulum-mitochondria Ca(2+) crosstalk in the control of the tumor cell fate. *Biochim Biophys Acta* **1864**, 858-864 (2017).
126. B. Ciapa, D. Pesando, M. Wilding, M. Whitaker, Cell-cycle calcium transients driven by cyclic changes in inositol trisphosphate levels. *Nature* **368**, 875-878 (1994).
127. K. A. Skelding, J. A. Rostas, N. M. Verrills, Controlling the cell cycle: the role of calcium/calmodulin-stimulated protein kinases I and II. *Cell Cycle* **10**, 631-639 (2011).
128. M. Levasseur, A. McDougall, Sperm-induced calcium oscillations at fertilisation in ascidians are controlled by cyclin B1-dependent kinase activity. *Development* **127**, 631-641 (2000).
129. C. R. Kahl, A. R. Means, Regulation of cyclin D1/Cdk4 complexes by calcium/calmodulin-dependent protein kinase I. *J Biol Chem* **279**, 15411-15419 (2004).
130. J. W. Harbour, R. X. Luo, A. Dei Santi, A. A. Postigo, D. C. Dean, Cdk phosphorylation triggers sequential intramolecular interactions that progressively block Rb functions as cells move through G1. *Cell* **98**, 859-869 (1999).
131. K. P. Lu, A. R. Means, Regulation of the cell cycle by calcium and calmodulin. *Endocr Rev* **14**, 40-58 (1993).
132. Y. Sasaki, H. Hidaka, Calmodulin and cell proliferation. *Biochem Biophys Res Commun* **104**, 451-456 (1982).
133. A. Margalit, S. Vlcek, Y. Gruenbaum, R. Foisner, Breaking and making of the nuclear envelope. *J Cell Biochem* **95**, 454-465 (2005).
134. R. Rizzuto, M. Brini, M. Murgia, T. Pozzan, Microdomains with high Ca2+ close to IP3-sensitive channels that are sensed by neighboring mitochondria. *Science* **262**, 744-747 (1993).